Doctoral Thesis

Development of fluorescent molecules and nanobioconjugates for cell imaging and singlet oxygen sensing

(細胞イメージングと一重項酸素センシングに向けた蛍光分子とナノバイオコンジュゲートの開発)

Division of Environmental Materials Science

Graduate School of Environmental Science

Hokkaido University

Sobhanan Jeladhara

September 2022

Acknowledgment

I owe my deepest gratitude to my supervisor Prof. Vasudevan Pillai Biju, without whose support, enthusiasm, and encouragement this thesis would have remained a dream. His knowledge and valuable guidance helped me throughout my doctoral research. I would like to thank Associate Professor Yuta Takano and Assistant Professor Palyam Subramanyam for their insightful discussions and comments. I kindly appreciate Mrs. Atsuko Fujii for helping me with the administrative tasks.

I extend my sincere thanks to the thesis committee members: Prof. Shin-ichiro Noro and Prof. Katsuaki Konishi for their valuable suggestions and comments. I am grateful to the Special Grant Program of the Graduate School of Environmental Science and Hokkaido University DX Doctoral Fellowship. I also thank Hokkaido University Nikon Imaging Centre and Nanotechnology PLATFORM for the facilities in my research.

I thank the former and current members of the Laboratory of Molecular Photonics, including Dr. Md. Shahjahan, Dr. Lata Chouhan, Dr. Devika Sasikumar, Dr. Sushant Ghimire, Dr. Bhagya Lakshmi, Dr. Takuya Okamoto, B. M. Sachith, Hanjun Zhao, Dong Zhang, Kazuya Yoshida, Rumana Akter, Farida Khatun, Danyang Chen, Zhijing Zhang, and Feijun Xu for their kind co-operation and friendship. I also acknowledge with gratitude the motivation and love of my family members and friends, especially, Archana and Ishfaq. Ultimately, I am indebted to my parents Sobhanan and Beena, and my brother Mohit for their understanding and trust while pursuing my research, whose prayers made me sustain this far.

Above all, my sincere gratitude to the Great Almighty, the author of knowledge and wisdom. His countless love and strength let me through all the pains and difficulties to achieve my degree.

Abstract

Recently, theranostics, a combination of diagnosis and therapy, has become a key modality in cancer management. Certain intrinsic limitations in conventional cancer diagnosis/therapy strategies lead to the development of nanomaterial-based therapeutics. Different nanoparticles have been developed into theranostics by combining multimodal contrast/imaging agents, drugs, and targeting moieties for cancer diagnosis, monitoring, therapy, and treatment follow-up. Theranostics for fluorescence imaging or fluorescence molecular tomography (FMT) using organic dyes and semiconductor nanocrystals with ligands/antibodies against cancer markers receive much attention in basic research and clinical applications. Also, nanomaterials combining FMT with chemotherapy, hyperthermia, or phototherapy enter the clinical stage. This thesis focuses on nanobioconjugates combining fluorescence probes, photosensitizers, fluorogenic sensors, and cancer-targeting biomolecules.

I use fluorescence probes such as semiconductor quantum dots (QDs) and nucleus staining Syto dyes to detect or image cancer cells. Also, QDs and porphyrins generate singlet oxygen ($^1O_2$), an essential reactive oxygen species (ROS) in photodynamic therapy (PDT), which is detected using a high sensitivity electron donor-acceptor (D-A) fluorogenic molecule. The cancer-targeting biomolecules include anticancer antibodies and a peptide. Rationally designed nanobioconjugates using the above components help me enrich and efficiently detect cancer cells in blood samples, and produce, detect, store and release $^1O_2$ in a solution or cells.

This thesis has five chapters, including general conclusions and perspectives. Chapter 1 of the thesis provides a general introduction to fundamental aspects of cancer management. Next, I discuss the significance of circulating tumor cells (CTCs)-based liquid biopsy and the current detection technologies for CTC isolation and enrichment. The importance of nanomaterials-based immunocapturing and optical detection based on the fundamental properties of nanomaterials are also discussed. Next, I discuss the role of $^1O_2$ in cancer therapeutics due to its cytotoxic effect on various biological substrates. I also discuss a few biological and chemical processes involved in the generation of $^1O_2$ followed by its detection using fluorescent molecular probes.

Chapter 2 provides the experimental procedures and techniques in this study. I discuss the procedure for the functionalization of silica, attachment of antibodies on functionalized silica microparticles, QD labeling with cancer-specific antibodies, and the attachment of QD-

antibody conjugates on the functionalized silica particles. I also discuss the synthesis of a $^1O_2$ sensor molecule, preparation of silica-$^1O_2$ sensor nanoassemblies, and the conjugation of cell-penetrating peptides on the nanoassembly. Next, I discuss the procedure for cell culture and cell labeling. I also discuss time-resolved fluorescence spectroscopy used in the characterization of CTCs. Finally, I discuss UV-vis absorption spectroscopy, steady-state and time-resolved fluorescence spectroscopy, single-particle microspectroscopy, laser scanning confocal microscopy, nuclear magnetic resonance spectroscopy, and scanning electron microscopy used in this thesis.

In chapter 3, I discuss a multimodal fluorescence microspectroscopic and mesenchymal-antigen specific detection, collection, and characterization of cancer cells. I use self-segregating immunosilica microparticles to capture the pre-labeled cells and the cells are identified from modalities such as multicolor images, multimodal fluorescence spectra, and fluorescence decay profile of nucleus staining dyes or QDs. The large size of silica microparticles prevents their endocytosis and help avoid an external force for cell separation, and the CD44 antigen-selective cell capturing help in an error-free cancer cell detection. The CD44-targeted cell collection combined with the above modalities shows a 9-fold detection accuracy for CTCs among blood cells.

In chapter 4, I synthesize a $^1O_2$ sensor composed of an aminomethyl anthracene and a coumarin moieties to increase the efficiency of intracellular $^1O_2$ generation, detection, and release. I construct a nanoassembly of a sensitizer and the sensor and investigate the ability of the assembly to generate, store, sense, and release $^1O_2$ at the ensemble, single-particle, and cell levels. In all cases, the sensor shows an enormous fluorescence enhancement due to the reaction of $^1O_2$ generated by the photosensitizer. The mechanisms behind $^1O_2$ sensing and releasing are explained in detail in this chapter. The intracellular uptake ability of the nanoassembly and $^1O_2$ generation are studied after conjugating an RGD peptide to the assembly. The single-particle and cell imaging reveal continuous $^1O_2$ release and efficient cell death. In addition, the fluorescence from the photosensitizer and the sensor help colocalized cell imaging. Thus, this work highlights the utilization of programed nanocarriers for multimodal cancer therapeutic strategies.

Chapter 5 is the general summary of the thesis and future prospects of nanobioconjugates and $^1O_2$ sensing-releasing probes for cancer therapy. Also, I explain the toxicity aspects and the significance to analyze the pharmacokinetics of nanobioconjugates.

Abbreviations and symbols

APTES	(3-aminopropyl)triethoxysilane
ab	Antibody
RGD	Arginine-Glycine-Aspartic
E_g	Bandgap energy
BP	Band-pass
CSC	Cancer stem cell
ca	Centered around
cm	Centimeter
CCD	Charge coupled device
δ	Chemical shift
CTC	Circulating tumor cell
CD44	Cluster of Differentiation 44
CB	Conduction band
CLSM	Confocal laser scanning microscopy
cw	Continuous wave
CK	Cytokeratin
°C	Degree Celsius
DNA	Deoxyribonucleic acid
DMT-MM	4-(4,6-Dimethoxy-1,3,5-triazin-2-yl)-4-methylmorpholinium chloride
DMSO	Dimethyl sulfoxide
d	Doublet
ET	Electron transfer
EMCCD	Electron multiplying charge-coupled device

EPO	Endoperoxide
EGFR	Epidermal growth factor receptor
EpCAM	Epithelial adhesion molecule
EMT	Epithelial-to-mesenchymal transition
eq.	Equivalent
fs	Femtosecond
ϕ_F	Fluorescence quantum efficiency/yield
FDA	Food and drug administration
g	Gram
HOMO	Highest occupied molecular orbital
h	Hour
HER2	Human epidermal growth factor receptor 2
ISC	Intersystem crossing
kHz	Kilohertz
kV	Kilovolt
L	Litre
LP	Long pass
LUMO	Lowest unoccupied molecular orbital
MHz	Megahertz
MSNP	Mesoporous silica nanoparticle
µg	Microgram
µL	Microlitre
µm	Micrometer
µM	Micromolar

µmol	Micromole
mg	Milligram
mL	Milliliter
mm	Millimeter
mmol	Millimole
mM	Millimolar
ms	Millisecond
mW	Milliwatt
min	Minute
mol	Mole
m	Multiplet
nm	Nanometer
nM	Nanomolar
NP	Nanoparticle
ns	Nanosecond
NIR	Near infrared
NMR	Nuclear magnetic resonance
NA	Numerical aperture
PBMC	Peripheral blood mononuclear cell
PBS	Phosphate buffered saline
PET	Photoinduced electron transfer
PMT	Photomultiplier tube
PDT	Photodynamic therapy
PS	Photosensitizer

PTT	Photothermal therapy
QD	Quantum dot
q	Quartet
ROS	Reactive oxygen species
RNA	Ribonucleic acid
RT	Room temperature
s	Second, Singlet
SEM	Scanning electron microscope
$^1O_2$	Singlet oxygen
NaN_3	Sodium azide
TCPP	Tetrakis(4-carboxyphenyl)porphyrin
t	Triplet
UV	Ultraviolet
VB	Valence band
Vis	Visible
λ	Wavelength
wt%	Weight percent

Table of contents

Chapter 1

Introduction

Abstract

The GLOBOCAN 2020 estimates by the International Agency for Research on Cancer report 10 million cancer deaths and 19.3 million new cancer cases. Cancer remains a threat to human survival as the second leading cause of death in developing countries. Thus, improved diagnostic and targeted therapies are crucial for successful treatment and increased survival rates. This chapter outlines the causes and genetic alterations contributing to cancer, followed by different diagnostic and treatment modalities, including laboratory tests, tumor markers, biopsy, and imaging techniques used by clinicians. Next, I introduced liquid biopsy as an innovative tool for the early detection of cancer, where I explained the pros and cons between liquid biopsy and conventional tissue biopsy, among which circulating tumor cells (CTCs) serve as an excellent diagnostic and prognostic marker to enhance the treatment efficacy. Later, I discuss the current detection technologies for CTCs isolation based on their characteristic physical or biological properties different from hematologic cells. The immunoaffinity-based technique increases the sensitivity and reliability of CTC capture. Further, I discuss the advantages of nanomaterials for CTC enrichment, particularly silica- and quantum dots-based immunocapture and fluorescence detection of the CTCs. The next section explains the cytotoxic effects of singlet oxygen (1O2) on the oxidation of cellular macromolecules, cell signaling, and cell ablation by emphasizing its key role in cancer therapeutic application. Various methods for the endogenous and chemical generation of $^1O_2$ are explained, followed by luminescent molecular probes for its detection. The merit of anthracene-based chemical tools for $^1O_2$ detection is highlighted, and the photophysical factors that govern the $^1O_2$ quantum yield are also discussed. I finally conclude the chapter with the motivation to conduct my research.

1.1 Cancer diagnosis

Cancer is a major public health concern and the leading cause of mortality worldwide. The GLOBOCAN estimates produced by the International Agency for Research across 185 countries on cancer incidence and mortality indicated 19.3 million new cases and 10 million cancer deaths in 2020.[1] Cancer cells differ from the normal cells in various ways. It is a genetic disease that results in the abnormal growth of cells. The uncontrolled cell division forms lumps of tissue or clusters of cells called tumors that can be benign (noncancerous) or malignant (cancerous).[2] Genetic changes in cells can happen by inheritance due to the changes in germ cells (eggs and sperms) known as germline changes found in the offspring. It is also caused due to the errors that happen during the cell division or DNA damages induced by carcinogenic substances such as UV rays or chemicals in tobacco smoke that affect either one unit (nucleotide) or long stretches of DNA, causing rearrangements, deletions, or DNA duplications.[3] Mutations in three types of genes mainly contribute to cancer – proto-oncogenes, tumor suppressor genes, and DNA repair genes.[4] Proto-oncogenes and tumor suppressor genes control the growth and division of normal cells, while DNA repair genes help fix DNA damages. Mutations in these genes create changes in chromosomes, and thus the cells become cancerous. For example, germline mutation in the *TP53* gene responsible for the tumor growth suppression causes the hereditary cancer syndrome - Li-Fraumeni syndrome. Similarly, mutations in *BRCA1* and *BRCA2* genes are associated with breast, ovarian, pancreatic, or prostate cancers among men and women. Depending on the specific cell types or fluids from which cancer originates, such as epithelial cells, bone, soft tissues, lymphocytes, etc., cancers are classified as carcinomas, sarcoma, leukemia, lymphoma, multiple myeloma, melanoma, etc.

The diagnosis and classification of cancerous cells involve multiple stages. Different cancer diagnosis techniques include laboratory tests, tumor biopsy, imaging scans, endoscopic examination, surgery, or genetic testing.[5-7] Laboratory tests are based on chemical processes that measure the level of blood glucose, fats or lipids, hormones, enzymes, electrolytes (calcium and potassium), proteins, etc., released by the organs or tissues into the blood or urine. Different types of blood tests which play an important role in monitoring and diagnosing cancer, such as complete blood count (CBC), protein testing, tumor marker test, circulating tumor cells test, etc. A CBC test determines the number of blood cells such as RBCs, WBCs, and platelets in the blood sample. It also measures the amount of hemoglobin (Hgb), the size of RBCs, and the ratio of RBCs to plasma (hematocrit) in the blood. This test can also identify conditions other than blood cancer, such as leukemia, anemia, and infections. Tumor marker tests, which

measure the level of specific proteins or genes, are usually done along with other diagnostic methods to detect and monitor cancer. Cancer cells usually produce tumor markers at elevated levels compared to the noncancerous cells of the prostate (PSA), ovary (CA 125), column (CEA), thyroid (calcitonin), liver (AFP), nervous system, or lung (NSE). Urinalysis measures the presence of sugar, protein, RBCs, WBCs, and other substances in urine and helps diagnose kidney and urothelial cancers. The inter-and intra-tumor heterogeneity associated with tumors is imageable with the aid of different biomedical imaging techniques such as perfusion X-ray computed tomography (CT), single-photon emission computed tomography (SPECT) imaging, positron emission tomography (PET), magnetic resonance imaging (MRI), ultrasound (US), and optical imaging.[8,9] These techniques target the molecular and cellular physiologies of biomolecules and are grouped as "molecular imaging." US or sonography is based on the reflection, scattering, and frequency shift of acoustic waves (high-frequency sound waves) from various organs and tissues depending on the density of tissues in that region, producing echoes. US machine thus generates real-time images of blood vessels, tissues, and organs from the bounced sound waves or echoes. Tumor tissues are less elastic than the normal tissues; hence, ultrasound elastography is useful for diagnosing breast cancer, prostate cancer, liver fibrosis, etc. Conversely, CT produces cross-sectional images of the internal organs, bones, tissues, or blood vessels with X-rays for reconstructing the 3D image and can be performed with or without exogenous contrast agents. On the other hand, MRI uses a strong magnetic field and radio waves to produce detailed anatomical 3D images of water and soft tissues, helping diagnose and monitor cancers. PET and SPECT are nuclear imaging techniques to detect biochemical and physiologic abnormalities related to cancers, which are based on the decay of radiotracers by the emission of positrons or by electron capture or gamma emission, respectively.

1.2 Liquid biopsy

Among all techniques, tissue biopsy provides reliable results for cancer detection and is considered the gold standard for diagnosis. Biological samples are obtained from the suspicious masses or irregular tissues followed by diagnosis to analyze the composition and treatment options in this method.[10,11] This is performed with imaging techniques (CT, MRI) once the mass becomes visible. Various types of biopsy techniques are used to retrieve tissue samples, such as needle biopsy, endoscopic biopsy, skin biopsy, bone marrow biopsy, and surgical

biopsy.[12] This helps to determine the origin, type, cancerous or non-cancerous cells, and the degree of aggression of cancer (on a scale of 1-4). Despite the advantages offered by tissue biopsy, there are certain risks and challenges revealed along with the recent advances in genomics and proteomics, as mentioned below:

1) It can be performed when the mass becomes visible, lowering the probability of treatment success.
2) Clinically, it has barriers to accessing certain tissue samples due to their anatomical location.
3) It is an invasive procedure and includes stress, pain, and discomfort to the patient. Thus, it cannot be performed repeatedly to monitor the disease progression and treatment efficacy.
4) It fails to provide information regarding the tumor heterogeneity which affects targeted cancer therapy.

Hence to overcome the above limitations, analysis of body fluids by liquid biopsy has emerged as the most appropriate technique for the early stage and accurate cancer detection. It offers the following advantages over traditional tissue biopsy:

1) It is a minimally invasive procedure involving a simple blood draw that causes no discomfort to the patient and thus can be performed even in an advanced cancer stage.
2) Sample for the biopsy can be easily obtained, and the procedure can be repeated to monitor the disease progression.
3) It reveals the tumor heterogeneity, which could help clinicians decide on appropriate treatment methods.

Liquid biopsy is carried out by analyzing the cancer biomarkers present in the sample isolated from various biofluids such as the saliva, blood, bile, cerebrospinal fluid (CSF), pleural effusion (PE), or urine of cancer patients (Figure 1.1).[13] The analytes in liquid biopsy include cell-free RNA (cfRNA), circulating tumor cells (CTCs), cell-free DNA (cfDNA), proteins, miRNAs, extracellular vesicles (exosomes), and metabolites. These analytes are environed by various non-analytes shredded from the normal cells that can hinder the detection of the sample of interest. In this scenario, liquid biopsy is important for the molecular analyses of tumors by its non-invasive nature. Analytes can be used as such to obtain necessary information, or they serve as the starting materials for the biomarker detection. There are several biomarkers present, such as tumor-specific proteins, metabolites or miRNAs, somatic point mutations, deletions,

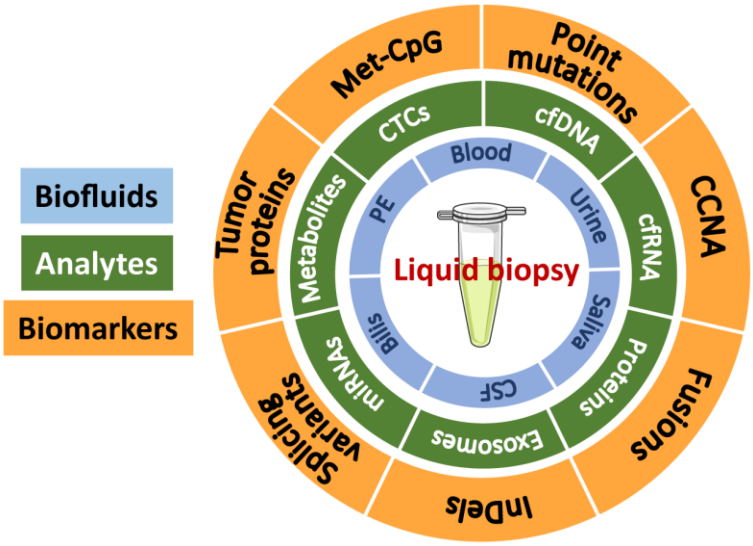

Figure 1.1. Biomarkers, analytes, and biofluids in liquid biopsy.[13]

amplifications, gene-fusions, DNA-methylated marks, etc., that depend on the analytes and tumor type. Though next-generation sequencing (NGS) has expanded the possibilities of nucleic acid-based liquid biopsies, poor analytic sensitivity often affects their detection. It requires further validation studies for clinical use. Previously, proteins from the circulating tumors were used for cancer screening and detection, but the overdiagnosis involved in this technique limits its utility.

1.3 Circulating tumor cells (CTCs)

Nevertheless, in the last decades, CTCs have marked an exponential growth as an excellent diagnostic tool among all the liquid biopsy analytes.[14] In 2004, CellSearch®, the first and only validated clinical tool, gained the U.S. Food and Drug Administration (FDA) approval to predict the prognosis of metastatic prostate, breast, and colorectal cancer patients by collecting CTCs in the blood.[15] The concept of CTC was proposed by Thomas Ashworth in 1869 with the discovery of tumor cells in the peripheral blood of a metastatic cancer patient.[16] CTCs are the cells detached from the primary tumor and invaded the blood circulation, which often results in metastasis by the engraftment at distant sites. These are resistant to anoikis as they do not bind with the extracellular matrix (ECM), making them accessible for capture and detection. They can be differentiated from the blood cells based on the morphology or epithelial markers such as epithelial adhesion molecule (EpCAM), and cytokeratin markers (CK8, CK18,

CK19).[17] But when these undergo epithelial-to-mesenchymal transition (EMT), EMT regulators such as vimentin, N-cadherin, transforming growth factor (TGF)-β, and fibronectin are developed.[18] Recent studies show that the multicellular clusters show characteristics such as the phenotype, gene expression, and the mode of spread distinct from individual CTCs. Thus, CTC clusters play a vital role in investigating metastasis.[19] Reports also confirm the acquisition of stem-cell properties and the associated markers such as CD44, KLF4, ESA, P63, and ALDH7A1 in a certain percentage of CTCs.[20] But depending on the cancer stage, CTCs are extremely rare in the blood, with one count per ~ 10^6 blood cells, with a half-life time of < 2.5 h.

1.4 CTC detection technologies

The capturing of single CTCs from the blood is extremely challenging due to their rarity and heterogeneity.[21] In the past decades, several strategies for isolating CTCs based on their physical or biological properties have been developed. The performance of various detection technologies is compared based on the capture and enrichment efficiency, throughput, cell viability, and recovery.[22] Current CTC enrichment and detection technologies are shown in Figure 1.2.

Isolation of CTCs based on physical properties relies on the physical or mechanical differences such as size, density, electric charge, or deformability between blood cells and the CTCs.[24] This technique is independent of the antigen expression on cell surfaces. The size of CTCs is usually larger (9-19 μm) than the normal cells and the technique mainly uses membrane microfilters and microfluidic sorting devices to isolate CTCs.[25] There is no biomodification step involved in this process which usually results in viable and enriched cells among 10^4 leukocytes. But the interference with leucocytes having a size of 7-9 μm, similar to a few CTCs is a limitation of this method. Also, cancer cells from the clinical samples having a size larger than CTCs lower the efficiency of this technique. Density-based CTC isolation depends on the difference in the buoyant densities of blood cells and CTCs, referred to as the density-based gradient centrifugation method.[26] Examples of this include OncoQuick®, Ficoll-Hypaque, and AccuCyte, which are designed to enrich CTCs based on the density. The limitation of this technique involves nonspecific loss of desired cells. Tumor cells with high metastatic potential show more deformability than normal cells, based on the measurement of Young's modulus. But the reduction of this parameter during the malignant transformation

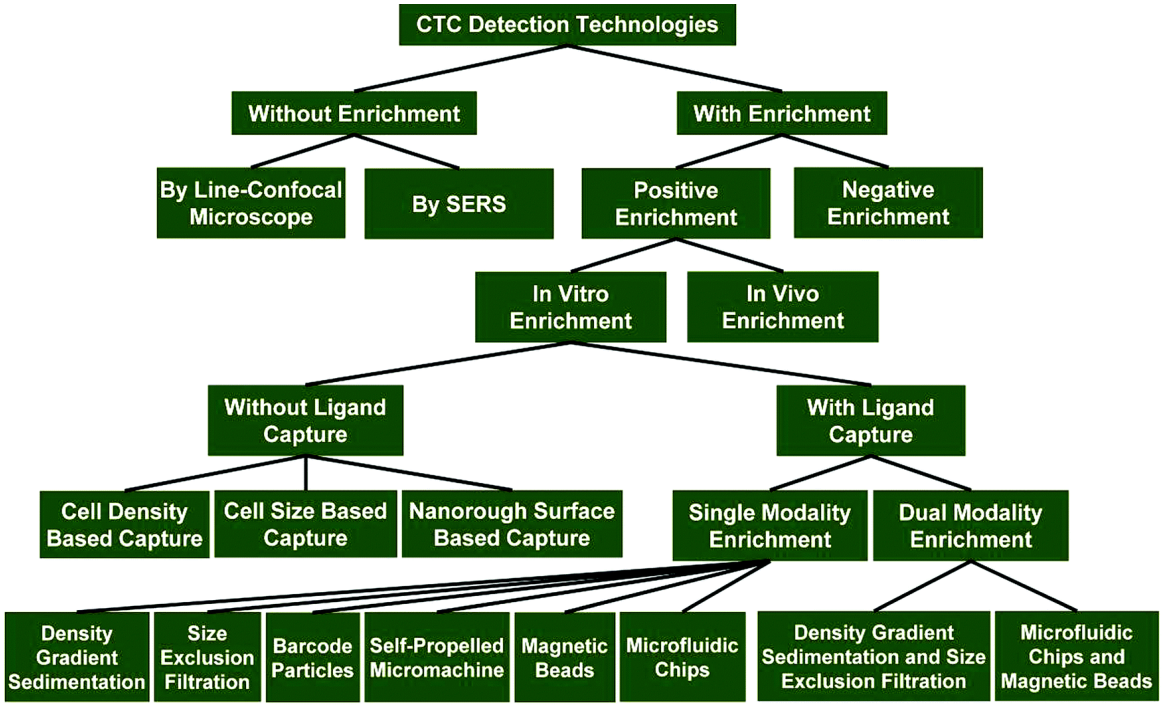

Figure 1.2. Classification of current CTC detection technologies.[23]

affects the reliability of this technique.[27] The electrical properties of CTCs vary from other cells, measured using techniques such as dielectrophoresis, impedance spectroscopy, and electrorotation.[28] Electrical measurements give information on the size, shape, morphology, membrane integrity, and cytoskeletal structure of the cells. But this method suffers from drawbacks in terms of throughput, sample processing time, and purity.

The isolation of CTCs based on the biological properties utilizes the cancer-specific biomarkers (antigens) present on the cell surfaces. These immunoaffinity-based techniques utilize either a negative enrichment or positive enrichment for the detection. Negative enrichment targets the antigens present in non-cancerous cells or blood cells such as CD45 or CD66b,[29] and EasySep is an easy-to-use kit developed by StemCell™ to capture label-free and viable cells. But low purity and collection of all heterogeneous CTCs together is a major disadvantage of this method. Positive enrichment techniques target tumor-cell-specific antigens such as EpCAM, EGFR, HER2, PSMA, CK, MUC1, etc., during the enrichment step.[30] This immunoaffinity technique utilizes antibodies bound to the surface of different substrates that specifically capture CTCs from a sample of whole blood. Examples include an immunomagnetic strategy utilizing antibody-labeled magnetic microbeads for the capture of CTCs with the help of an external magnetic force. Magnetic cell separation systems (MACS),

MagSweeper, immuno-magnetosomes (IMS), and Streptag are devices utilizing magnetic rods, magnetic nanoparticles (NPs), or magnetic nanoclusters coated with antibodies such as anti-EpCAM.[31-33] Another class of immunoaffinity devices is based on a microfluidic platform such as CTC-chip, herringbone chip, geometrically enhanced differential immunocapture (GEDI) chip, etc.[34] Though CTCs are isolated with high purity in these methods mostly by targeting the EpCAM antigen, nonmalignant epithelial cells can give false-positive results, and CTCs with non-epithelial characteristics result in false-negative results. Further, CTCs expressing mesenchymal markers formed by the EMT transition and stem cell markers cannot be detected.[35]

1.4.1 Nanomaterials-based CTC enrichment

Recently, new techniques for CTC detection using nanomaterials such as magnetic NPs, carbon nanotubes, graphene oxide (GO), quantum dots (QDs), gold NPs, polymeric NPs, silica NPs, liposomes, etc. are found to enhance the efficiency of CTC capture.[36] These materials increase the capture efficiency, and modification with CTC-targeting moieties increases the specificity and surface area for the cellular binding in the blood sample. Further, the properties of nanomaterials can be tuned for multiplexed targeting and detection, which allows the possibility of capturing heterogeneous CTCs. Among these, silica NPs have been extensively employed in biomedical applications due to their key properties such as size, uniform and tunable porosity, facile surface functionalization, bio-distribution, and -compatibility.[37] Also, it incorporates various fluorescent probes such as dyes, nanocrystals, etc., and the emission property can be manipulated by modifying the surface with these probes. Studies show the high-efficient capture of CTCs using fluorescent silica microbeads conjugated with antibodies due to their optical transparency and high density resulting in precise imaging and easy separation.[38] Wang *et al*. developed a microfluidic device consisting of a silicon nanopillar coated with EpCAM antibody attached to a polydimethylsiloxane (PDMS) substrate for CTC capture and compared the efficiency with CellSearch.[39] This device exhibited high capture rate (>95%) than the latter. Another report by Chang *et al*. developed a magnetic-fluorescent nanoprobe consisting of FITC and EpCAM functionalized magnetic mesoporous silica NPs with different morphologies (sphere, rodlike) for immunomagnetic CTCs isolation and detection among the blood cells.[40] In addition, the ability of silica nanomaterials to incorporate

various tumor-targeting ligands and photodynamic/photothermal agents make their utilization as a nano-carrier. Thus they are promising for diagnostic and therapeutic applications.

1.4.2 Quantum dots-based CTC detection

The accuracy and efficiency of CTC detection are also enhanced with various optical methods that lead to the advancement in single-cell imaging. This technique is based on the optical property of materials bound to the CTC, which increases the purity. Optical methods include fluorescence in situ hybridization (FISH), Raman spectroscopy, reflectometric interference spectroscopy (RIFS), chemiluminescence, immunofluorescence staining, etc.[41] Of these, immunofluorescence is highly preferred for accurate enumeration and detection of viable CTCs. Here, a fluorophore is attached to CTCs through antigen-antibody interaction. By suitably using a light source such as a laser for the detection of emission light, the distribution of target biomolecules or cells can be visualized.[41] Amon various fluorophores, fluorescent semiconductor nanocrystals, or QDs have achieved a breakthrough in biomedical imaging. They are exploited in many biological applications such as multiplexed cellular imaging, real-time monitoring of extracellular processes, molecular histopathology, investigation of dynamic cellular processes, Förster resonance energy transfer (FRET) studies, and cancer cell detections.[42] The high photostability and fluorescence quantum yield, broad excitation, and narrow emission promote its clinical relevance for *ex vivo* CTC detection. Among different kinds of QDs such as CdTe, CdSe, GaAs, GaN, PbSe, InAs, and InP, CdSe/ZnS core/shell QDs are prevalent in bio-imaging and -analyses. In organic solvents, highly crystalline, homogeneous, and monodispersed colloidal QDs are synthesized at high temperatures. Wide-bandgap semiconductor shells from ZnS and CdS make QDs improve the stability and feasibility of bioconjugation.[43] Also, the shells minimize the surface defect and enhance the photoluminescence quantum yields. However, the synthesis often renders hydrophobic QDs made hydrophilic by surface modifications. Further, such modifications reduce the aggregation and non-specific binding of QDs to biomolecules or cells.[43] The biocompatibility of QDs can be accomplished by ligand exchange and polymer encapsulation.[44] The ligand exchange uses bifunctional molecules like mercapto silanes, dihydrolipoic acid (DHLA), cysteine, or thioglycolic acid (TGA), whereas in encapsulation, polymers or phospholipids are used to protect the hydrophobic surface. Surface-modified QDs contain reactive functional groups like

amines, carboxylic acids, thiols, or hydroxyl groups that are useful for conjugating ligands, peptides, antibodies, nucleic acids, and other biomolecules.

Quantum confinement effect

The electrical, optical, and mechanical properties of QDs are influenced by the "quantum confinement effect" because of their peculiar tunable bandgap properties with the particle shape and size (nm order). A simplified explanation of optical excitation is given below. During photon absorption from the light source, electrons in the valence band (VB) of a semiconductor, on gaining the energy to overcome the bandgap energy (E_g), move to the conduction band (CB), creating a hole and electron in VB and CB, respectively. The charge of a hole and electron is equivalent, and the combination of them due to polarity charges and Coulomb exchange interaction results in excitons (electron-hole pairs). The electrons or excitons are tightly confined in all the three dimensions in QDs, and this effect occurs only in II-VI, III-V, and IV-VI group elements. The electron-hole (exciton) distance is called the exciton Bohr radius (or Bohr radius). Every semiconductor has a characteristic Bohr radius, and in QDs, the size of the particles is below the Bohr radius. Here, the electron-hole pair is bound by the Coulomb electrostatic interactions. Below this radius, the quantum confinement effect takes place, which leads to the formation of discrete energy levels in QDs. Considering the exciton as a hydrogen-like system, on comparing the exciton radius with Bohr radius approximation, the spatial separation of excitons is given by,

$$\mathrm{r} = \frac{\varepsilon h^2}{\pi m_r e^2}$$

where r is the radius of 3D sphere containing exciton, m_r is the reduced mass of exciton, ε is the dielectric constant of the material, e is the electron charge, and h is the Plank's constant. For most semiconductors, this value lies between 1 and 10 nm.

Semiconductor crystals of 10-100 nm show size effects, whereas nanocrystals of size <10 nm exhibit quantum size effects.[45] A bulk material has many energy states (or atoms) that lead to a continuous distribution of the band states. When the dimensions of the confining structures are larger than the de Broglie wavelength, the particle behaves as a free particle, resulting in these continuous states. But with a decrease in the number of atoms, the energy states become delocalized and confined. Also, as the particle dimension approaches the de Broglie

wavelength of electrons in the CB, the excitons become spatially confined in 3D and the electronic bands split into molecule-like discrete energy levels. Thus, the decrease in the particle size towards the nanoscale increases the energy difference between the band states (Figure 1.3) and results in quantum confinement. The density of states function describes the

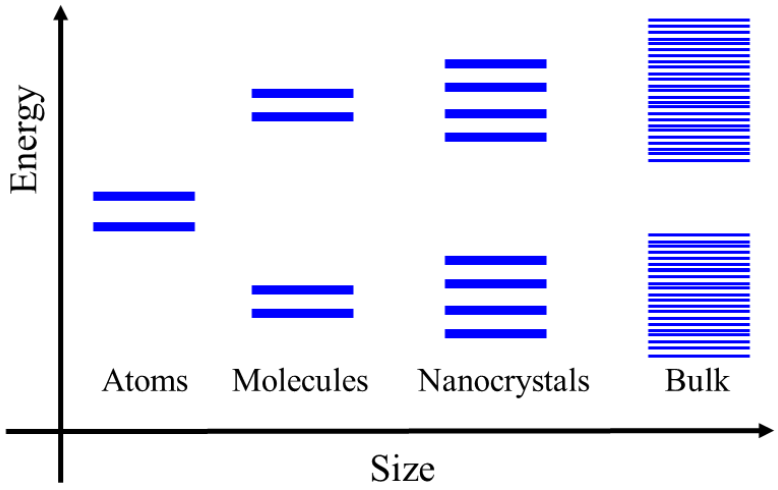

Figure 1.3. A scheme showing size-dependent bandgap energy in materials.

number of states available for filling charge carriers and determines the concentration and energy of the charge carriers in a semiconductor. The electrons in a quantum well, quantum wires, and QDs are confined in one direction (1D quantized), two directions (2D quantized), and three directions (3D quantized) and thus have freedom of movement in 2D, 1D, and 0D potential wells, respectively. Thus, a continuous *k* component changes to a discrete component with each confinement direction, characterized by quantum number *n*. The following equations represent the density of states in various systems,

$$\text{For 3D system, } \left(\frac{dN}{dE}\right) = \frac{1}{3}\frac{L^3}{\pi^2} \text{x} \frac{(2m^*)^{\frac{3}{2}}}{\hbar^3} E^{\frac{1}{2}}$$

$$\text{For 2D system, } \left(\frac{dN}{dE}\right) = \frac{L^2 m^*}{\pi\hbar^2}$$

$$\text{For 1D system, } \left(\frac{dN}{dE}\right) = \frac{(2m^*)^{\frac{1}{2}}\text{L}}{\pi\hbar E^{\frac{1}{2}}}$$

where, $\frac{dN}{dE}$ is the density per unit energy, L is the side length, and m* is the electron mass.

For 0D (QDs), there is no free motion. Since there is no *k* space to be filled with electrons, the density of states is described with the delta function as $g(E)_{0D} = 2\delta(E\text{-}E_c)$. The functional dependence on the energy of density of states is shown in Figure 1.4.

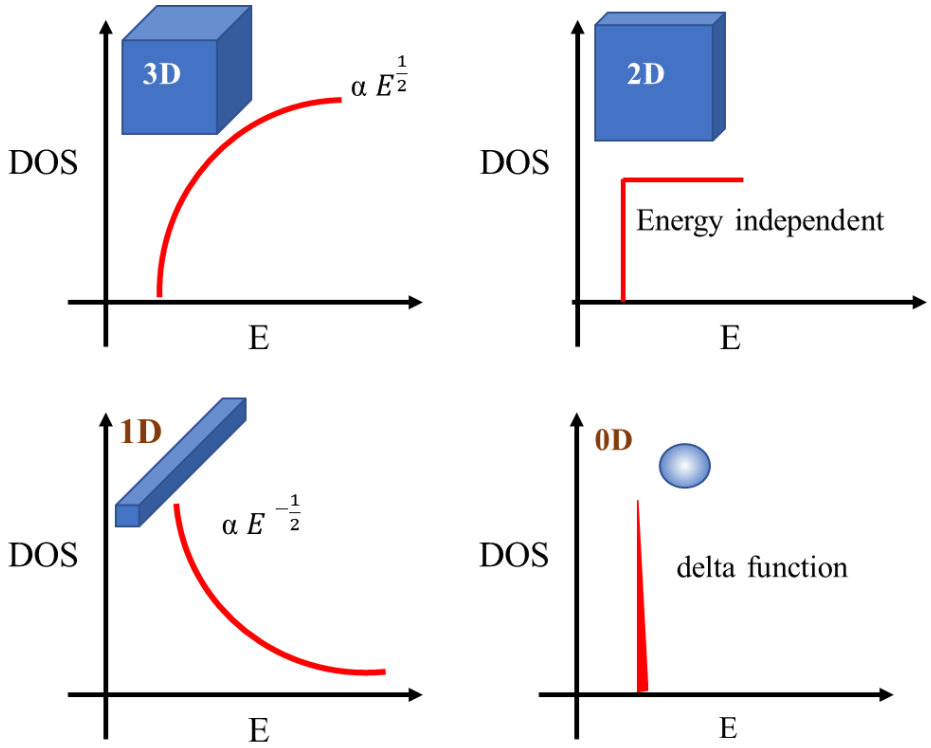

Figure 1.4. A scheme showing the electronic density of states for various materials.

Effect on the photophysical and photochemical properties of QDs

The effect of quantum confinement on the optical absorption of a QD was first explained in 1990 by Steigerwald and Brus using quantum mechanical molecular orbital calculation. At a point, the magnitude of E_g becomes smaller or comparable to the Bohr radius with a decrease in particle size. This property of semiconductors is utilized in multi-quantum well and superlattice devices, imaging systems, photocatalysis, and nonlinear optical materials. QDs show excellent optoelectronic properties compared to bulk materials due to the decreased exciton Bohr diameter. They show size-dependent optical and electrical properties in the range of a few nanometers. The quantum confinement results in the energy increase of band-to-band excitation peaks as the radii of semiconductor material are decreased relative to the Bohr radius (blue-shift).

In a weak confinement regime where the radius of particle *R* exceeds the bulk exciton Bohr radius, Coulombic force dominates. The confinement results in the shift of exciton ground energy state to higher energy levels given by,

$$\Delta E \approx \frac{\hbar^2 \pi^2}{2MR^2}$$

Here, *M* is the exciton mass given by $M = m_e^* + m_h^*$ where, m_e^* and m_h^* are the effective mass of an electron and hole, respectively. In the case of II-IV semiconductors, *R* is equal to the Bohr radius and lies in between the hole and electron Bohr radius ($a_h < R < a_e$). This is called a moderate confinement regime which is observed in small QDs. Strong quantum confinement is observed when *R* is less than both hole and electron Bohr radius. In QDs, electrons and holes are considered independent particles, and ladder-like discrete energy levels exist in the excited state. Here, Coulombic interaction is small, leading to perturbation, and the electrons and holes behave independently. The spectrum thus contains a series of lines due to the transition between various band states. The shift in energy is given by,

$$\Delta E \approx \frac{\hbar^2 \pi^2}{2\mu R^2}$$

where μ is the reduced mass of exciton given by, $\frac{1}{\mu} = \frac{1}{m_e^*} + \frac{1}{m_h^*}$

Fluorescence emission from semiconductor QDs

Luminescence occurs only in materials having non-zero bandgap energy. In direct and indirect bandgap semiconductors, it is explained by the quantum confinement effect. In a direct bandgap material such as QDs, the CB minimum and VB maximum is aligned at the zone center where k = 0. But in indirect bandgap materials such as Si, these are aligned in reciprocal space ($k \neq 0$) at the zone edge or closer. In QDs, the absorption of a suitable photon with energy >Eg creates an electron-hole pair. The VB maximum and CB minimum have the same k (wave vector) values in the initial and final electronic states. Since photons do not have momentum, the law of conservation of momentum is obeyed during the photoexcitation process. As the electron wave vector is not changed significantly during the process, the absorption process is represented by the vertical transition in the E-k diagram obeying the Franck-Condom principle. The electrons and holes accumulate in the lowest and highest energy states of CB and VB,

respectively. Thus, the energy separation between electrons and holes becomes approximately equal to E_g. The electron-hole pairs can recombine rapidly (~10^{-13} s) with the emission of a photon (fluorescence) with energy close to E_g or transfer its energy to defects or impurities within the material. Here, the fluorescence emission is a first-order process with a short lifetime in the range of 10^{-9}-10^{-8} s, and the efficiency depends on the radiative and nonradiative recombination rate. However, due to the quantum confinement effect, a particle of mass m spatially confined to a given direction (for example, x-axis) of length Δx will create uncertainty in its momentum $\hbar/\Delta x$ and increase its kinetic energy by an amount $E_{QC} \sim (\Delta p_x)^2 / 2m \sim \hbar^2 / 2m(\Delta x)^2$ (Heisenberg uncertainty principle). The particle-in-a-box analysis using Schrödinger's equation and the effective mass approximation showed the ground state quantum confinement energy, $E_{QC} \sim (3\,\hbar^2 / 8\,m^*)\,(\pi / a)^2$, where m^* is the reduced effective mass of exciton. In QDs, the quantum confinement effect becomes significant as E_{QC} becomes comparable to or greater than the thermal energy. This increases E_g with a decrease in particle size along with the simultaneous broadening of electron-hole pair state in the momentum space. Also, the probability of nonradiative recombination is decreased unless the dangling surface bonds are passivated to prevent the trap-assisted carrier recombination that causes fluorescence quenching. This results in the shifting of emission peak to high energy and a high fluorescence quantum efficiency. The fluorescence quantum efficiency/yield (ϕ_F) is defined as the ratio of the number of photons emitted to the number of photons absorbed. The relative ϕ_F of QD is given by the equation,

$$\phi_F = \phi_R \times \frac{A_R}{A_S} \times \frac{\mathrm{IF_S}}{\mathrm{IF_R}} \times \left(\frac{\mu_S^2}{\mu_R^2}\right)$$

where, ϕ_R is the fluorescence quantum yield of reference, A_R and A_S are the absorbencies of the reference and the sample at the excitation wavelength, IF_R and IF_S are the integrated fluorescence intensities of the reference and the sample, and μ_R and μ_S are the refractive indices of the solvents in which the reference and the sample are dissolved.

ϕ_F is also related to the fluorescence lifetime (τ_f). τ_f of a QD is the average lifetime spent by them in the excited state. The general relationship between the fluorescence intensity and the lifetime is

$$I = I_0 e^{-t/\tau_f}$$

where I is the intensity at time 't' and I_0 is the absolute fluorescence intensity. The absolute fluorescence lifetime (τ_0) is the value when there is no nonradiative process that competes with the excited state. It is related to the measured lifetime (τ_f) and the ϕ_F values by the equation,

$$\phi_F = \frac{\tau_f}{\tau_0}$$

Also, τ_0 is inversely proportional to the relaxation rate. Thus,

$$\tau_0 = \frac{1}{k_r}$$

$$\tau_f = \frac{1}{k_r + k_{nr}}$$

$$\therefore \phi_F = \frac{1}{k_r + k_{nr}} \div \frac{1}{k_r} = \frac{kr}{k_r + k_{nr}}$$

where k_r and k_{nr} are the excited state radiative and nonradiative relaxations rates.

1.5 Singlet oxygen ($^1O_2$)

In the 1840s, the paramagnetic property of molecular oxygen was discovered by Faraday, and based on this, Mulliken assigned the outer electronic configuration.[46] The triplet ground energy state (lowest energy) of oxygen subsequently led to the discovery of electronic configurations for the higher two excited states of singlet oxygen ($^1O_2$). These are represented in Figure 1.5.

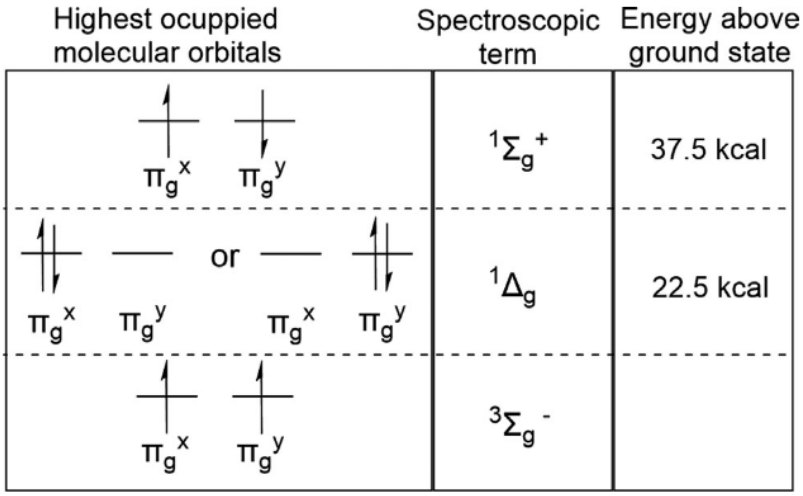

Figure 1.5. A diagram showing the electronic configuration of different states of molecular oxygen.[47]

The lifetime of $^1\Delta_g$ excited state is longer than $^1\Sigma_g^+$ which is responsible for many reactions in chemistry and biology. In 1933, Kautsky discovered the "metastable, reactive state of oxygen" by observing photochemical oxidation of leukomalachite impregnated on silica gel which was mixed with trypaflavin sensitizer adsorbed on another silica.[48] This reaction occurred only within a limited range of pressures, with maximal effect at 0.02 mmHg, and provided strong experimental evidence for $^1O_2$. But this did not provide sufficient information about the nature of $^1O_2$, and the significance of this work was later recognized in 1964 from the work of Foote and Wexler.[49] They reported the formation of intermediate in photosensitized oxidation reactions in solution as the lowest excited state of molecular oxygen ($^1\Delta_g$). This was regarded as a milestone in $^1O_2$ research. Further, Kasha and Khan also observed red chemiluminescence in the hypochlorite-peroxide reaction due to the formation of $^1O_2$. Another study discovered the $^1O_2$ *ene* products in a reaction which revealed a mean radius of $^1O_2$ diffusion of 3 cm and lifetime of ~ 1 s.

1.5.1 Effect of $^1O_2$ on biological substrates

$^1O_2$ acts as a weapon and signal against various pathogens inside the human body. Due to the high reactivity, $^1O_2$ causes the oxidation of various cellular macromolecules, which leads to a strong immune response and induces programmed cell death through many signaling pathways.

Cytotoxic effect of $^1O_2$ on biomolecules

$^1O_2$ causes the oxidation of the cell membrane. The cell membrane mainly comprises phospholipids, glycolipids, cholesterol, and proteins. In phospholipids, the sn-2 position is converted to unsaturated fatty acids by an esterification reaction which in turn oxidizes to phospholipid hydroperoxides (PLOOH) by the reaction with $^1O_2$.[50] $^1O_2$ also produce isomers of H_2O_2 by addition reactions during which the intermediates such as lipid hydroperoxides (LOOHs) and cholesterol hydroperoxides (ChOOHs) are formed. LOOHs take part in the cell signal transduction, triggering a series of electron migration or energy conversion mediated reactions (Figure 1.6a). Several peroxidases (Prx) reduce LOOHs to alcohols, whereas the remaining LOOHs are oxidized by biological oxidants to form highly reactive intermediates such as peroxides and alkoxyls. These free radicals cause damage to proteins, nucleic acids, etc. in the cells. Further, reports show $^1O_2$-mediated lipid oxidation and Fe-dependent oxidative

death of cells called ferroptosis (Figure 1.6b).[51] The activation of lipoxygenase (LOX) and hyperpolarization of mitochondrial membrane potential (MMP) results in increased ROS or calcium influx production. This effect the mitochondria or endoplasmic reticulum leading to cell apoptosis. In addition, the production of ChOOHs also aggravates the loss of MMP, causing extensive apoptosis.

$^1O_2$ also causes extensive oxidative damage to the DNA inside the nucleus, of which guanine is the preferential target. It interacts with various types of nucleobases and sugar groups, resulting in apoptosis.[52] Mitochondria in cells are associated with energy supply, cell growth,

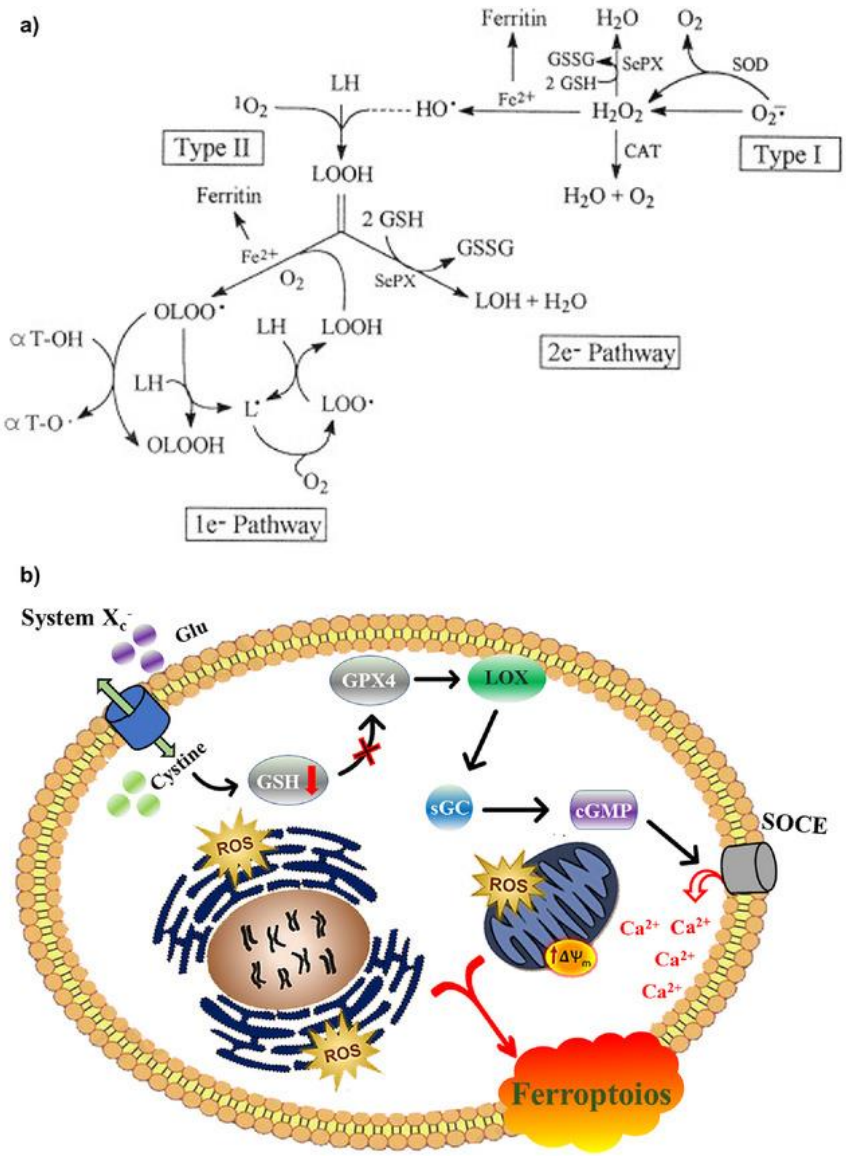

Figure 1.6. a) A scheme showing different ways of LOOH formation and turnover in photodynamic activated cells. b) Mechanism of Fe-dependent ferroptosis.[50]

and cell cycle regulation through multiple cell pathways such as differentiation, information transmission, and apoptosis. $^1O_2$ reaction with mitochondria leads to oxidative stress in cells, and the phosphorylation of a signaling pathway is inhibited, inducing apoptosis. This also affects cellular energy metabolism. Further, mitochondrial dysfunction is also observed due to the mutations in mtDNA. These oxidative reactions are fundamental to PDT in cancer therapy.

Regulation of cellular signaling by $^1O_2$

Apart from the oxidation of various cellular organelles, $^1O_2$ also plays a key role in many signaling pathways (metabolism, growth, differentiation, and death) by reversible oxidative modification.[53] The cell proliferation or apoptosis is directly correlated with the activation of P13K-Akt and its related signaling pathways. Akt (or protein kinase B) has anti-apoptotic property and is activated in many cancers. This interacts with the signaling pathway for the regulation of tumorigenesis. It promotes the epithelial-to-mesenchymal transition (EMT) of cancer cells and increases invasiveness and metastasis. It also activates the telomerase reverse transcriptase to enhance the self-healing ability of the tumor cells. PTEN (a tumor suppressor gene) is inactivated with an increase in $^1O_2$ concentration, changing the kinase-phosphatase balance, and this can promote tumor growth.

In the presence of $^1O_2$, the protective catalase produced by the tumor cells, which are controlled by the active oncogenes, is inactivated. This reactivates the HOCl and NO/peroxynitrite signaling pathways that are involved with the intracellular apoptosis signaling. This initiates apoptosis in tumor cells. $^1O_2$ can also inactivate many antioxidant enzymes by oxidizing the active histidine groups. Apoptosis signal-regulating kinase 1 (ASK1), belonging to the mitogen-activated protein kinase family, plays a crucial role in apoptosis regulation. $^1O_2$-induced oxidative stress activates ASK1, which subsequently activates the mitochondria-dependent caspase-9 and caspase-3, resulting in apoptosis. Also, B-cell lymphoma-2 (Bcl-2), an oncogene associated with apoptosis, and its modified form Bmf can undergo phosphorylation by activated ASK1 followed by further activation of Bak/Bax mediated protein receptor pathways to induce apoptosis. $^1O_2$ also induces DNA-oxidative damage and cell apoptosis by ATM-mediated activation of the atm-chk2-p53 signaling pathway (Figure 1.7).

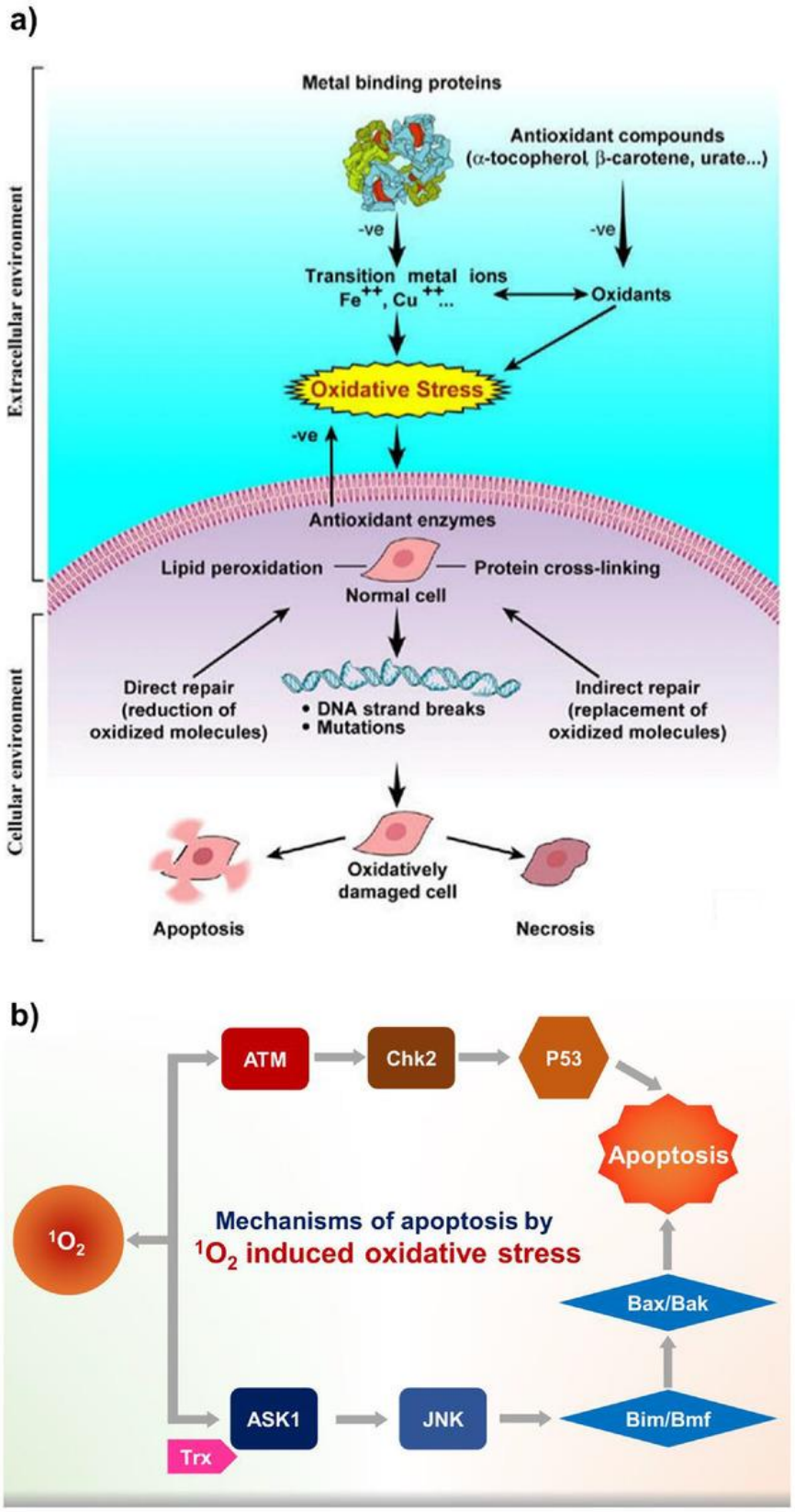

Figure 1.7. Steps involved in a) oxidative stress-mediated cell death and b) apoptosis by singlet oxygen-mediated oxidative stress.[50]

1.5.2 $^1O_2$ in cancer PDT

$^1O_2$ induced apoptotic and necrotic cells produce an immune response by activating the immune system.[54] After tumor cell death, the cell debris initiates a strong inflammatory response in the neighbouring tissues. Cells in the tumor microenvironment, such as living tumor cells, damaged endothelial cells, etc., also release a large number of inflammatory promoting media such as cytokines, histamine, arachidonic acid, etc. These enhance the activation of macrophages (innate immune activation) and produce neutrophil aggregate, which results in cancer-specific primary and memory CD8 (+) T cell responses. After the phagocytosis of dead cancer cells, adaptive immunity that is dominated by the lymphocytes will be activated, which secretes lymphokines. This further increases the ability of the immune system to kill the cells. Besides, the infiltration of neutrophils in tumor areas can promote T cell proliferation and survival. This helps to develop anti-cancer immunity.

Another mechanism promoted by $^1O_2$ is immunogenic cell death (ICD) which can eliminate the tumor.[55] ICD is induced by the endoplasmic reticulum stress (ERS) in response to an external stimulus. $^1O_2$ triggered ERS initiates damage-associated molecular patterns (DAMPs)/DANGER signaling pathways that promote the release of DAMPs. In normal cells, DAMPs play a role in physiological activities. But once secreted by the cells, they produce dangerous signals and amplify the immune function, activating the adaptive immune response of the human body. DAMPs promote the maturation of dendritic cells (DCs), which present the cancer cell antigen to primitive T cells and initiate their differentiation into effector T cells. They also simultaneously recruit the antigen-presenting cells (APCs) and promote the maturation, presenting the tumor antigens to effector T cells. Thus, the T cell adaptive immune response is enhanced to produce long-term immune memory. Hence, $^1O_2$ can efficiently regulate innate and adaptive immunity.

1.5.3 $^1O_2$ sources

Endogeneous generation of $^1O_2$

$^1O_2$ is produced in the human and animal tissues through a range of enzymatic and nonenzymatic reactions. Though the cellular DNA does not directly absorb the UVA (320-400 nm) radiation, the UV-Visible light can excite various photosensitizers (PS) in the skin such as bilirubin, melanin, flavins, vitamin K, etc. to generate ROS, particularly $^1O_2$.[56] The formation

of $^1O_2$ also takes place by the interaction of UVB radiation (290-320 nm) with different vitamins and fatty acids, and retina which contains various PSs like lipofuscin. The penetration of IRA radiation (760-1440 nm) in the skin also generates ROS, of which the superoxide anion can lead to the generation of $^1O_2$. Neutrophils also produce $^1O_2$ during multiple oxidative burst responses. Biomolecules, including proteins, nucleic acids, lipids, etc., also produce $^1O_2$ by the Russel mechanism. Here, the reaction between two peroxyl radicals (1) results in the liberation of $^1O_2$, alcohol (3), and a carbonyl compound (4) by the decomposition of tetroxide (2) intermediate (Figure 1.8). $^1O_2$ generated during phagocytosis utilizing hydrogen peroxide, superoxide anion, or hypochlorous acid act as an oxidant for the digestion of foreign species.[57] $^1O_2$ is also formed by various phenolic substances present in the human diet. For example, tyrosine amino acid generates tyrosine hydroperoxide 13 under physiological conditions and releases $^1O_2$. Tryptophan, catechol or its derivatives, etc., also contribute to $^1O_2$ release.[58] Another study showed that cytochrome c generates $^1O_2$ during the conversion of lipid-derived aldehydes to triplet carbonyl compounds.[59] Further, dietary factors such as carotenoids accumulate in the skin, preventing $^1O_2$-related photoaging due to its role as a $^1O_2$ quencher.

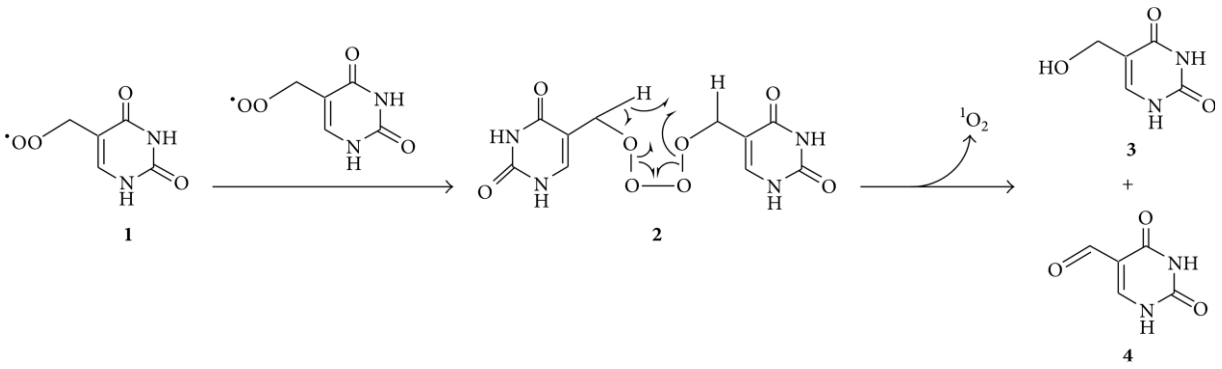

Figure 1.8. A scheme of $^1O_2$ releasing by the reaction of thymine peroxyl radicals.[56]

It also reduces the risks of diabetes. During smoking and alcohol consumption, the level of carotenoids in the skin decreases, which reduces the $^1O_2$ quenching efficiency.[60] This increases the risk of sunburn and skin cancer. In addition, the increased level of acetaldehyde in the blood during the metabolization of ethanol generates ROS. Thus, alcohol consumption can also cause gastric, colorectal, and oro-esophageal squamous cancer in humans. However, the biological utilization of $^1O_2$ is limited due to various physiological conditions that affect its production.

$^1O_2$ chemical sources

The above biological findings have led to various chemical sources of $^1O_2$. Haber-Weiss reaction is a popular technique for $^1O_2$ generation, which involve a reaction between hydrogen peroxide and superoxide anion, similar to the mechanism observed during phagocytosis.[61] But the formation of other byproducts decreases the $^1O_2$ yield. Jacob *et al*. developed a binary catalyst system of $[MoO_4]^{2-}$ and La(III) as shown below:

$$[MoO_4]^{2-} + nH_2O_2 \longrightarrow [MoO_{4-n}(O_2)_n]^{2-} + nH_2O$$

$$[MoO_{4-n}(O_2)_n]^{2-} \longrightarrow [MoO_{6-n}(O_2)_{n-2}]^{2-} + {}^1O_2$$

Here they achieved a turnover frequency of 546 h^{-1}.[62] Inorganic peroxides such as potassium perchromate, and calcium peroxide diperoxohydrate also generate $^1O_2$, which finds broad synthetic applications. Organic sources of $^1O_2$ include peracids, alkyl hydroperoxides, ozonides of triphenyl phosphites, etc. The presence of the carbonyl group is necessary for $^1O_2$ formation, such as in acyl peroxides. Thus, compounds such as cumyl peroxide, butyl hydroperoxides, etc., do not produce $^1O_2$. However, these methods have challenges associated with performing an optimum activity in physiological conditions determined by pH and temperature, robustness, and byproducts formation.[63]

$^1O_2$ molecular carriers

The molecular sources for $^1O_2$ are more stable and promising than other sources. The common and convenient strategy is the photosensitization technique that involves a photochemical excitation of sensitizer, causing the transfer of energy to the molecular oxygen, which results in $^1O_2$ generation (Type II mechanism).[64] $^1O_2$ is a strong oxidant, regio- and stereo-selective. Its unique reactivity is utilized in organic synthesis, biology, and medicines. $^1O_2$ can also be produced directly by the suitable irradiation of triplet oxygen ($^3\Sigma_g^-$) at 765 nm. It first undergoes excitation to higher energy ($^1\Sigma_g^+$) state followed by internal conversion to a lower energy $^1\Delta_g$ state. But this method has low efficiency.

Among the different molecular carriers reported, dienes or anthracenes are more common. They undergo [4+2] cycloaddition with $^1O_2$ forming the endoperoxides (EPO), which undergo decomposition either photochemically or thermally to release $^1O_2$.[65] This reaction is dependent on various factors such as the number of fused rings, electron-donating group (EDG), steric

hindrance, and solvent polarity. The presence of aromatic groups on $^1O_2$ reacting carbon mainly favor cycloaddition over other side reactions that form quinones, epoxides, hydroxy ketones, etc. Examples of reported molecular carriers of $^1O_2$ include acene derivatives of anthracene, naphthalene, etc.[66] Though $^1O_2$ produced by naphthalene derivatives shows a good yield, the half-life of $^1O_2$ is less, which prevents its utilization for biophysical studies. Studies have shown that $^1O_2$ is more stable with electron-withdrawing groups (EWG) at the 2-position of naphthene or geometric restriction around EPOs.[67] Recently, Akkaya *et al*. developed a sensitizer-sensor molecule composed of BODIPY and 2-pyridone, acting as a $^1O_2$ generator and trapping moiety.[68] The EPO formed underwent cycloreversion in the dark to generate $^1O_2$ and starting compound with a suitable irradiation source. However, compared to acenes, the cycloreversion of EPO in 2-pyridone is slow and not completely reversible. Further, incorporating photothermal agents such as gold NPs with $^1O_2$ chemical sources is also reported for dual PDT and PTT applications.

1.5.4 Enhanced $^1O_2$ generation strategies

The efficiency of a PDT process depends on $^1O_2$ quantum yield (Φ_Δ). Thus, the therapeutic efficacy depends on the following factors:

1. Intersystem crossing (ISC) rate.
2. Triplet quantum yield and lifetime
3. The energy gap between the excited singlet and triplet states of a PS.

Reports suggest that the rate of ISC is increased with spin-orbital coupling (SOC) with the introduction of heavy atoms such as metal or halogens in PSs (SOC-ISC).[69] The halogen atom's position in PS, bond length, and atomic number also affect the Φ_Δ. A decrease in the bond length, the number of halogen groups, and an increase in the atomic weight decrease the ISC rate. Further, heavy atoms in PS have several challenges, such as short lifetime, high cost, tedious synthesis, low solubility, and dark toxicity of PSs.[70] Hence, photoinduced electron transfer (PET) using electron acceptor-donor groups is an alternative method to enhance ISC. Here, the SOCT-ISC is greatly enhanced, resulting in a high triplet lifetime. Φ_Δ is also determined by the length, position, and substitution pattern of the donor-acceptor chromophore. In addition, the singlet-triplet energy-gap decreases with a significant overlap of HOMO and

LUMO orbitals of the donor and acceptor, respectively. The energy gap can also be modulated with π-π stackings, twisted geometry, ligand orientations, and polymerization reactions.

1.5.5 Fluorescence detection of $^1O_2$

The NIR phosphorescence emission of $^1O_2$ at 1270 cm^{-1} is very weak due to the competition between radiative (k_r) and nonradiative (k_{nr}) decay processes from the excited triplet state. Usually $k_{nr} > k_r$ by order of ~ 6. Thus, detecting $^1O_2$ at this emission requires sophisticated instruments that limit its practicability.

Studies suggest various molecular probes for convenient $^1O_2$ detection. These can be classified as absorption-based, photoluminescent-based, and chemiluminescent-based probes. An ideal $^1O_2$ probe should satisfy the following criteria:

1. High sensitivity and selectivity.
2. Quick response time.
3. Reversibility.

For biological detection, in addition to the above, these probes should possess low cytotoxicity, dynamic response to $^1O_2$ level, and suppressed transformation of $^1O_2$ in the biological medium. Among these, photoluminescent $^1O_2$ probes are a highly demanding and expanding topic of research due to their high sensitivity at a lower concentration. This technique finds useful mainly due to the short lifetime of ROS in the aqueous and cellular environment. The signaling features of the probes as be categorized as “always-on” or “on-off”. Former relates to the probes used in cell/tissue staining and labeling. These act as fluorescent markers for various analyses of the biological samples. But these produce high background fluorescence and thus need to attain a high signal-to-noise ratio by showing affinity towards the target cells/tissues. The latter reacts with the analyte to produce significant differences in the output signal. The performance of on-off probes depends on excited-state phenomena such as ET, charge transfer (CT), aggregation-induced emission (AIE), resonance and exchange energy transfer, etc.[71] Many commercial $^1O_2$ probes such as Singlet Oxygen Sensor Green (SOSG), Si-DMA, 1,3-Diphenylisobenzofuran (DPBF), AlphaScreen, etc. are available. There are several ways to achieve fluorescence signaling (Figure 1.9). ET between a chromophore and $^1O_2$ receptor proceeds through a non-fluorescent charge-separated state before undergoing charge

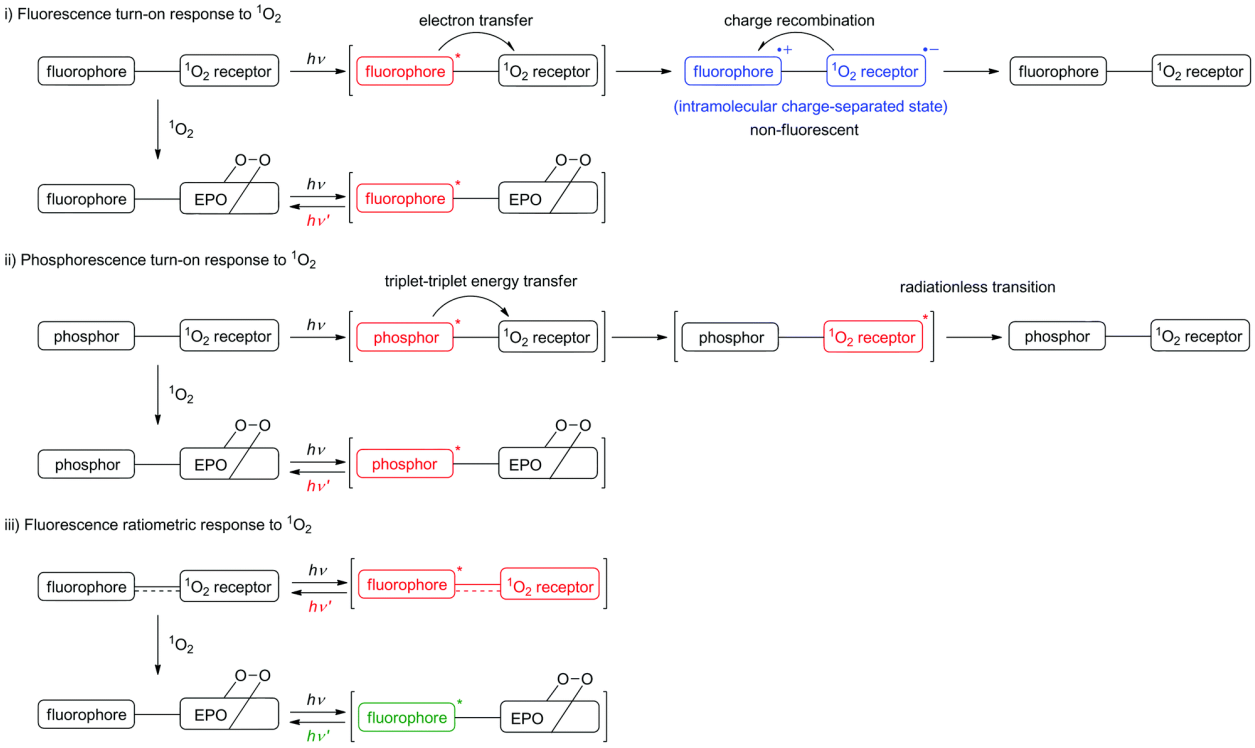

Figure 1.9. A scheme showing various methods of creating photoluminescent $^1O_2$ probes.[71]

recombination. EPO formed in PET has a negative driving force towards ET, thus blocking the ET.[72] This results in the fluorescence emission of the chromophore. Another method is based on the triplet-triplet energy transfer (TTET) between a phosphor and $^1O_2$ receptor. Here, the triplet state of the receptor is lower than phosphor, which quenches the phosphorescence due to TTET. The formation of EPO abrogates this, resulting in the phosphorescence of the phosphor. Further, $^1O_2$ reaction with π-conjugated receptor and fluorophore will decrease the π-conjugation length. Thus, a hypsochromic shift in the fluorescence emission is observed here. The photoluminescent $^1O_2$ probes can be either unimodal or ratiometric.[73] Unimodal corresponds to the transitions recorded from a single chromophore. Ratiometric probes consist of a ROS reacting moiety ($^1O_2$ receptor) and a luminescent moiety acting as the reference and producing fluorescence changes. The spectra of these probes are at least bimodal. These probes are classified depending on the sensing mechanism, signaling mode, and spectral chromaticity and apply to both NPs and small molecules. Anthracene-based $^1O_2$ probes are widely investigated for biological applications as it has a rich electron density (Figure 1.10). Examples of such dyads include a conjugate of dimethyl anthracene and fluorescein.[71] The addition of $^1O_2$ during PET blocks the intramolecular ET and releases the fluorescence. A BODIPY-

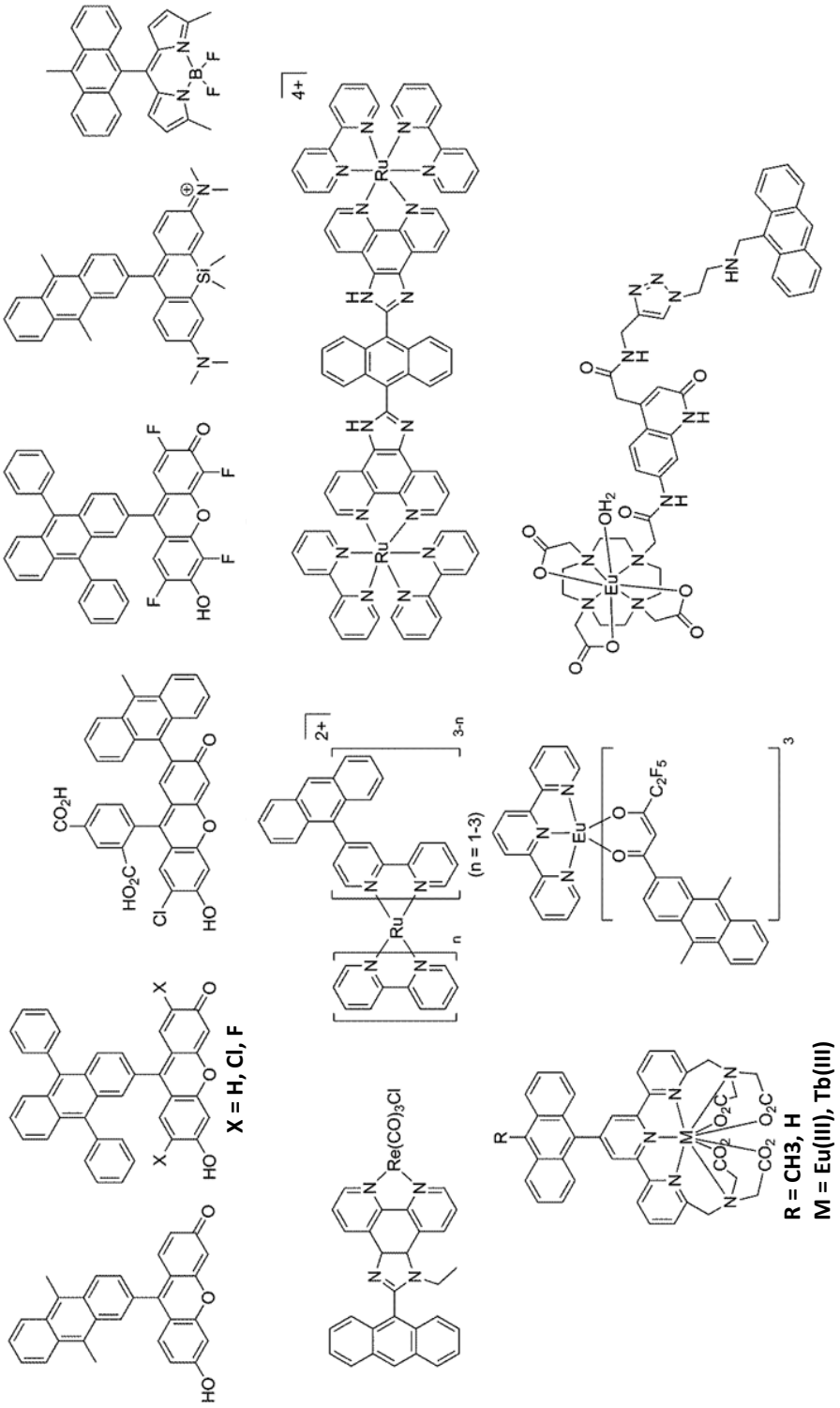

Figure 1.10. A diagram showing different anthracene-based $^1O_2$ probes.[71]

anthracene conjugate was also developed recently for $^1O_2$ detection that showed a fast ISC due to photoinduced charge separation.[74] Also, 9-[2-(3-carboxy-9,10-dimethyl) anthryl]-6-hydroxy-3H-xanthen-3-one (DMAX) for $^1O_2$ detection in biological samples was reported, which

showed improved solubility and sensitivity.[75] It showed a good fluorescence turn-on feature on forming EPO. $^1O_2$ probes utilizing lanthanide complexes are also developed to increase the luminescence lifetime of EPO, water solubility, and fluorescence enhancement.[76] But many of the fluorescent probes suffer from several drawbacks, including undesired photooxidation, $^1O_2$ self-sensitization, pH dependence, low sensitivity, low fluorescence quantum yield, etc. Lanthanide-based probes are excited by UV light which causes damage to the tissues/cells and thus has limited biological utilization. In addition, various phosphorescence-based $^1O_2$ probes based on transition metals such as rhenium (Re), ruthenium (Ru), and dinuclear Ru(II) complex with a different number of anthracene moieties are also studied.[77] But these probes also suffer from self-sensitization.

1.6 Motivation

Several diagnostic, imaging, and therapeutic techniques are introduced in every phase of cancer management. In the past decades, NPs have emerged as a promising tool for cancer theranostics due to their intrinsic molecular properties and multifunctionalities. Despite the substantial signs of progress, certain limitations restrain their utility for cancer detection and therapeutic studies. The present liquid biopsy-based CTC detection techniques are unimodal and mostly target the EpCAM markers on the cell surface. Thus, a heterogeneous CTC population with non-epithelial phenotypes gives false-negative results. With the wide utilization of magnetic-silica microbeads for CTC detection, the application of external gradient forces during separation, and possible internalization of beads by the cells due to size resemblance will affect the analysis and viability of the CTCs. Further, NPs loaded with various singlet oxygen molecular probes have potential in photodynamic cancer therapies. Among these, anthracene derivatives conjugated to fluorophores are commonly used due to their electron-rich nature, $^1O_2$ reactivity, and clean reaction. However, the fluorescence sensitivity of some sensors is very poor and undergoes self-sensitization on excitation. In addition, a few sensors emit in the visible-light region overlapping with the commonly used photosensitizers, which affects the $^1O_2$ detection studies. Photostability is another limiting factor of the sensors.

Hence, the main focus of my research is to develop nano-bioconjugates for a multimodal CTC detection and a highly sensitive $^1O_2$ sensor encompassed in nano-scaffolds for efficient $^1O_2$ storing, sensing, and releasing for phototherapeutic application. Thus, I introduced a CTC detection technology combining the mesenchymal antigen targeting immunosilica particles and

spectrotemporal resolved fluorescence micro-spectroscopic detection method for an error-free capture and detection of CTCs among the blood cells without any external gradient force. Further, I synthesized a sensor-sensitizer-peptide-silica nanoassembly for intracellular $^1O_2$ storage, sensing, and controlled release. The anthracene-based sensor demonstrated good stability and high fluorescence turn-on efficiency upon reaction with $^1O_2$ in the ensemble, single-particle, and living cells. In addition, the co-fluorescence from the sensor and sensitizer helped cell imaging, and $^1O_2$ promoted cell death. Thus, the new multimodal CTC detection and intracellular $^1O_2$ release and detection highlight the prospects of nanobioconjuagtes for advanced cancer screening and image-guided PDT.

1.7 References

1. H. Sung, J. Ferlay, R. L. Siegel, M. Laversanne, I. Soerjomataram et al. Global cancer statistics 2020: GLOBOCAN estimates of incidence and mortality worldwide for 36 cancers in 185 countries, *CA Cancer J. Clin.* **2021**, *71*, 209.

2. T. L. Roth, A. Marson, Genetic disease and therapy, *Annu. Rev. Pathol. Mech. Dis.* **2021**, *16*, 145.

3. H. Takeshima, T. Ushijima, Accumulation of genetic and epigenetic alterations in normal cells and cancer risk, *NPG Precis. Onc.* **2019**, *3* (7).

4. H. Takeshima, T. Niwa, T. Takahashi, M. Wakabayashi, S. Yamashita et al. Frequent involvement of chromatin remodeler alterations in gastric field cancerization, *Cancer Lett*. **2015**, *357*, 328.

5. S. H. Jafari, Z. Saadatpour, A. Salmaninejad, F. Momeni, M. Mokhtari et al. Breast cancer diagnosis: Imaging techniques and biochemicalmarkers, *J. Cell Physiol*. **2018**, *233*, 5200.

6. R. Lambert, Endoscopy in screening for digestive cancer, *World J. Gastrointest. Endosc.* **2012**, *4*, 518.

7. R. R. Alfano, Advances in optical biopsy for cancer diagnosis, *Technol. Cancer. Res. Treat.* **2011**, *10* (2).

8. J. V. Frangioni, New technologies for human cancer imaging, *J. Clin. Oncol.* **2008**, *26*, 4012.

9. L. Fass, Imaging and cancer:A review, *Mol. Oncol.* **2008**, *2*, 115.

10. C. Manneli, Tissue vs liquid biopsy for cancer detection: Ethical issues, *J. Bioeth. Inq.* **2019**, *16*, 551.

11. M. Ilie, P. Hofman, Pros: Can tissue biopsy be replaced by liquid biopsy? *Trans. Lung Cancer Res.* **2016**, *5,* 420.

12. T. Hirahata, R. Quraish, A. Quraish, S. Quraish, M. Naz al. Liquid biopsy: A distinctive approach to the diagnosis and prognosis of cancer, *Cancer Inform.* **2022**, *21*, 1.

13. M. Arechederra, M. A. Avila, C. Berasain, Liquid biopsy for cancer management: a revolutionary but still limited new tool for precision medicine, *Adv. Lab. Med.* **2020**, *1*.

14. E. Kilgour, D. G. Rothwell, G. Brady, C. Dive, Liquid biopsy-based biomarkers of treatment response and resistance, *Cancer Cell* **2020**, *37*, 485.

15. A. J. Rushton, G. Nteliopoulos, J. A. Shaw, R. C. Coombes, A review of circulating tumour cell enrichment technologies, *Cancers* **2021**, *13,* 970.

16. H. Zhang, X. Lin, Y. Huang, M. Wang, C. Cen et al. Detection methods and clinical applications of circulating tumor cells in breast cancer, *Front. Oncol.* **2021**, *11*, 652253.

17. M. G. Krebs, J. M. Hou, R. Sloane, L. Lancashire, L. Priest et al. Analysis of circulating tumor cells in patients with non-small lung cancer using epithelial marker dependent and-independent approaches, *J. Thorac. Oncol.* **2012**, *7,* 306.

18. A. J. Armstrong, M. S. Marengo, S. Oltean, G. Kemeny, R. L. Bitting et al. Circulating tumor cells from patients with advanced prostate and breast cancer display both epithelial and mesenchymal markers, *Mol. Cancer Res.* **2011**, *9*, 997.

19. R. Pineiro, I. M. Pena, R. L. Lopez, Relevance of CTC clusters in breast cancer metastasis, *Adv. Exp. Med. Biol.* **2020**, *1220,* 93.

20. Y. Ming, Y. Li, H. Xing, M. Luo, Z. Li et al. Circulating tumor cells: from theory to nanotechnology-based detection, *Front. Pharmacol.* **2017**, *8.*

21. E. Rossi, R. Zamarchi, Single-cell analysis of circulating tumor cells: how far have we come in the -omics era? *Front. Genet.* **2019**, *10*, 958.

22. P. Banko, S. Y. Lee, V. Nagygyorgy, M. Zrinyi, C. H. Chae, D. H. Cho, A. Telekes, Technologies for circulating tumor cell separation from whole blood, *J. Hematol. Oncol. Pharm.* **2019**, *12* (48).

23. Z. Shen, A. Wu, X. Chen, Current detection technologies for circulating tumor cells, *Chem. Soc. Rev.* **2017,** *46*, 2038.

24. R. A. Harouaka, M. Nisic, S. Y. Zheng, Circulating tumor cell enrichment based on physical properties, *J. Lab. Autom.* **2013**, *18*, 455.

25. S. Khetani, M. Mohammadi, A. S. Nezhad, Filter-based isolation, enrichment, and characterization of circulating tumor cells, *Biotechnol. Bioeng*. **2018**, *115*, 2504.

26. Q. Huang, F. B. Wang, C. H. Yuan, Z. He, L. Rao et al. Gelatin nanoparticle-coated silicon beads for density-selective capture and release of heterogeneous circulating tumor cells with high purity, *Theranostics* **2018,** *8*, 1624.

27. Z. Liu, R. Chen, Y. Li, J. Liu, P. Wang et al. Integrated microfluidic chip for efficient isolation and deformability analysis of circulating tumor cells, *Adv. Biosyst.* **2018**, *2*(10), 1800200.

28. P. R. C. Gascoyne, S. Shim, Isolation of circulating tumor cells by dielectrophoresis, *Cancers* **2014**, *6,* 545.

29. C. H. Chu, R. Liu, T. O. Ahmadov, B. E. Swain, M. Boya et al. Negative enrichment of circulating tumor cells from unmanipulated whole blood with a 3D printed device, *Sci. Rep.* **2021**, *11,* 20583.

30. X. Li, Y. Li, W. Shao, Z. Li, R. Zhao, Strategies for enrichment of circulating tumor cells, *Trans. Cancer Res.* **2020**, *9,* 2012.

31. A. Woestemeier, K. H. Effenberger, K. F. Karstens, L. Konczalla, T. Ghadban et al. Clinical relevance of circulating tumor cells in esophageal cancer detected by a combined macs enrichment method, *Cancers* **2020**, *12,* 718.

32. A. Gribko, J. Stiefel, L. Liebetanz, S. M. Nagel, J. Kunzel et al. IsoMAG—An automated system for the immunomagnetic isolation of squamous cell carcinoma-derived circulating tumor cells, *Diagnostics* **2021**, *11,* 2040.

33. L. Wu, X. Xu, B. Sharma, W. Wang, X. Qu, Beyond Capture: Circulating Tumor Cell Release and Single-Cell Analysis, *Small Methods* **2019**, *3,* 1800544.

34. A. J. Rushton, G. Nteliopoulos, J. A. Shaw, R. C. Coombes, A review of circulating tumour cell enrichment technologies, *Cancers* **2021**, *13,* 970.

35. R. G. Austin, T. J. Huang, M. Wu, A. J. Armstrong, T. Zhang, Clinical utility of non-EpCAM based circulating tumor cell assays, *Adv. Drug Deliv. Rev.* **2018,** *125,* 132.

36. Y. Liu, R. Li, L. Zhang, S. Guo, Nanomaterial-based immunocapture platforms for the recognition, isolation, and detection of circulating tumor cells, *Bioeng. Biotechnol.* **2022**, *10,* 850241.

37. J. H. Kim, H. H. Chung, M. S. Jeong, M. R. Song, K. W. Kang et al. One-step detection of circulating tumor cells in ovarian cancer using enhanced fluorescent silica nanoparticles, *Int. J. Nanomedicine* **2013**, *8,* 2247.

38. C. L. O'Connell, R. Nooney, C. McDonagh, Cyanine5-doped silica nanoparticles as ultra-bright immunospecific labels for model circulating tumour cells in flow cytometry and microscopy, *Biosens. Bioelectron.* **2017**, *91,* 190.

39. S. Wang, K. Liu, J. Liu, Z. T. F. Yu, X. Xu et al. Highly efficient capture of circulating tumor cells using nanostructured silicon substrates with integrated chaotic micromixers, *Angew. Chem. Int. Ed.* **2011**, *50*, 3084.

40. Z. Chang, Z. Wang, D. Shao, J. Yue, H. Xing et al. Shape engineering boosts magnetic mesoporous silica nanoparticle-based isolation and detection of circulating tumor cells, A*CS Appl. Mater. Interfaces* **2018**, *10,* 10656.

41. S. Bakhtiaridoost, H. Habibiyan, H. Ghafoorifard, Detection, manipulation and post processing of circulating tumor cells using optical techniques, *Mod. Phys. Lett. B* **2015**, *29*, 1530010.

42. S. M. A. Färkkilä, E. T. Kiers, R. Jaaniso, U. Mäeorg, R. M. Leblanc, K. K. Treseder, Z. Kang, L. Tedersoo, Fluorescent nanoparticles as tools in ecology and physiology, *Biol. Rev.* **2021**, *96*, 2392.

43. V. Biju, T. Itoh, A. Anas, A. Sujith, M. Ishikawa, Semiconductor quantum dots and metal nanoparticles: syntheses, optical properties, and biological applications, *Anal. Bioanal. Chem.* **2008**, *391*, 2469.

44. X. Hu, P. Zrazhevskiy, X. Gao, Encapsulation of single quantum dots with mesoporous silica, *Ann. Biomed. Eng.* **2009**, *37*, 1960.

45. Y. Z. Hu, S. W. Koch, Quantum confinement and coulomb effects in semiconductor quantum dots, *Mod. Phys. Lett. B* **1990**, *4*, 1009.

46. A. A. Krasnovsky, Primary mechanisms of photoactivation of molecular oxygen. history of development and the modern status of research, *Biochemistry* **2007**, *72*, 1065.

47. M. Orfanopoulos, Singlet oxygen: discovery, chemistry, C_{60}-sensitization, *Photochem. Photobiol.* **2021**, *97*, 1182.

48. A. A. Krasnovsky, Singlet molecular oxygen: early history of spectroscopic and photochemical studies with contributions of a.n. terenin and terenin's school, *J. Photochem. Photobiol. A: Chem.* **2018**, *354*,11.

49. A. Greer, Christopher Foote's discovery of the role of singlet oxygen [1O2 (1Delta g)] in photosensitized oxidation reactions, *Acc. Chem. Res.***2006**, *39*, 797.

50. Z. Y. Jin, H. Fatima, Y. Zhang, Z. Shao, X. J. Chen, Recent advances in bio-compatible oxygen singletgeneration and its tumor treatment, *Adv. Therap*. **2022**, *5*, 2100176.

51. X. Chen, C. Yu, R. Kang, D. Tang, Iron Metabolism in Ferroptosis, *Front. Cell Dev. Biol.* **2020**, *8*, 590226.

52. M. Simon, H. Van Vunakis, The photodynamic reaction of methylene blue with deoxyribonucleic acid, *J. Mol. Biol*. **1962**, *4*, 488.

53. M. Riethmuller, N. Burgur, G. Bauer, Singlet oxygen treatment of tumor cells triggers extracellular singlet oxygen generation, catalase inactivation and reactivation of intercellular apoptosis-inducing signaling, *Redox. Biol.* **2015**, *6*, 157.

54. C. Nathan, A. C. Bussel, Beyond oxidative stress: an immunologist's guide to reactive oxygen species, *Nat. Rev. Immunol.* **2013**, *13*, 349.

55. G. Bauer, D. Sersenova, D. B. Graves, Z. Machala, Dynamics of singlet oxygen-triggered, RONS-based apoptosis induction after treatment of tumor cells with cold atmospheric plasma or plasma-activated medium, *Sci. Rep.* **2019,** *9*, 13931.

56. A. N. Onyango, Endogenous generation of singlet oxygen and ozone in human and animal tissues: mechanisms, biological significance, and influence of dietary components, *Oxid. Med. Cell. Longev.* **2016**, *2016*, 2398573.

57. M. B. Hampton, A. J. Kettle, C. C. Winterbourn, Inside the neutrophil phagosome: oxidants, myeloperoxidase, and bacterial killing, *Blood* **1998**, *92*, 3007.

58. G. F. Fedorova, A. V. Trofimoz, R. F. Vasilev, T. L. Veprinstev, Peroxy-radical-mediated chemiluminescence: mechanistic diversity and fundamentals for antioxidant assay, *ARKIVOC* **2007,** *8*, 163.

59. D. Takagi, S. Takumi, M. Hashiguchi, T. Sejima, C. Miyake, Superoxide and singlet oxygen produced within the thylakoid membranes both cause photosystem I photoinhibition, *Plant. Physiol*. **2016**, *171*, 1626.

60. K. Aoki, Y. Ito, R. Sasaki, M. Ohtani, N. Hamajima, A. Asano, Smoking, alcohol drinking and serum carotenoids levels, *Jpn. J. Cancer Res.* **1987**, *78*, 1049.

61. A. U. Khan, M. Kasha, Singlet molecular oxygen in the Haber-Weiss reaction, *Proc. Natl. Acad. Sci. U.S.A.* **1994**, *91*, 12365.

62. J. Wahlen, D. E. D. Vos, M. H. Groothaert, V. Nardello, J. M. Aubry et al. Synergism between molybdenum and lanthanum in the disproportionation of hydrogen peroxide into singlet oxygen, *J. Am. Chem. Soc*. **2005**, *127*, 17166.

63. R. L. Jensen, J. Arnbjerg, P. R. Ogilby, Temperature effects on the solvent-dependent deactivation of singlet oxygen, *J. Am. Chem. Soc.* **2010**, *132*, 8098.

64. A. P. Castano, T. N. Demidova, M. R. Hamblin, Mechanisms in photodynamic therapy: part one-photosensitizers, photochemistry and cellular localization, *Photodiagnosis Photodyn. Ther*, **2004**, *1*, 279.

65. J. M. Aubry, C. Pierlot, J. Rigaudy, R. Schmidt, Reversible binding of oxygen to aromatic compounds, *Acc. Chem. Res.* **2003**, *36*, 668.

66. S. Dong, A. Ong, C. Chi, Photochemistry of various acene based molecules, *J. Photochem. Photobiol. C: Photochem. Rev.* **2019**, *38*, 27.

67. M. Klaper, T. Linker, New singlet oxygen donors based on naphthalenes: synthesis, physical chemical data, and improved stability, *Eur. J. Chem.* **2015**, *21*, 8569.

68. I. S. Turan, F. P. Cakmak, D. C. Yildirim, R. C. Atalay, Near-IR absorbing BODIPY derivatives as glutathione-activated photosensitizers for selective photodynamic action, *Eur. J. Chem.* **2014**, *20*, 16088.

69. A. R. Serrano, V. R. Constapel, M. C. Daza, M. Doerr, C. M. Marian, Internal heavy atom effects in phenothiazinium dyes: enhancement of intersystem crossing *via* vibronic spin-orbit coupling, *Phys. Chem. Chem. Phys.* **2015**, *17*, 11350.

70. Z. Wang, M. Ivanov, Y. Gao, L. Bussotti, P. Foggi et al. Spin–orbit charge-transfer intersystem crossing (ISC) in compact electron donor–acceptor dyads: ISC mechanism

and application as novel and potent photodynamic therapy reagents, *Eur. J. Chem.* **2019**, *26*, 1091.

71. Y. You, Chemical tools for the generation and detection of singlet oxygen, *Org. Biomol. Chem*. **2018**, *16*, 4044.

72. K. Murotomi, A. Umeno, S. Sugino, Y. Yoshida, Quantitative kinetics of intracellular singlet oxygen generation using a fluorescence probe, *Sci. Rep.* **2020**, *10*, 10616.

73. J. Herman, Y. Zhang, V. Castranova, S. L. Neal, Emerging technologies for optical spectral detection of reactive oxygen species, *Anal. Bioanal. Chem.* **2018**, *410*, 6079.

74. M. A. Filatov, S. Karuthedath, P. M. Polestshuk, H. Savoie, K. J. Flanagan et al. Generation of triplet excited states via photoinduced electron transfer in meso-anthra-BODIPY: fluorogenic response toward singlet oxygen in solution and in vitro, *J. Am. Chem. Soc*. **2017**, *139*, 6282.

75. K. Tanaka, T. Miura, N. Umezawa, Y. Urano, K. Kikuchi et al. Rational design of fluorescein-based fluorescence probes. mechanism-based design of a maximum fluorescence probe for singlet oxygen, *J. Am. Chem. Soc.* **2001**, *123*, 2530.

76. J. X. Zhang, W. L. Chan, C. Xie, Y. Zhou, H. F. Chau et al. Impressive near-infrared brightness and singlet oxygen generation from strategic lanthanide-porphyrin double-decker complexes in aqueous solution, *Light Sci. Appl.* **2019**, *8*, 46.

77. H. Wu, Q. Song, G. Ran, X. Lu, B. Xu, Recent developments in the detection of singlet oxygen with molecular spectroscopic methods, *Trends Anal. Chem.* **2011**, *30*, 133.

Chapter 2

Experiments

In this chapter, I have compiled the preparation and characterization of sensor molecules, quantum dots, and nanobioconjugates. Also, I outline the cell culture, cell labeling, and cell imaging techniques in addition to the various instruments used. The chemicals and reagents used for my research are listed under the Materials section. In the methods section, I discuss the preparation of different antibodies-functionalized silica microparticles. The size and morphology of the silica particles were examined by scanning electron microscopy. The general procedure for mammalian cell culture is also discussed. The procedures for cell labeling using the nucleus staining dye, different QD-antibody conjugates, and the subsequent attachment of labeled cells on the surface of antibody functionalized silica microparticles are explained. This approach selectively attaches cancer cells to the surface of silica microparticles. With the help of time-resolved fluorescence spectroscopy, I performed the immunohistochemistry to distinguish the cancer cells on silica microparticles from the peripheral blood mononuclear cells (PBMCs). The spectrally and temporally resolved photocount maps help determine the levels of different antigens in the cells and distinguish the cancer cells from PBMCs. Next, I report the procedures for the synthesis of a singlet oxygen ($^1O_2$) sensor, incorporation of the sensor, and sensitizers such as tetrakis(4-carboxyphenyl)porphyrin (TCPP) and quantum dot 655 (QD655) into the silica microparticles covalently, and the conjugation of a cell-penetrating peptide RGD to the sensor-sensitizer-silica nanoassembly. The sensor is characterized by proton and carbon nuclear magnetic resonance (NMR) spectroscopy, which also helps determine the structure of the reaction intermediate. The $^1O_2$ sensing and releasing potentials of the sensor in the ensemble solution phase is realized from the steady-state absorption and fluorescence spectroscopic results. The $^1O_2$ generating-caging-releasing-sensing properties of the nanoassembly in the presence of a photosensitizer is studied through single-particle microspectroscopy measurements. The ability of the sensor embedded in the nanoassembly to release $^1O_2$ intracellularly is confirmed by confocal laser scanning microscopic imaging.

2.1 Materials

All chemicals used were of analytical grade, and the reagent grade solvents were obtained from FUJIFILM Wako. Mesoporous silica particles (FUJIFILM Wako), silica nanoparticles (FUJIFILM Wako), streptavidin (FUJIFILM Wako), phosphate buffered saline (PBS, FUJIFILM Wako), (3-aminopropyl)triethoxysilane (APTES, TCI), (D/L) biotin *N*-hydroxysuccinimide ester (biotin-NHS, Sigma Aldrich), anti-EGFR-ab (Sigma Aldrich), biotin-anti-EpCAM-ab (BioLegend), anti-CD44-ab (Sony), Alexa Fluor®488 anti-CD44-ab (Sony), streptavidin-QD 585/655-conjugate (ThermoFisher Scientific), Dulbecco's Modified Eagle Medium (DMEM, high glucose, ThermoFisher Scientific), Roswell Park Memorial Institute (RPMI) 1640 medium (ThermoFisher Scientific), fetal bovine serum (FBS, ThermoFisher Scientific), penicillin/streptomycin (P/S, ThermoFisher Scientific), trypsin (ThermoFisher Scientific), Syto-13/25 (ThermoFisher Scientific), potassium carbonate (K_2CO_3, FUJIFILM Wako), 4-(4,6-Dimethoxy-1,3,5-triazin-2-yl)-4-methylmorpholinium chloride (DMT-MM, FUJIFILM Wako), 7-amino-4-methyl coumarin (TCI), *N*,*N*-dioctylamine (TCI), 9,10-bis(chloromethyl)anthracene (TCI), tetrakis(4-carboxyphenyl)porphyrin (TCPP, TCI), RGD-SH (CDCRGDCFC, GenScript), sulfosuccinimidyl 4-(N-maleimidomethyl)cyclohexane-1-carboxylate (Sulfo-SMCC, ThermoFisher Scientific) and MCF7 and HeLa cells (RIKEN cell bank).

2.2 Methods

2.2.1 Preparation of antibody-functionalized silica microparticles

Steps involved in functionalizing silica microparticles with antibodies are shown in Figure 2.1. Mesoporous silica microparticles (2 mg, 75 ~ 150 μm) were added to 25 μL of an APTES solution (1 wt% APTES, 80 wt% acetone, 19 wt% water) in a microtube and reacted in a shaker at RT for 30 min.[1] The settled particles were washed using acetone and PBS and resuspended in PBS. Biotin-NHS ester (10 eq.) in a PBS solution was added to the amino-functionalized silica, reacted at RT by up-down flipping the microtube for 30 min, and washed with PBS. Next, streptavidin (12.5 eq.) was added, reacted at RT for 30 min, and washed with PBS. Separately, biotinylated anti-human CD44 (30:1 eq.) in PBS solution was added to the streptavidin-silica microparticles and reacted at RT for 30 min by continuous up-down flipping. The antibody functionalized silica beads were washed with PBS, resuspended in PBS, and

stored at 4 °C until use. Similarly, monoclonal anti-EGFR-ab conjugated silica microparticles were also prepared.

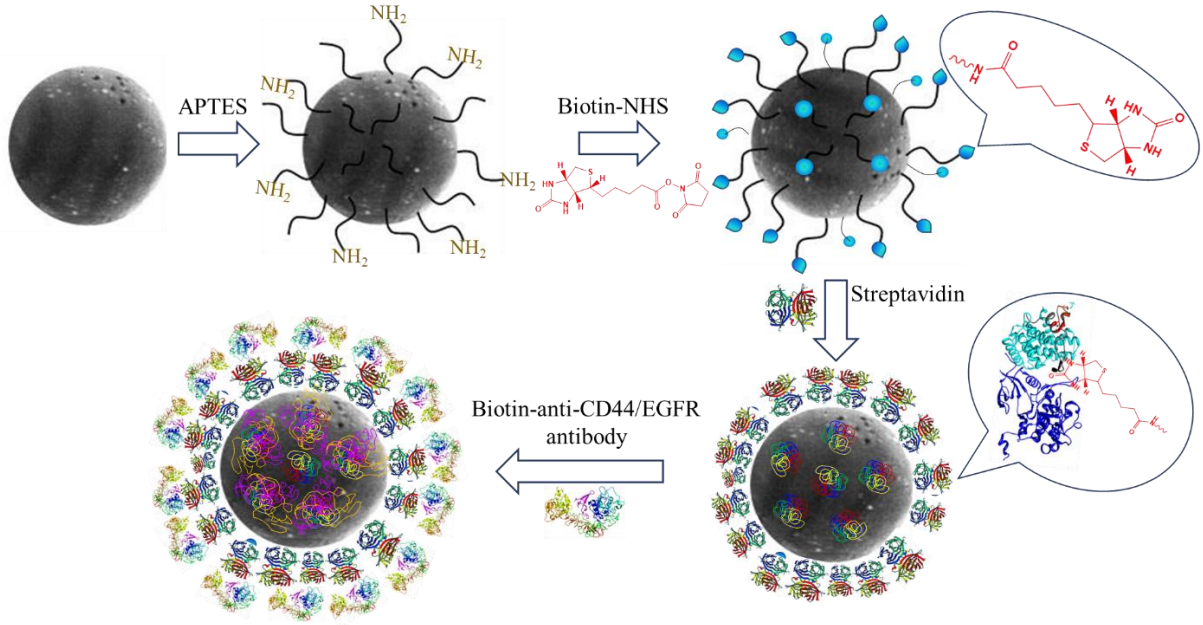

Figure 2.1. Schematic illustration of the functionalization of silica microparticles.

2.2.2 Cell culture

Human MCF7 adenocarcinoma breast cells, HeLa cervical carcinoma cells, and human lung epithelial adenocarcinoma H1650 cells were cultured in DMEM supplemented with 10% heat-inactivated FBS and 1% P/S under the humidified atmosphere (5% CO_2, 37 °C). Human NCI-H1650 lung carcinoma cells and Human T lymphoblastoid leukemia cells were cultured in RPMI 1640 medium supplemented with 10% FBS, 100 U/mL P/S, and 250 ng/mL fungizone. Cells were harvested using trypsin and collected by centrifugation for experiments.

2.2.3 Blood sample collection and PBMCs isolation

Ethical approval for the use of peripheral blood mononuclear cells (PBMCs) from healthy donors was obtained from the ethical committee (No. 2020-7) at the Graduate School of Dental Medicine, Hokkaido University. PBMCs from a healthy adult donor were collected by centrifugation over a Histopaque-1077 (Merck, USA), according to the manufacturer's protocol.[2]

2.2.4 Cell collection using silica microparticles

MCF7 or HeLa cells were mixed with PBMCs in a buffer to mimic clinical blood samples containing CTCs. The concentration of cancer cells was set at 10^4, 10^3, or 10^2 cells/ mL, with the PBMCs number kept constant at 10^5. The cells in the suspension were labeled with Syto13 nucleus staining dye (250 nM), QD655-anti-EpCAM-ab (6 nM), and QD585-anti-CD44-ab (6 nM) by co-incubation for 30 min at RT. After washing, the cells were collected by centrifugation and resuspended in PBS (Figure 2.2). The pre-labeled cells were added to the anti-CD44-ab-silica microparticles (1000 particles/mL) separately to each sample. The cells were attached to the silica particles by up-down flipping for 30 min, and the particles were allowed to settle down under the gravity. The settled particles were then gently washed and resuspended in PBS. Similarly, H1650 or HeLa and T cells were treated with the anti-EGFR-ab functionalized silica microparticles. Here, HeLa cells were labeled using QD655-anti-EpCAM-ab (6 nM), Alexa Fluor 488 anti-CD44-ab (6 nM), and Syto25 (250 nM). T cells and H1650 cells were labeled only with Syto25.

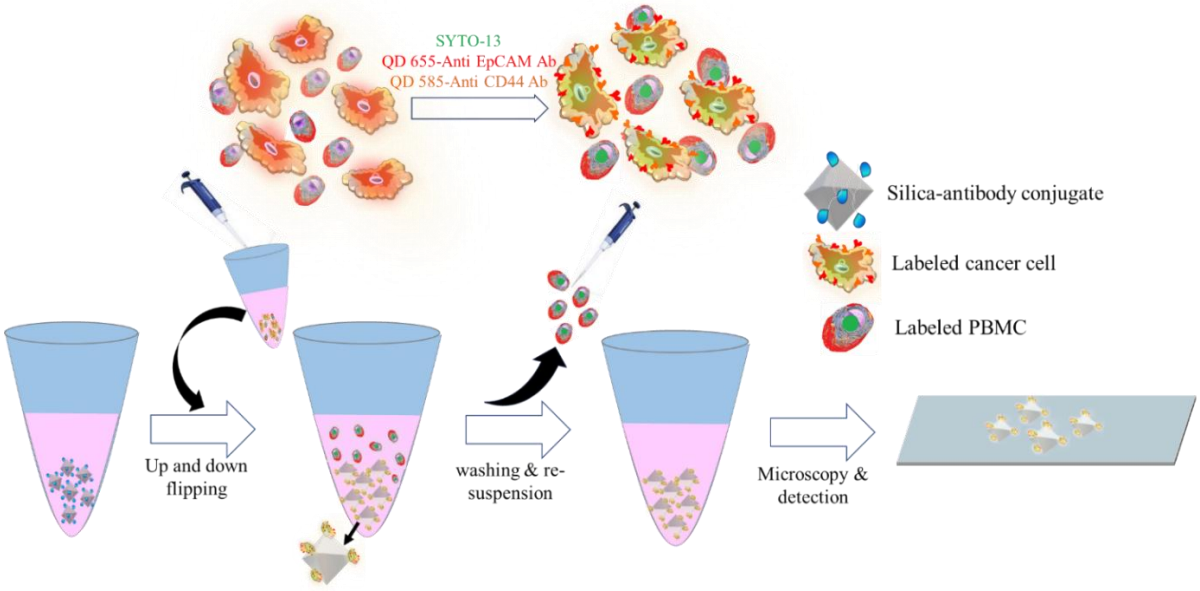

Figure 2.2. A scheme showing the procedure for isolating cancer cells in a blood sample.

2.2.5 Synthesis of a $^1O_2$ sensor

*Synthesis of sensor **4***

9,10-bis(chloromethyl)anthracene **1** (1.38 g, 5.01 mmol) was dissolved in 1,2-dichlorobenzene (20 mL) at 130 ºC followed by the addition of *N*,*N*-dioctylamine (0.96 g, 3.97 mmol). Then,

K_2CO_3 (1.36 g, 9.84 mmol) was added to the solution, and the mixture was stirred at 130 ^oC for 5 h under the argon atmosphere, during which intermediate **2** was formed. Then 7-amino-4-methylcoumarin **3** (680 mg, 3.88 mmol) was added, and the solution was stirred for 12 h. Afterward, the solution was cooled, and the precipitate was removed by filtration. The filtrate was collected, and the solvent was removed by vacuum distillation. The product was purified by silica-gel column chromatography using 10% ethyl acetate and hexane mixture, giving the sensor as a pale-yellow powder (35 %), which was characterized by ^1H NMR spectroscopy.

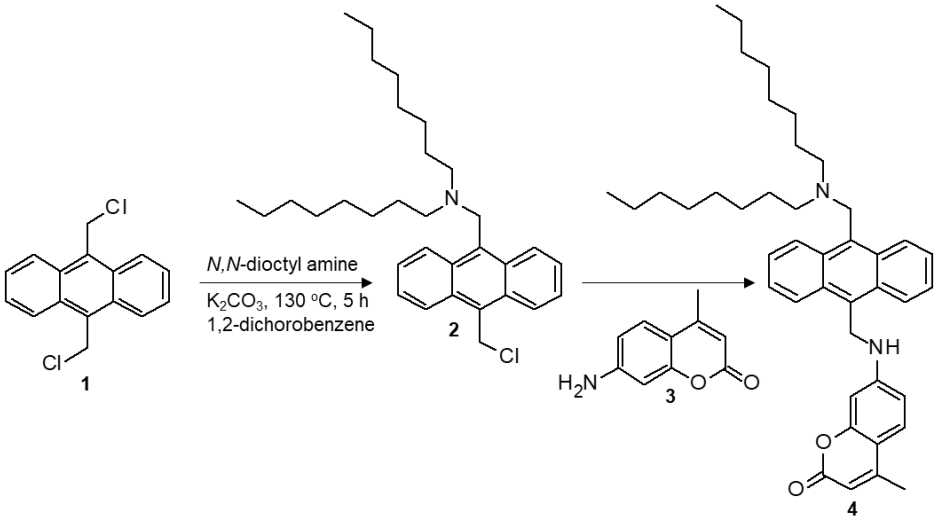

Figure 2.3. A scheme showing the synthesis of sensor **4**.

^1H NMR (400 MHz, $CDCl_3$): δ = 8.64-8.67 (d, 2 H, Ar-H), 8.21-8.23 (d, 2 H, Ar-H), 7.51-7.53 (m, 4 H, Ar-H), 7.42-7.45 (d, 1 H, Ar-H), 6.75 (s, 1 H, Ar-H), 6.60-6.62 (d, 1 H, Ar-H), 6.04 (s, 1 H, allylic), 5.21 (d, 2 H, CH_2-NH), 4.52 (s, 2 H, Ar-CH_2-N), 4.36 (t, 1 H, NH), 2.51-2.53 (t, 4 H, N-CH_2), 2.39 (s, 3 H, CH_3), 1.40-1.55 (q, 4 H, N-CH_2-C), 1.00-1.35 (m, 24 H, C-CH_2-C), 0.5-0.8 (t, 6 H, C- CH_3).

Synthesis of ***5***

9,10-bis(chloromethyl)anthracene **1** (2 g, 7.26 mmol) was dissolved in 1,2-dichlorobenzene (30 mL) at 130 ^oC followed by the addition of 7-amino-4-methylcoumarin **3** (0.87 g, 4.99 mmol). Then, K_2CO_3 (1.36 g, 9.84 mmol) was added, and the reaction was stirred at 130 ^oC for 3 h under the argon atmosphere (Figure 2.4). Afterward, an excess amount of hexane was added

to remove the solvent, and the precipitate formed was collected by filtration. The crude product was purified by repeated precipitation from toluene and acetonitrile, which provided **5** in 40 %. The product was characterized by ^{1}H and ^{13}C NMR spectroscopy.

^{1}H NMR (400 MHz, $CDCl_3$): δ = 8.41-8.43 (d, 2 H, Ar-H), 8.29-8.43 (d, 2 H, Ar-H), 7.62-7.67 (m, 4 H, Ar-H), 7.44-7.46 (d, 1 H, Ar-H), 6.76 (s, 1 H, Ar-H), 6.61-6.63 (d, 1 H, Ar-H), 6.06 (s, 1 H, allylic), 5.66 (s, 2 H, CH_2 -Cl), 5.24 (s, 2 H, CH_2-NH), 4.33 (s, 1 H, NH), 2.39 (s, 3 H, CH_3).

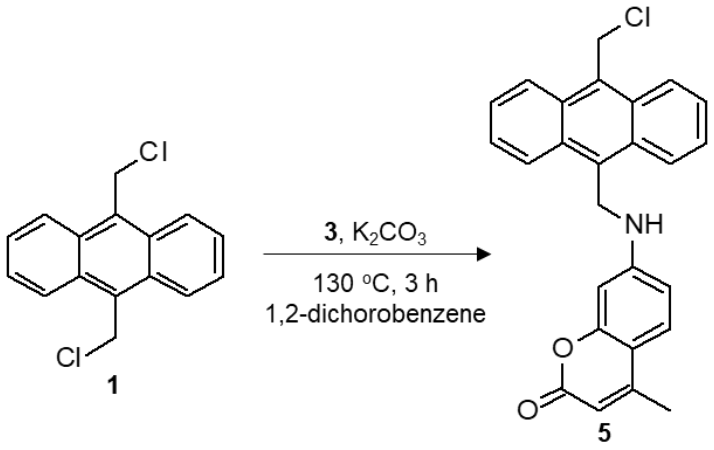

Figure 2.4. A scheme showing the synthesis of sensor **5**.

^{13}C NMR (100 MHz, $CDCl_3$): δ = 18.72, 31.03, 38.97, 40.72, 98.18, 110.02, 110.46, 111.18, 124.42, 124.76, 125.80, 126.79, 126.89, 128.32, 129.13, 129.67, 129.84, 130.38, 130.48, 151.21, 153.01, 156.20, 161.97.

2.2.6 Preparation of sensor-sensitizer nanoassemblies

Synthesis of silica-sensor/sensitizer assemblies (S-MSNP and SS-MSNP)

Mesoporous silica NPs (0.5 g; 200 nm size) were silanized by adding a 25 µL APTES solution (1 wt% APTES, 80 wt% acetone, 19 wt% water). This mixture was stirred for 30 min at 25 °C. The particles settled were thoroughly rinsed with water and acetone and dried. Then, a solution of **5** (5 mM) in 1,2-dichlorobenzene was added to the amine-functionalized silica NPs and stirred for 1 h at 100 °C in the presence of K_2CO_3 (0.5 mg, 3.61 µmol). After 1 h, the NPs were thoroughly washed with acetone and water and dried. Thus, the silica-sensor conjugate (S-

MSNP) was obtained (Figure 2.5). To prepare the silica-sensor-TCPP conjugate (SS-MSNP), a TCPP solution (500 µM) in DMSO was added to the S-MSNP and stirred for 15 min in the presence of DMT-MM (0.13 mg, 0.46 µmol) as the coupling agent at 25 °C. The silica NPs were then thoroughly washed with methanol and DMSO and dried.

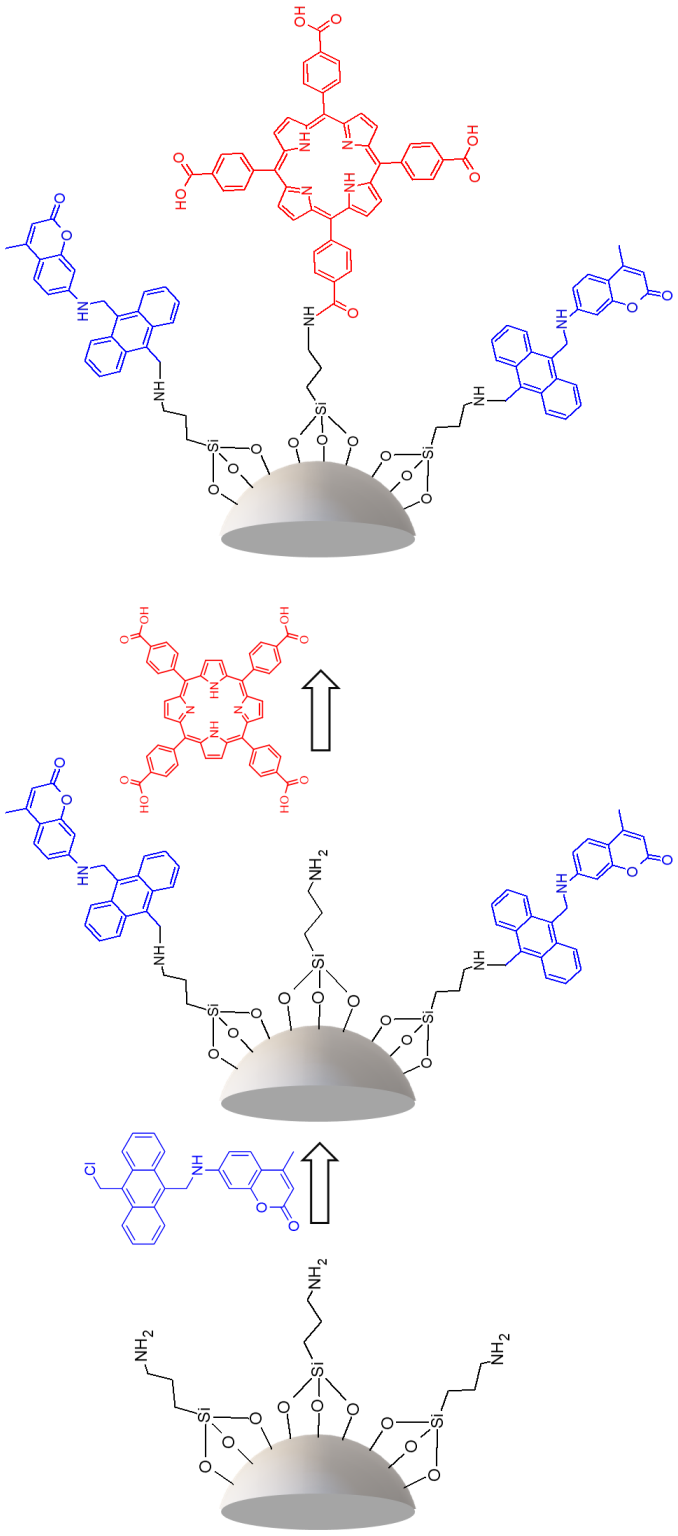

Figure 2.5. A scheme showing the synthesis of S-MSNP and SS-MSNP nanoassemblies.

Synthesis of the silica-sensor-sensitizer-RGD nanoassembly

For the conjugation of a cell-penetrating ligand, the free primary amino groups in the SS-MSNP (5 mg) were reacted with the terminal sulfo-NHS ester group of the heterobifunctional cross-linker Sulfo-SMCC (2.3 mM) in a PBS solution for 30 min at 25 ºC (Figure 2.6).[3] The particles

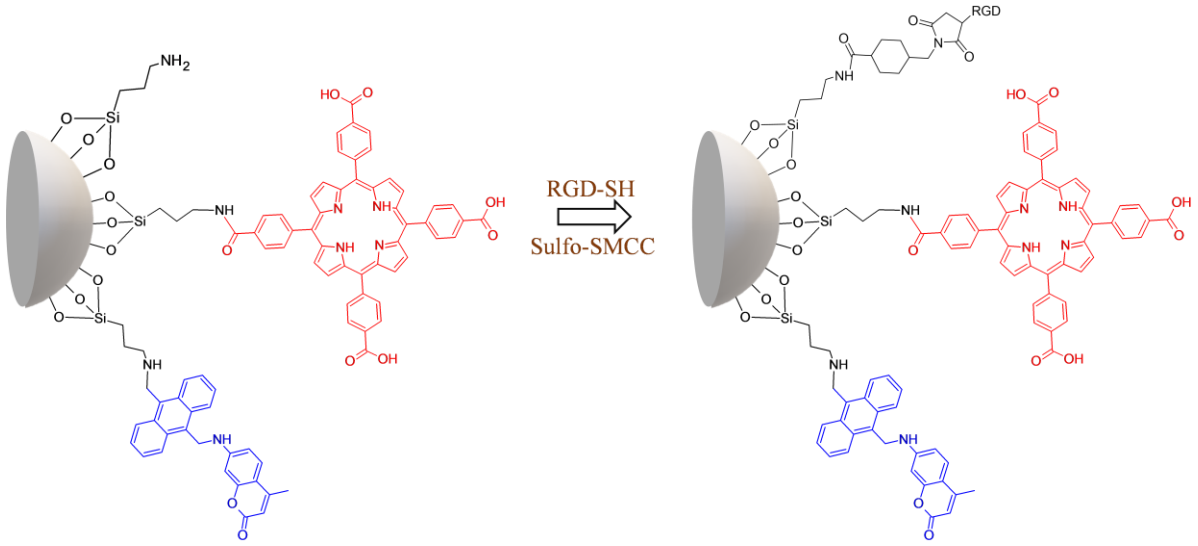

Figure 2.6. A scheme showing the synthesis of silica-sensor-sensitizer-RGD nanoassembly.

were thoroughly washed to remove the free Sulfo-SMCC and collected by centrifugation. An RGD-SH solution in PBS (1.33 mM) was added and reacted with the maleimide reactive group of the cross-linker on the SS-MSNP system for 1 h. Finally, the NPs were washed and resuspended in PBS.

Preparation of the silica-sensor-quantum dot assembly (Si-sensor-QD655)

To the S-MSNP conjugate prepared, a biotin-NHS ester solution (1 mM) in DMSO was added and stirred for 4 h at 25 ºC. Biotinylated silica particles (Figure 2.7) were obtained in this step. The particles were thoroughly washed with water and acetone. In the next step, a QD655-streptavidin solution in PBS (100 nM) was added, reacted for 30 min, washed with PBS, and resuspended in water.

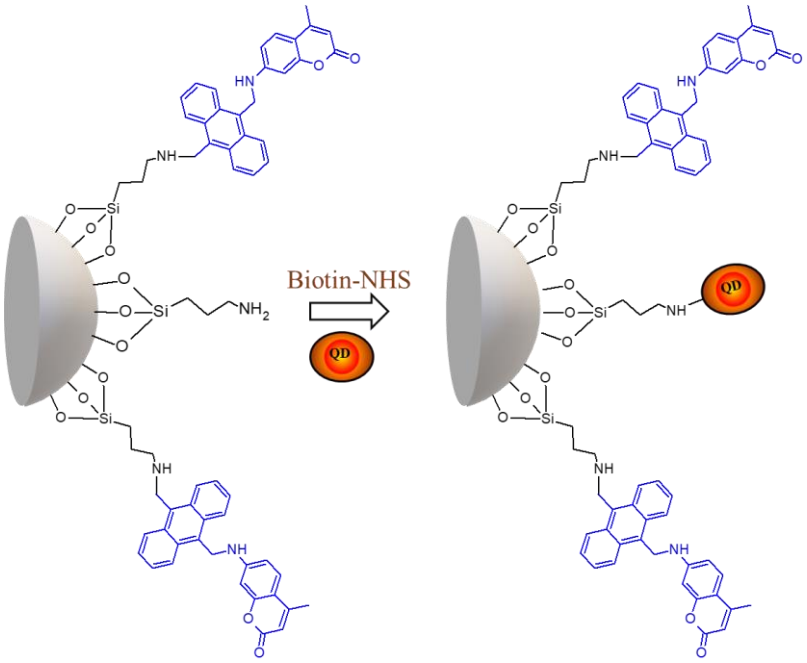

Figure 2.7. A scheme showing the synthesis of Si-sensor-QD655 nanoassembly.

2.3 Instrumentation

2.3.1 UV-vis spectrophotometry

Figure 2.8 shows the schematic diagram of a single beam UV-vis spectrophotometer. The spectrophotometer uses a light source such as a xenon lamp to excite the sample in the 190-900 nm range. The broad spectrum of white light passes a monochromator which is generally composed of an entrance slit, a dispersion device (prism/grating), and an exit slit. Finally, the nominated band of wavelengths from the monochromator passes through the sample and arrives at the detector, which is connected to a recording device. Here, the beam's attenuation due to the absorption by the molecules in a sample solution is measured. Beer-Lambert law underpins the UV-vis spectroscopy, which states that the absorbance (*A*) of a solution linearly

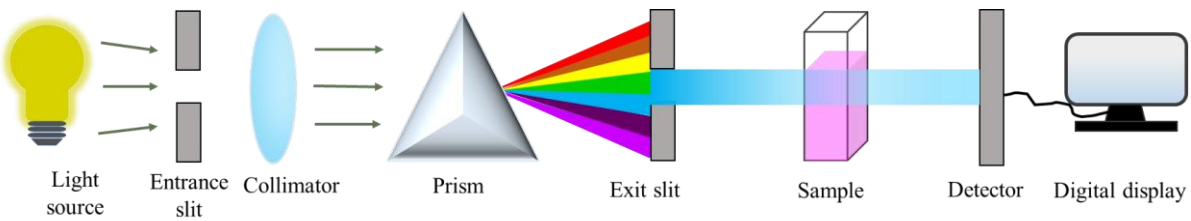

Figure 2.8. A scheme of a UV-vis spectrophotometer.

correlates with the concentration of the absorbing species (c) and the path length (l) given by $A = \varepsilon cl$, where ε is the molar absorptivity (L mol^{-1} cm^{-1}). I used Evolution 201/220 UV-Visible spectrophotometer (Thermo Scientific, USA) to quantitatively determine metal ions and to study the kinetics of the $^1O_2$ sensor.

2.3.2 Steady-state fluorescence spectroscopy

The schematic diagram of a fluorescence spectrophotometer (spectrofluorometer) is shown in Figure 2.9. The steady-state fluorescence method measures the long-term average fluorescence of the analyte in the sample upon light irradiation. A light source, excitation monochromator, sample cuvette, emission monochromator, and detector are the essential components of a spectrofluorometer. I used a Hitachi F-4500 spectrofluorometer in my studies, equipped with a 150 W Xenon lamp. The excitation wavelength from the light source reaches the sample by passing through the excitation monochromator. The monochromator allows for the transmission of a specific wavelength to excite the analyte. Upon relaxation, the molecules in the sample emit light with an emission wavelength longer than the excitation wavelength. The emitted light passes the emission monochromator placed at 90^o to the excitation wavelength. This minimizes the light scatter and screens the emission light from reaching the detector. Finally, the detector (photomultiplier tube) measures the emitted light and displays the fluorescence signature of the analyte. The fluorescence value is directly proportional to the concentration of the analyte in the sample. In my experiments, to determine the $^1O_2$ sensing ability of the sensor, I used 320 nm excitation wavelength.

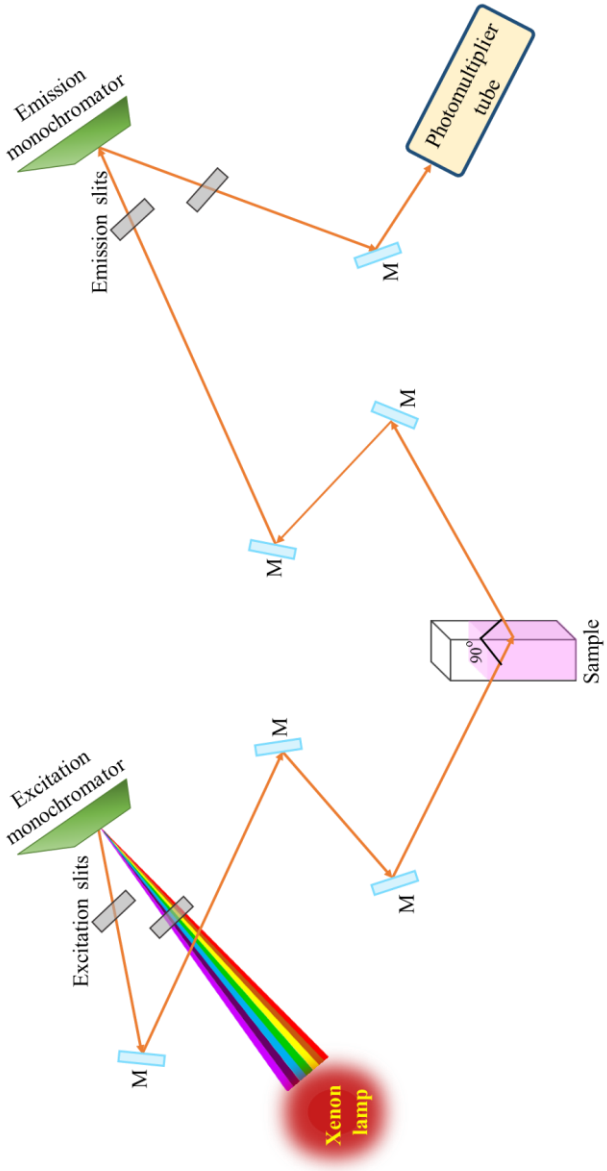

Figure 2.9. A scheme of a steady-state fluorescence spectrometer.

2.3.3 Time-resolved fluorescence spectroscopy

The schematic diagram of the optical setup for time-resolved fluorescence (TRF) spectroscopy is shown in Figure 2.10. TRF detects the intensity decays or the delayed detection of the fluorophore's emission upon excitation. Here, the excitation light pulse is shorter than the decay time. I used the TRF for the immunohistochemistry assay and to identify cells attached to the silica microparticles particularly CTCs. I measured the fluorescence lifetime of the QDs and dyes with distinctive fluorescence lifetimes. To perform the immunohistochemistry assay, MCF7 or HeLa cells were cultured up to ~70% confluence and labeled with QD655-anti-

EpCAM-ab and QD585-anti-CD44-ab conjugates. The antigen expression levels in the labeled cells were determined from the photocount maps in a 200 ns window. The excitation light was 405 nm pulses from the optical parametric amplifier (Coherent OPA 9400) pumped by the 800 nm (200 kHz, 150 fs) output from a regenerative amplifier (Coherent RegA 9000). An oscillator (76 MHz, Coherent Mira 900F) seeded the amplifier. To obtain single-photon maps, I used a polychromator (model 250IS, Chromex) and a photon-counting Streak camera assembly (C4334, Hamamatsu Photonics). The fluorescence signals from cells were collected using a 500 nm long-pass filter, and the spectrotemporal-resolved photons were counted using the Streak camera. The intensity averaged fluorescence lifetimes were calculated by fitting the PL decays to the third-exponential equation,

$$\tau_{av} = \frac{\tau_1 A_1 + \tau_2 A_2 + \tau_3 A_3}{A_1 + A_2 + A_3}$$

where A_1, A_2, and A_3 are the amplitudes, and τ_1, τ_2, and τ_3 are the PL lifetime values of the first, second, and third components of the exponential fit.

I also collected the fluorescence images of the cells using an inverted optical microscope (Olympus IX70) equipped with a 10x or 40x objective lens and a 500 nm long-pass filter. A 465 nm (200 mW) continuous wave (cw) laser (ACAN A12) was used as the excitation source, and the fluorescence images were collected using a digital camera (Olympus, Model No. XZ-2). Next, to identify CTCs attached to silica particles, the particles were dispersed on a glass coverslip, mounted on the microscope equipped with a 40x objective lens (0.60 NA), and excited with the 405 nm fs laser. The spectrotemporal resolved photons were obtained as described above, and the multicolor images of the cells attached to the particles were collected using a color CCD camera (Olympus) attached to the microscope.

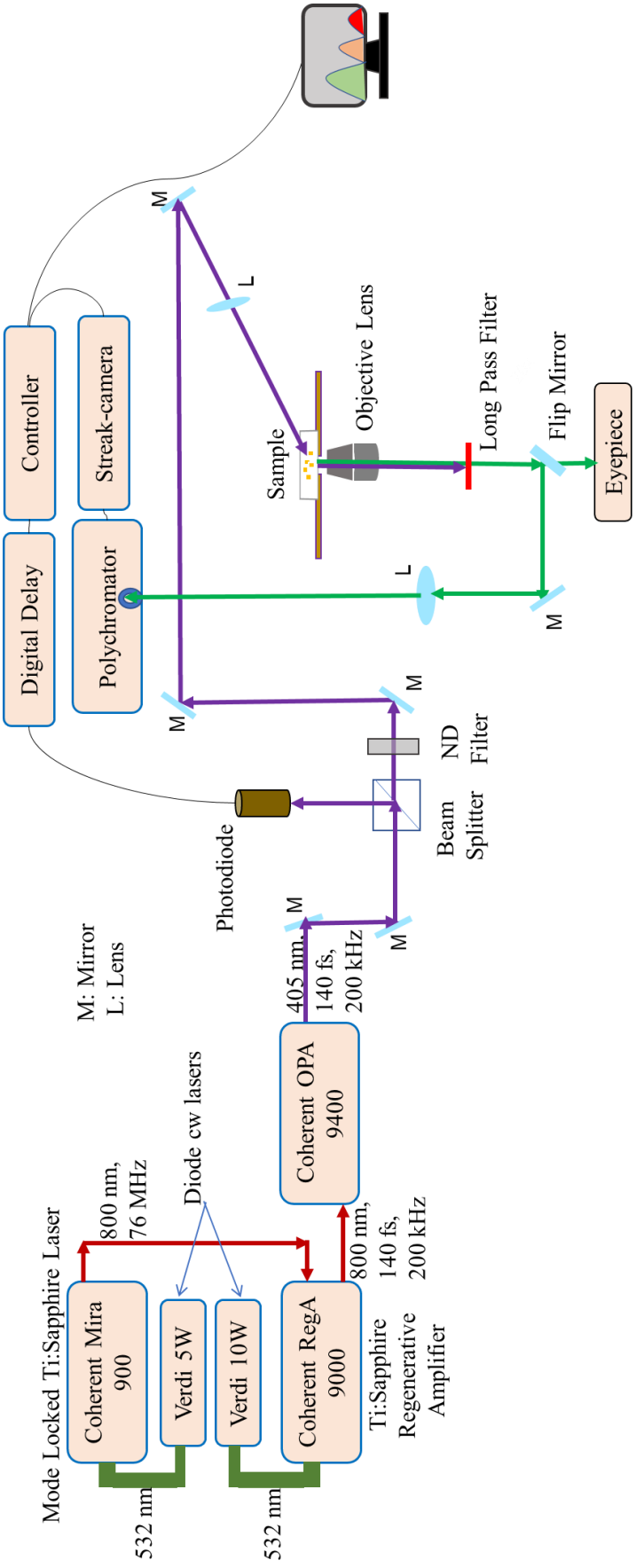

Figure 2.10. The scheme of the TRF measurement system.

2.3.4 Single-particle microspectroscopy

I used single-particle microspectroscopy to evaluate the photostability and $^1O_2$ sensing, locking, and releasing behavior of the nanoassemblies under cw laser or UV light illumination. The scheme of single-particle microspectroscopy is shown in Figure 2.11. The sample for the single-particle measurement was prepared by placing the particle suspension (1 mL) on glass coverslips (25 × 50 mm^2). The PL intensity trajectories of the S-MSNP attached to the coverslip and immersed in a TCPP solution or the SS-MSNP attached to the coverslip were recorded for 15 min on an Olympus microscope equipped with an electron-multiplying charge-coupled

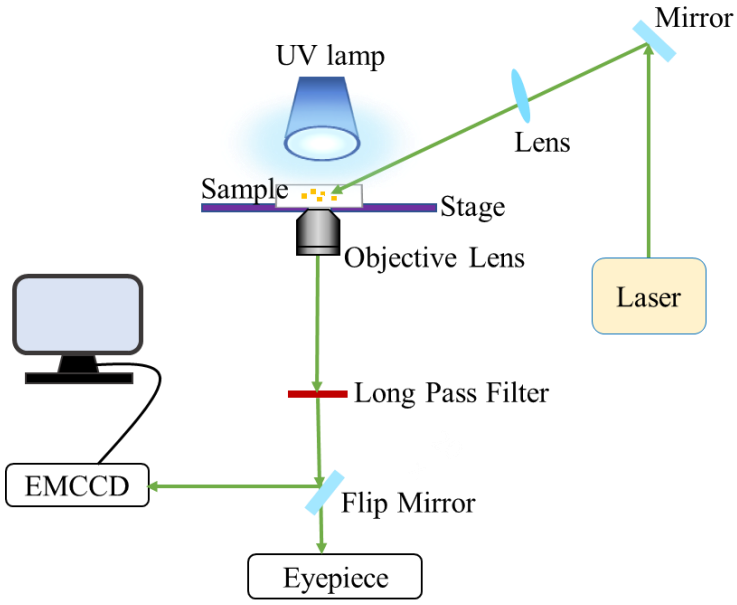

Figure 2.11. An optical setup of single-particle microspectroscopy.

device (EMCCD, iXon3, Andor Technology), a 40x objective lens (NA = 0.60), a 420-480 nm band-pass filter for coumarin, and a 600 nm long-pass filter for TCPP. TCPP in the samples was photoactivated with a 532 nm cw laser (Millenia IIs, Spectra-Physics, 2 mW cm^{-2}) at 30 s intervals followed by UV light illumination (320-390 nm) for 2 min. I recorded the PL images, videos, and intensity trajectories during this time through the coumarin's band-pass filter. Similarly, the data was recorded for Si-sensor-QD samples with 1 min photoactivation using a 532 nm cw laser and 2 min UV light illumination. The PL intensity trajectories at different power densities were collected and analyzed.

2.3.5 Confocal laser scanning microscopy

CLSM offers several advantages over conventional widefield optical microscopy. It uses a point source of light, reduces out-of-focus light that allows deep tissue imaging with high resolution, and collects optical sections from thick specimens for 3D reconstruction. The illumination and detection optics are focused on the same diffraction-limited spot. Figure 2.12

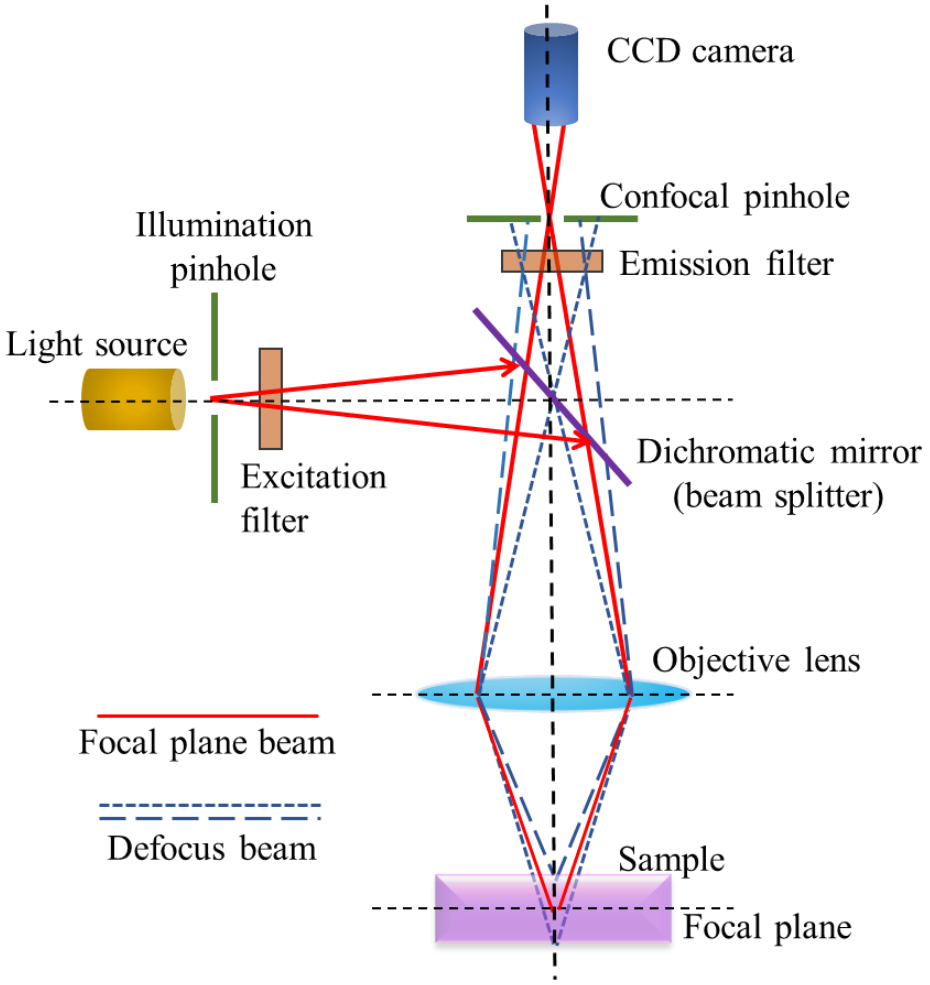

Figure 2.12. A scheme of a CLSM.

shows the basic structure of CLSM imaging. Light from the laser source passes a pinhole aperture and produces a point light source. A beam splitter reflects this excitation light through the excitation filter. The beams are focused by the objective lens into the sample and scanned across the sample in a defined focal plane perpendicular to the optical axis in the XY plane. The secondary fluorescence emitted from the illuminated area on the same focal plane passes

the beam splitter and gets focused at the detector pinhole as a confocal point through the emission filter. Since the confocal pinhole and illumination pinhole are conjugate to the objective focal plane, only the fluorescence from the focal plane passes the pinhole and reaches the detector (PMT). The emission from points above or below the focal plane of the objective is out-of-focus and will not reach the detector as it is blocked at the pinhole. It forms an extended airy disk in the aperture plane.

In my work, MCF7 cells were cultured in a culture dish with a glass bottom-up to ~60% confluency. For CLSM imaging, the cells were stained with Syto16 nucleus staining dye (5 µM) for 15 min. After PBS washing, the cells were incubated with samples of silica NPs (50 µg/mL) for 1 h in a serum-free medium. The cells were thoroughly washed with PBS, and the fluorescence emission from the cells was collected using a CLSM system (Nikon Ti2, Nikon Corporation, Japan) equipped with a water-immersion objective lens (PlanApo VC 60x/NA. 1.40). The cell samples were excited with multiple laser sources of 402, 488, and 561 nm with the respective fluorescence detection channels at 420-490 nm (sensor), 520-560 nm (Syto16), 610-730 nm (TCPP), and 630-690 nm (QD655).

2.3.6 Nuclear magnetic resonance (NMR) spectroscopy

NMR is a key analytical technique to determine the content, purity and the molecular structure of a sample. Nuclei with odd mass or odd atomic numbers have nuclear spin, and NMR is based on the atomic nuclear spins that generate magnetic fields. In the absence of an external magnetic field, the spins are arranged randomly. Still, when an external magnetic field is applied, the nuclear spin gets aligned parallel (lowest energy of the nucleus) or antiparallel (highest energy level) to the external magnetic field. This generates energy differences (ΔE) between the ground and excited state. The energy transfer or absorption takes place at a radio frequency that depends on factors such as the nucleus type (^{1}H or ^{13}C), the chemical environment of the nucleus, and the location of the nucleus in the non-uniform magnetic field. When the nuclear spins return to the initial ground state, the absorbed radiofrequency is emitted, which is proportional to the applied magnetic field. This emitted radiofrequency gives the NMR spectrum of the particular nucleus. I measured the NMR signals of my samples in a JEOL 400 MHz NMR spectrometer.

2.3.7 Scanning electron microscopy (SEM)

I used SEM to determine the surface morphology and size of silica particles before and after surface functionalization. The samples were prepared by dispersing the silica particles in ethanol and placing the sample suspension on a STEM Cu100P grid. It was then dried overnight under a vacuum, and I used a Hitachi HD-2000 microscope operated at 200 kV for SEM imaging. Finally, I estimated the size of silica particles using ImageJ software.

2.4 References

1. S. S. Shafqat, A. A. Khan, M. N. Zafar, M. H. Alhaji, K. Sanaullah, et al. Development of amino-functionalized silica nanoparticles for efficient and rapid removal of COD from pre-treated palm oil effluent, *J. Mater. Res. Technol.* **2019**, *8*, 385.
2. E. E. Thacker, M. Nakayama, B. F. Smith, R. C. Bird, Z. Muminova, T. V. Strong, L. Timares, N. Korokhov, A. M. Neill, T. D. de Gruij, J. N. Glasgow, K. Tani, D. T. Curiel, A genetically engineered adenovirus vector targeted to CD40 mediates transduction of canine dendritic cells and promotes antigen-specific immune responses *in vivo*. *Vaccine* **2009**, *27*, 7116.
3. M. G. Ciulla, R. Pugliese, F. Gelain, Boosted cross-linking and characterization of high-performing self-assembling peptides, *Nanomaterials* **2022**, *12*, 320.
4. M. B. Sigman, A. Ghezelbash, T. Hanrath, A. E. Saunders, F. Lee, B. A. Korgel, Solventless synthesis of monodisperse cu_2s nanorods, nanodisks, and nanoplatelets, *J. Am. Chem. Soc*. **2003**, *125*, 16050.
5. H. T. Uyeda, I. L. Medintz, J. K. Jaiswal, S. M. Simon, H. Mattoussi, Synthesis of compact multidentate ligands to prepare stable hydrophilic quantum dot fluorophores, *J. Am. Chem. Soc.* **2005**, *127*, 3870.
6. L. Benov, Effect of growth media on the MTT colorimetric assay in bacteria, *Plos One* **2019**, *14*, e0219713.
7. P. L. Olive, J. P. Banath, The comet assay: a method to measure DNA damage in individual cells, *Nat. Protoc.* **2006**, *1*, 23.

Chapter 3

Multimodal detection of circulating tumor cells

Abstract

Liquid biopsy involving circulating tumor cells (CTCs) for the early detection and characterization of various carcinomas is a powerful noninvasive technique. To date, most of the detection technologies are based on single modality enrichment methods except for a few reports on dual modality-based methods. The collection efficiency and detection accuracy of CTCs are continuously sought after to improve the clinical prospects of CTC-based cancer detection. This chapter reports high-efficiency CTC collection and detection by combining the self-segregating multifunctional mesoporous silica microparticles conjugated to cancer cell-specific antibodies and spectrally- and temporally resolved fluorescence photocount maps of dye or quantum dot labels in the nucleus or the cell surface. The large size of the microparticles is favorable for preventing endocytosis common to nanoscale silica or magnetic particles in CTC detection and enables the gravity separation of CTCs without applying an external force. The significance of mesenchymal biomarker targeted CTC collection and detection is demonstrated to overcome the limitations of the generally used EpCAM- or EGFR-based CTC enrichment methods. Also, the time-stamped and energy dispersed photocount histograms increase the modality of detection of triply labeled cancer cells into nine with the color, fluorescence wavelength, and lifetime resolutions. Here, the multicolor images of the collected cancer cells are associated with multiple fluorescence spectral maxima and lifetime values, increasing the CTC detection accuracy. Therefore, this multimodal detection method is expected to enable a more comprehensive collection of CTCs for advanced cancer screening and downstream assays.

3.1 Introduction

CTCs or metastatic cells have proved their excellence in liquid biopsy as a powerful tool for the early-stage detection, isolation, and molecular or genomic identification of various carcinomas.[1] These cells extravasate from the parent tumor regions to the circulatory or lymphatic systems, ultimately leading to metastasis.[2] In most cases, the presence of CTCs is marked in the early stages of cancer, particularly in the breast, lung, colorectal, and prostate cancers.[3,4] Hence, a CTC is a potential biomarker for cancer prognosis and diagnosis to ascertain cancer recurrence and chemotherapeutic efficacy.[5-7] This could ultimately improve the overall survival rate of cancer patients.[8-10] Nevertheless, the extreme rarity of CTCs, usually a few per 10^9 hematopoietic cells,[11,12] demands accurate and user-friendly strategies for their isolation and enumeration.

Over the last few years, various separation techniques have been adopted for CTC enrichment assays utilizing the physical[13-16] (size, density, nanorough surface, etc.) or biological[17-20] (cancer markers) characteristics of the cells. The immunoaffinity-based method stands at the forefront where CTCs are collected by a positive enrichment method, mostly concentrating on the EpCAM antigens as the cell surface cancer markers. Examples include the CellSearch™ technology, the "gold standard" for clinical use.[21] Also, nanomaterials such as graphene oxide chips[22], silicone nanopillars[23], or gold NPs[24] coated with the CTC-specific antibodies efficiently collect CTCs. Here, the large surface area of the nanomaterials increases the interactions of cancer biomarkers on CTCs. Also, CTC enrichment devices are fabricated using immunomagnetic strategies like immune-magnetosomes (IMSs) [25] or Strep-tag,[26,] which paved the way for cellular and molecular profiling of CTCs to overcome the limitation of using whole blood samples. In all these methods, a specific antibody-coated substrate captures the cells, targeting mainly the enormously expressed epithelial antigens on tumor cells. Conversely, considering the dissimilarities in the physical and biological properties of CTCs within a subgroup, the level of membrane proteins available for detecting CTCs varies.[27] Nevertheless, anticancer antibodies such as anti-CD44-ab[28], anti-EGFR-ab[29], anti-HER2-ab[30], and anti-Vimentin-ab[31] are widely applied to detect cancer cells. For example, the cells undergoing epithelial to mesenchymal transitions (EMT) downregulate epithelial phenotypes like EpCAM, E-cadherin, or cytokeratins, lowering the CTC detection efficiency while upregulating the mesenchymal markers during their migration phase in the bloodstream.[32,33] Besides, the low recovery rate, less purity, and insufficient sample throughput further add limitations to collecting and analyzing CTCs.[34]

Enrichment and isolation of CTCs from blood samples are essential for the detection and are often followed by various optical detection techniques. Fluorescence is one of the most promising techniques for detecting and characterizing CTCs. Fluorescence-Assisted Cell Sorting (FACS), a cytometric technique, is combined with the immunomagnetic enrichment of CTCs and is based on the fluorescence characteristics of stained cells.[35] This method yields high purity of the recovered cells, but the drawbacks include the strong flow conditions during cell sorting, which decrease the cell viability.[36] Other techniques employed for CTC detection include line-confocal microscopy,[37] which is an automated screening tool independent of the enrichment step based on microfluidics, and multi-color detection techniques, where the fluorescent-labeled cancer cells after counting are reported based on the fluorescence signals from an avalanche photodiode. The limitations include long detection time and high false-negative results that hamper further downstream analysis. Fluorescence *in situ* hybridization (FISH) is another technique where small DNA sequences attached to a fluorescent molecule act as the fluorescent probe for detecting and localizing RNA/DNA on chromosomes with a fluorescent microscope.[38] To increase the efficiency of immuno-fluorescently labeled CTCs, the fiber-optic array scanning technology (FAST) was also developed. This is based on laser printing optics, where the fluorescence emission is collected from a larger field of view after the excitation of a sample. It consists of ultra-fast and automated digital fluorescence microscopy without requiring additional enrichment.[39] Regardless of the advantages, these optical methods suffer from low throughput.

A plethora of literature reports biocompatible silica NPs for the specific binding of cancer cells.[40-43] Yoo *et al.* developed a CTC isolation method using highly dense and transparent epithelial antigen-specific silica microparticles by selective sedimentation on a disc (SSDS) to overcome the demerits of magnetic microbeads.[44] Here, the high gradient centrifugal force applied during the CTC enrichment step and endocytosis of many silica NPs decrease the cell viability.[45] In addition, the size of silica microparticles (5 μm in diameter) was almost comparable to the size of tumor cells. Yet another challenging issue is the collection of non-epithelial phenotypes and those undergoing phenotype alterations. Recent studies have shown the cancer stem cell (CSC) phenotype associated with CTC is CD44 as the biomarker.[46] CD44 is frequently overexpressed in metastasized cancer cells and is upregulated during EMT switching to its different mesenchymal isoforms.[47,48] Thus, magnetic nanomaterials functionalized with anti-CD44 are promising for CTC detection.[49] Nevertheless, most of these

detection procedures come with a single modality enrichment, except for the methods involving density gradient sedimentation,[50] and microfluidic chips.[51]

This chapter reports the collection and discrimination of MCF7, H1650, or HeLa cells from among the blood cells by using self-segregating, multifunctional immunosilica microparticles. The large size of the particles functionalized with anti-human CD44-ab or anti-EGFR-ab helps separate the cancer cells under gravity but without applying any magnetic or centrifugal force. Also, the large size of the particles is favorable for preventing endocytosis common to silica or magnetic NPs. I accomplish an error-free collection of CTCs by targeting the stem cell antigen CD44 and characterization of CTCs by triple fluorescence staining and six- to nine-fold accuracy. The triple staining is carried out using Syto13 or Syto25 nucleus staining dye, CdSe/ZnS QD (QD-655) conjugated anti-EpCAM-ab, and QD-585 conjugated anti-CD44-ab. Also, I used QD conjugated to anti-EGFR-ab with H1650 and HeLa cells. Following the triple staining of the cells, I characterized the collected MCF7, HeLa, or H1650 cells by the three-color fluorescence imaging and the triply degenerate fluorescence spectral and lifetime fingerprints of the labels.

3.2 Results and discussion

3.2.1 Immunohistochemistry assays of MCF7 cells

Firstly, MCF7 cell lines were chosen as the modal cells, the most common breast cancer cells causing malignant tumors in women.[52] I determined the levels of CD44 and EpCAM antigens in MCF7 cells by immunohistochemistry assay by labeling the cells with Syto13, QD585-anti-CD44-ab, and QD655-anti-EpCAM-ab. Details on the cell culture, QD-antibody conjugates preparation, and cell labeling are provided in section 2.2. The fluorescence microscopic image of the labeled cells obtained under a 465 nm cw laser excitation is shown in Figure 3.1a. I determined CD44 and EpCAM antigens levels on the cell membrane using a time-resolved fluorescence measurement. This was done by exciting the triply stained cells with a 405 nm pulsed laser and the simultaneous collection of photons using a Streak camera ($\lambda_{em} > 500$ nm). I characterized the cells by the multicolor fluorescence image and the single-photon histogram (Figure 3.1d). The histogram was further deconvoluted into a fluorescence spectrum (Figure 3.1b) with three spectral maxima and three decay curves (Figure 3.1c) having distinct fluorescence lifetime values. The calculated fluorescence lifetimes were 4 ns for Syto13, 11 ns

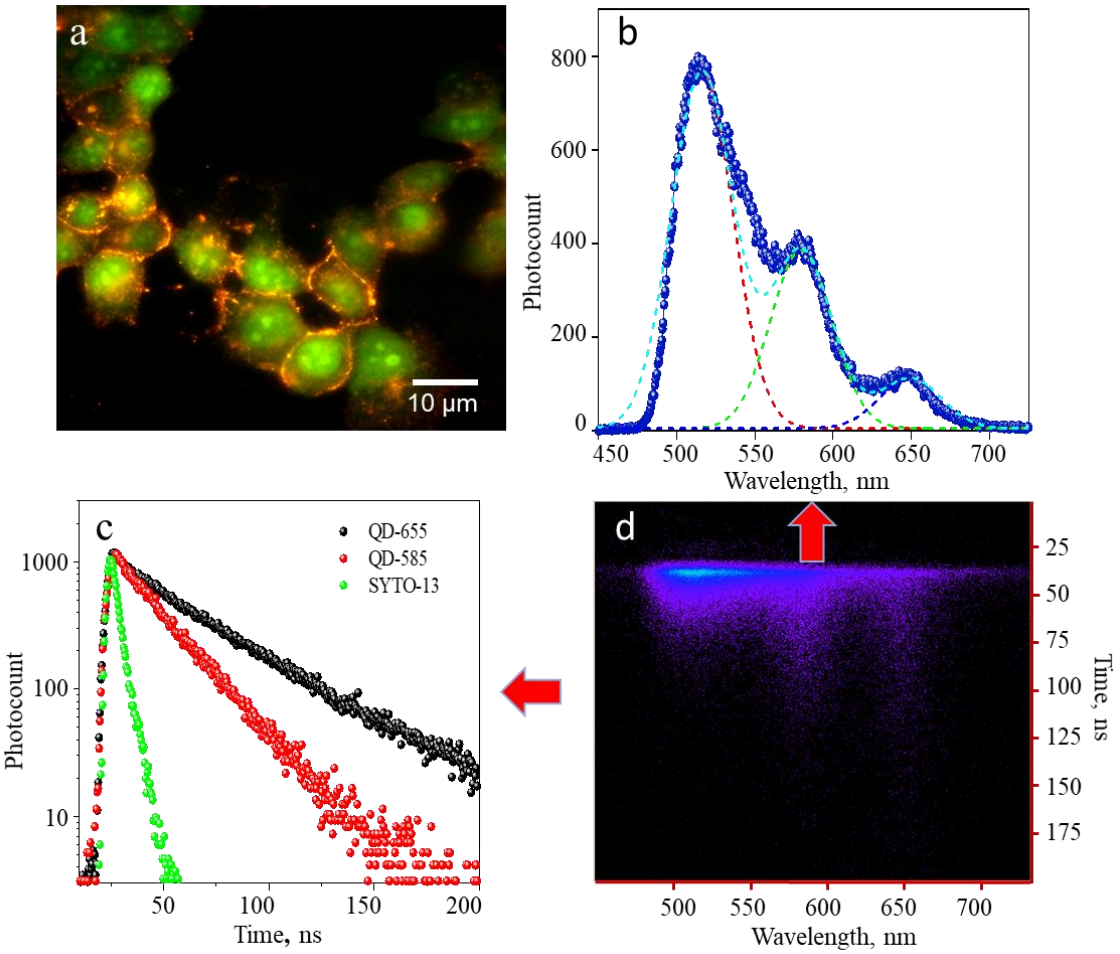

Figure 3.1. Characterization of triply stained MCF7 cells: (a) A fluorescence image of MCF7 cells identified with the emission from Syto13, QD585-anti-CD44-ab, and QD655-anti-EpCAM-ab. (d) A single-photon histogram of the cells showing the time and energy dispersed photon counts. (b) The fluorescence spectrum obtained from the integration of the photons in 'd'. The broken lines represent the Lorentzian fits based on the three fluorescence intensity maxima (ca 515, 585, and 655 nm). (c) The fluorescence decay curves of the three fluorophores.

for QD585, and 19 ns for QD655. Since the lifetime values are different for different labels, these results become the fingerprint evidence to distinguish CTCs from blood cells based on the differential expression of CD44 and EpCAM antigens. The integrated photocount maxima ca 515 (Syto 13), 585 (QD585-anti-CD44-ab), and 655 (QD655-anti-EpCAM-ab) nm resolved by the Lorentzian fittings, and the triply degenerate fluorescence decay profile resolve the ratios of EpCAM and CD44 antigens in the cells. Here, by considering the comparable

photoluminescence quantum efficiencies of QD585 and QD655 (ca 80%), I found that the expression level of CD44 is greater than EpCAM in MCF7 cells by a factor of 4. This result helped not only to characterize the cells but also to correlate the literature reports about the expression levels of CD44 and EpCAM antigens in the mesenchymal phenotype of MCF7 cells associated with breast cancer during the induction of EMT.[32,33] The cancer cells that undergo EMT acquire more stem-like properties and show an increase in the expression of stem cell markers like CD44 in its standard form or variant spliced isoforms.[47] Thus, the expression level of EpCAM and CD44 surface markers in MCF7 cells was confirmed micro-spectroscopically. These results suggested that the capturing efficiency of MCF7 cells in a blood sample can be improved by targeting CD44 than EpCAM. Overall, this work showed a 9-fold accuracy for cancer cell detection by combining the three-color imaging with the spectro-temporal resolution.

3.2.2 Capturing and identification of MCF7 cells using silica microparticles

A scheme for preparing the functionalized silica particles and the steps involved in collecting cancer cells for microspectroscopic detection are provided in Chapter 2 (Figures 2.1 and 2.2). I prepared the multifunctional silica microparticles by silanizing silica particles with APTES followed by biotinylation with biotin-NHS ester and conjugation with streptavidin. Figure 3.2 shows the SEM images of silica particles after silanization.

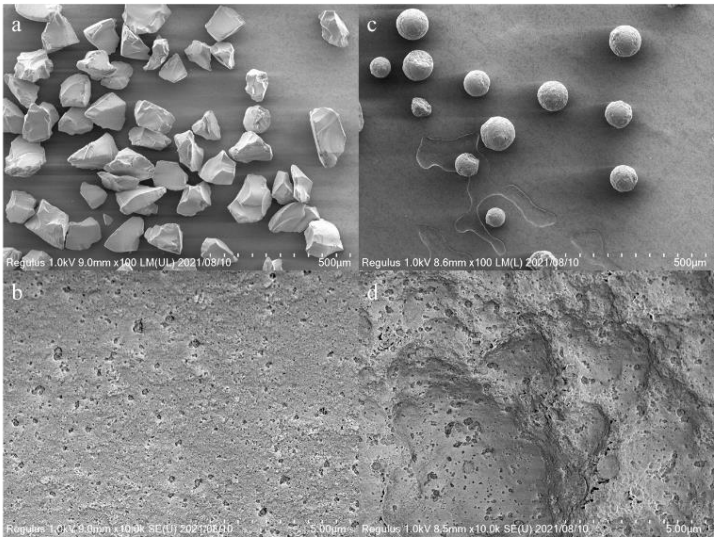

Figure 3.2. SEM images showing the two types of mesoporous silica particles with (a,b) irregular and (c,d) spherical shapes and morphologies.

Parallelly, anti-CD44-ab or anti-EGFR-ab was also biotinylated and stabilized in PBS. Biotin-anti-CD44-ab was attached to the streptavidin functionalized silica particles, purified by multiple washing, and separated under gravity. The detailed procedure of the steps involved is provided in Chapter 2. The large size (75 ~ 150 µm) and high specific gravity (~1.6 g/ml) of the mesoporous silica particles allow the gravity separation of cells compared to centrifugation commonly employed for CTC collection using immunomagnetic beads or silica NPs.[44] In addition, the possibility of nanosized particles engulfing (endocytosis) by the bound cells (5 ~20 µm) can be eliminated. In parallel to the subsequent conjugation of anti-CD44-ab to the functionalized silica microparticles, the blood sample was treated with a QD585-anti-CD44-ab solution (6 nM) in the labeling step, such that the antibody labels a portion of CD44 antigens on MCF7 cells and a portion is left for binding to the immuno-silica particles. I confirmed this binding by performing a control experiment by labeling the cells with a 6 nM or 30 nM of QD585-anti-CD44-ab solution. The fluorescence spectra obtained are shown in Figure 3.3. The integrated photocounts from different parts of the sample using a Streak camera confirmed more than 60% of the CD44 antigens on MCF7 cells are available for conjugation with the functionalized silica particles. This is one of the critical factors for collecting and sensitively detecting the cells following the immunoprecipitation.

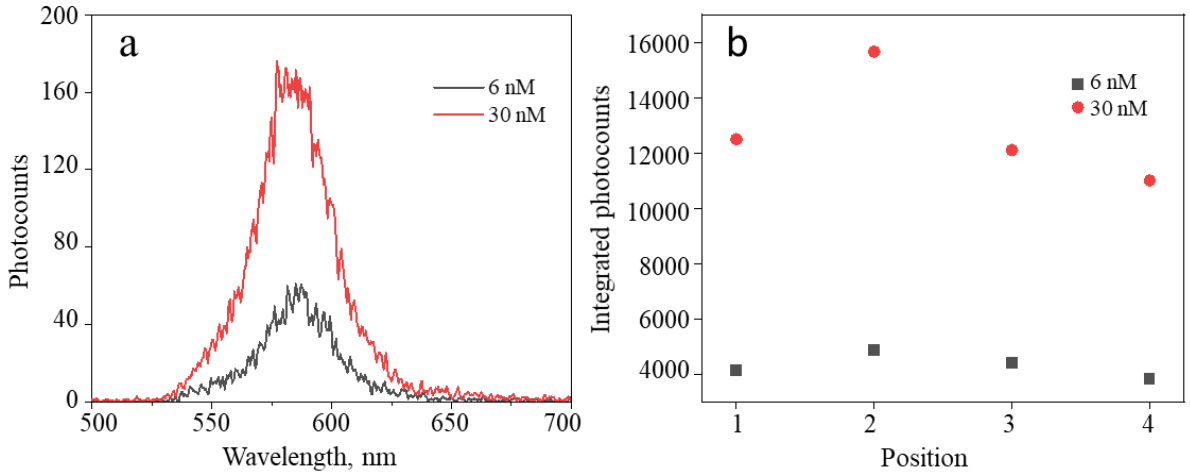

Figure 3.3. (a) The fluorescence spectrum for equal numbers of cells labeled with QD585-anti-CD44-ab at two concentrations. (b) Integrated photocounts for equal numbers of cells labeled with QD585-anti-CD44-ab at two concentrations and collected from different parts of a cell sample.

For the spectroscopic detection of cells, PBMCs and the MCF7 cells were pre-labeled with Syto13 dye, QD585-anti-CD44-ab, and QD655-anti-EpCAM-ab. The labeled cells, dispersed in PBS, were added to the functionalized silica particles, and the CTCs were isolated by gentle up-down flipping of the tube. The particles were settled under gravity, which can be denoted as a "natural gravity-mediated enrichment" method (Chapter 2). This helped avoid applying any external force such as ultracentrifugation to collect the CTC-silica complex. Thus, the difference in the density between the CTC-silica complex (~1.6 g/ml) and the PBMCs (< 1.07 g/ml) helped remove the blood cells easily and enrich CTCs. The isolated CTCs conjugated to the silica particles were characterized microscopically and spectroscopically. Figure 3.4a

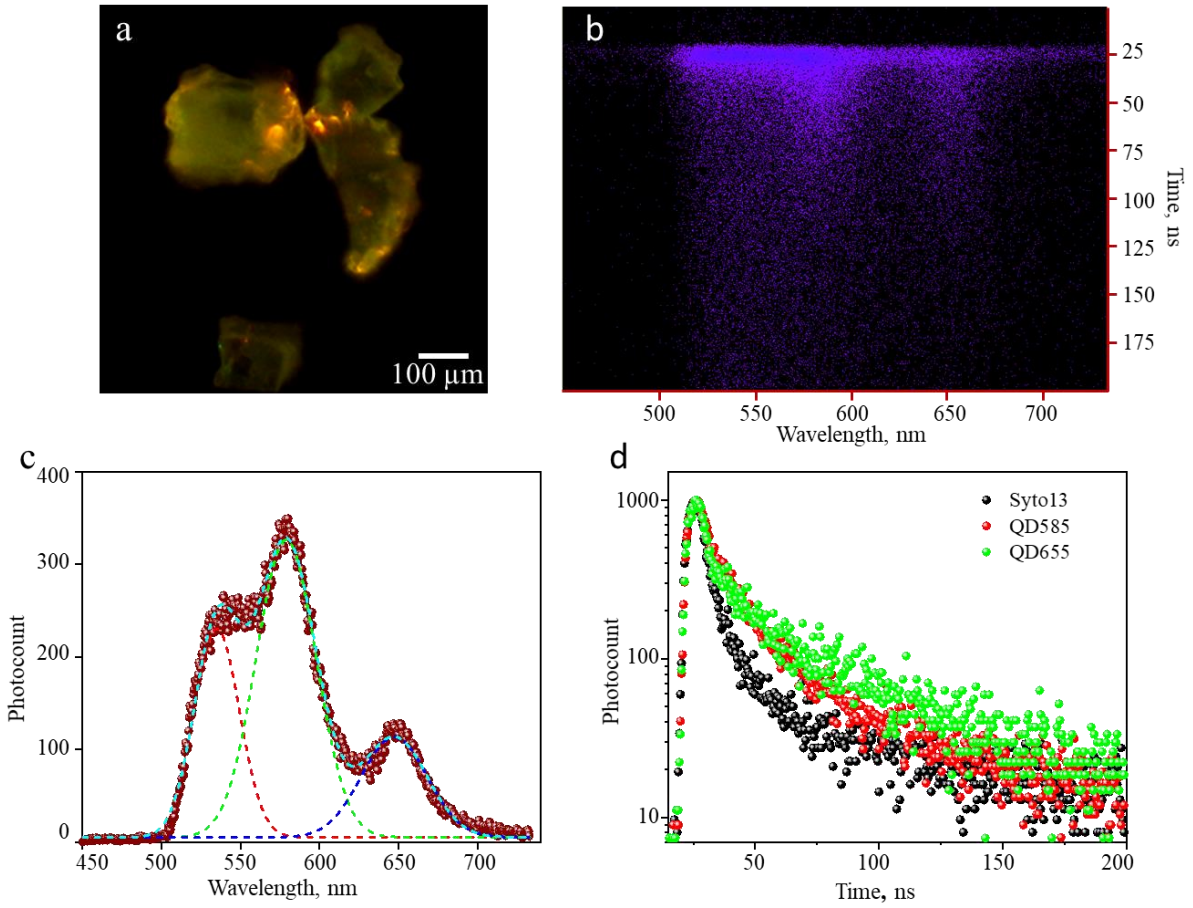

Figure 3.4. (a) A fluorescence image showing MCF7 cells attached to the immuno-silica particles with anti-CD44-ab. (b) A single-photon histogram of the cells showing the time and energy dispersed photon counts. (c) The fluorescence spectrum obtained from the integrated photons in 'b'. The broken lines represent the Lorentzian fits for the fluorescence intensity maxima ca 515, 585, and 655 nm. (d) The fluorescence decay curves of the three fluorophores deconvoluted from 'b'.

shows the MCF7 cells attached on anti-CD44-ab functionalized silica microparticles, and the single-photon histogram is shown in Figure 3.4b. The corresponding multi-color emission spectrum deconvoluted from the histogram resolved by the Lorentzian fittings (Figure 3.4c) confirms CTCs attached to the silica particles. Here, the characteristic fluorescence spectral maxima ca 515, 585, and 655 nm disclose the nucleus staining and the presence of CD44 and EpCAM. Further, the time-resolved triply degenerate decay curves of the individual labels reconstructed from the photocount map are shown in Figure 3.4d. The calculated fluorescence lifetime values are 10 ns for Syto13, 11 ns for QD585, and 15 ns for QD655. The isolation of 1-100 MCF7 cells was achieved in samples with 10^2 to 10^4 cells/mL, keeping the PBMC count constant at 10^5. Interestingly, by using anti-CD44-ab to collect MCF7 cells, we avoided nonspecific absorption of PBMC to the silica particles. Therefore, these results highlight the selectivity and sensitivity of this method toward the detection of MCF7 cells among the blood cells.

3.2.3 Immunohistochemistry assay and identification of HeLa cells

To confirm the EMT antigen-specific collection and detection of CTCs using the microspectroscopic technique, I chose a different cell line (HeLa) and followed the above protocol for MCF7 cells. HeLa cells were labeled with Syto13 dye, QD585-anti-CD44-ab, and QD655-anti-EpCAM-ab. The fluorescence microscopic images of the cells were obtained under a 465 nm cw laser excitation followed by immunohistochemistry assay. The time- and spectrally-resolved fluorescence photocounts were simultaneously collected using a Streak camera. Figure 3.5a shows the fluorescence image of HeLa cells, and the corresponding single-photon histogram is shown in Figure 3.5b. As seen in the photocount map, the QD655-anti-EpCAM-ab conjugate is not detected on HeLa cells, showing the EpCAM antigen-negative characteristic of the cell line, which is consistent with the literature.[53]

Next, the experiment was performed by attaching the labeled cells to silica particles functionalized with anti-CD44-ab, following the previous method for MCF7 cells. Figure 3.6a shows the fluorescence image of HeLa cells on immuno-silica particles, identified from the colocalized red-green (yellow) image, the bimodal photocount map (Figure 3.6b), and the doubly resolved emission spectrum obtained from the histogram (Figure 3.6c). Furthermore, the two decay profiles constructed from the Streak camera image and the corresponding fluorescence lifetimes of the individual labels (Figure 3.6d) confirm HeLa cells.

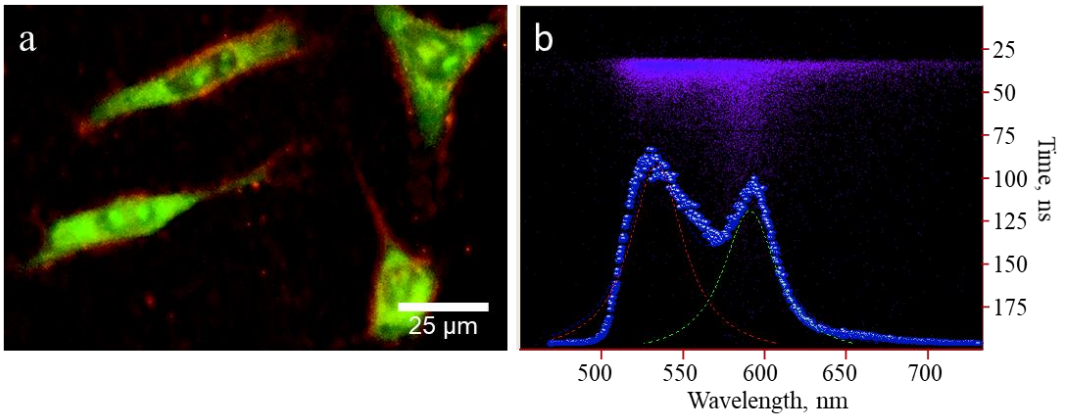

Figure 3.5. (a) A fluorescence image of HeLa cells identified with the emission from Syto13 and QD585-anti-CD44-ab. (b) The single-photon histogram showing the time- and energy-dispersed photocounts.

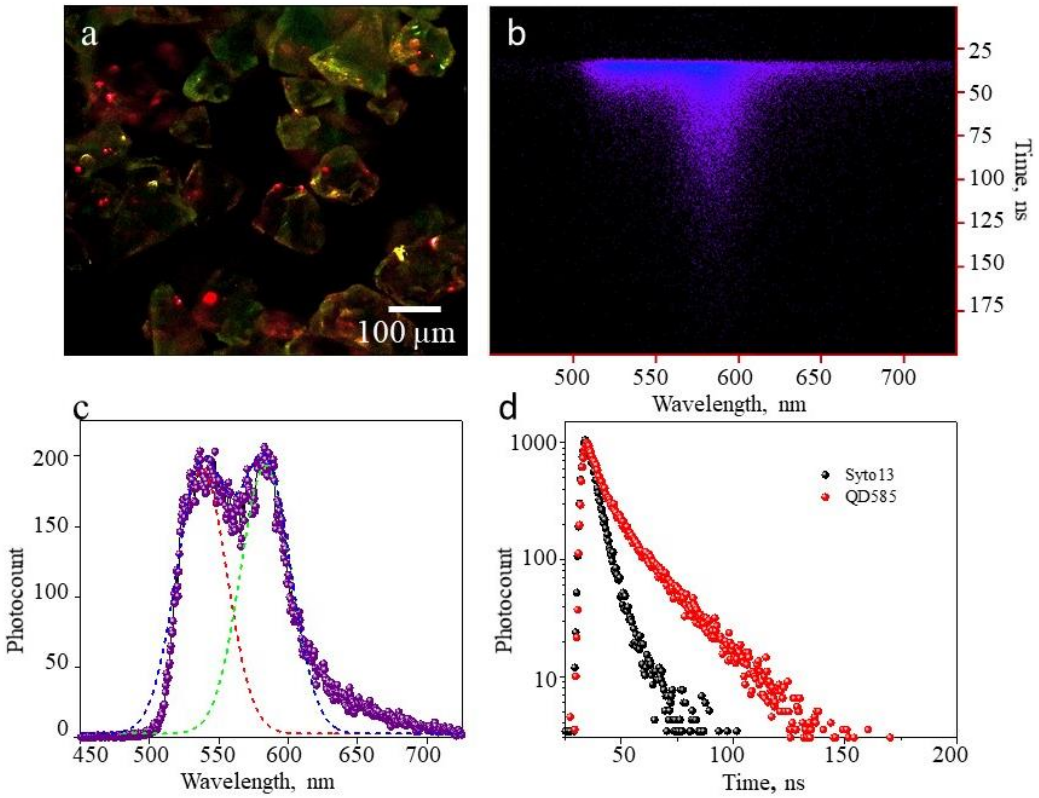

Figure 3.6. (a) A fluorescence image of HeLa cells attached to immunosilica particles with anti-CD44-ab. (b) A single-photon histogram showing the time- and energy-dispersed photocounts for HeLa cells attached to the silica particles. (c) The fluorescence spectrum deconvoluted from the photocount map in 'b'. (d) The fluorescence decay curves of the two fluorophores deconvoluted from 'b'. The calculated average fluorescence lifetime values are 5 ns for Syto13 and 8 ns for QD585.

Despite the deficiency of EpCAM antigen on HeLa cells, when examined at the single-cell level, the QD655-anti-EpCAM-ab conjugate was detected in a few HeLa cells at a low level (Figure 3.7). Hence, this multi-modal detection method based on the spectrally- and time-resolved fluorescence, displayed high CTC selectivity.

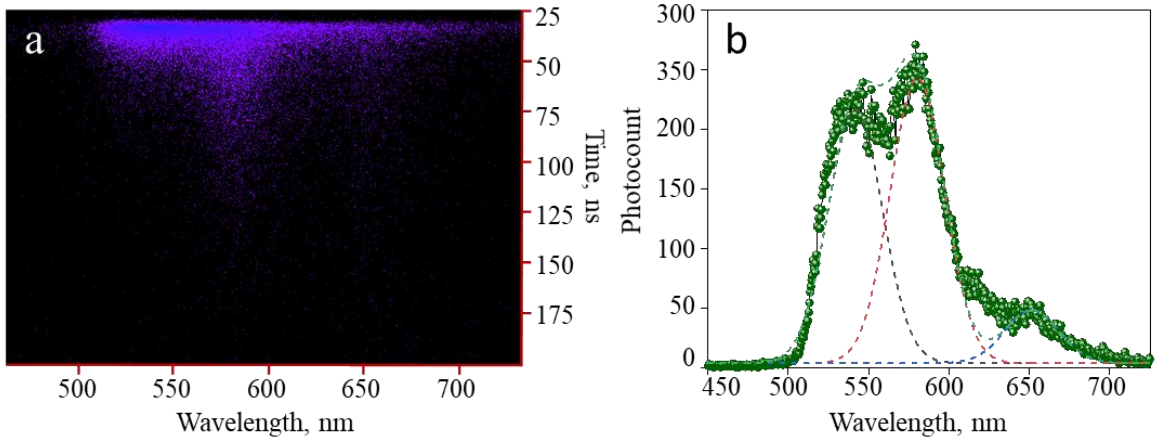

Figure 3.7. (a) A single-photon histogram showing the time- and energy-dispersed photon counts of HeLa cells, slightly expressing EpCAM antigen on their surface. (b) The fluorescence spectrum obtained from the integration of the photons in 'a'.

3.2.4 Advantages of CD44 antigen-based CTC capturing

To increase the modality of CTC detection, I modified the silica particles with anti-EGFR-ab. Anti-EGFR-ab was selected mainly because EGFR, a 170 kDa transmembrane glycoprotein, is overexpressed in various cancers and is widely used as an alternative biomarker for non-EpCAM-based approaches for CTCs enrichment and isolation.[54,55] The anti-EGFR-ab functionalized silica microparticles were then utilized for the enrichment of cells labeled using Syto25 dye, AlexaFluor488-anti-CD44-ab, and QD655-anti-EpCAM-ab. Figure 3.8a shows HeLa cells on anti-EGFR-ab functionalized silica particles. Here, I observed the binding of many PBMCs (green fluorescence) on the silica particles when compared to the immuno-silica particles with anti-CD44-ab as shown in the single-photon histogram (Figure 3.8b). I failed to discriminate the blood cells from the cancer cells based on the fluorescence maximum ca. 515 nm (Figure 3.8c) because the emission maxima ca. 515 nm was from the nucleus staining Syto25 dye, and the characteristic fluorescence decay profile matched with Syto13. Also, the lifetime value or decay profile (Figure 3.8d) cannot identify HeLa cells. This is not surprising since PBMCs also express EGFR approximately at 40k ~ 100k receptors per cell.[54]

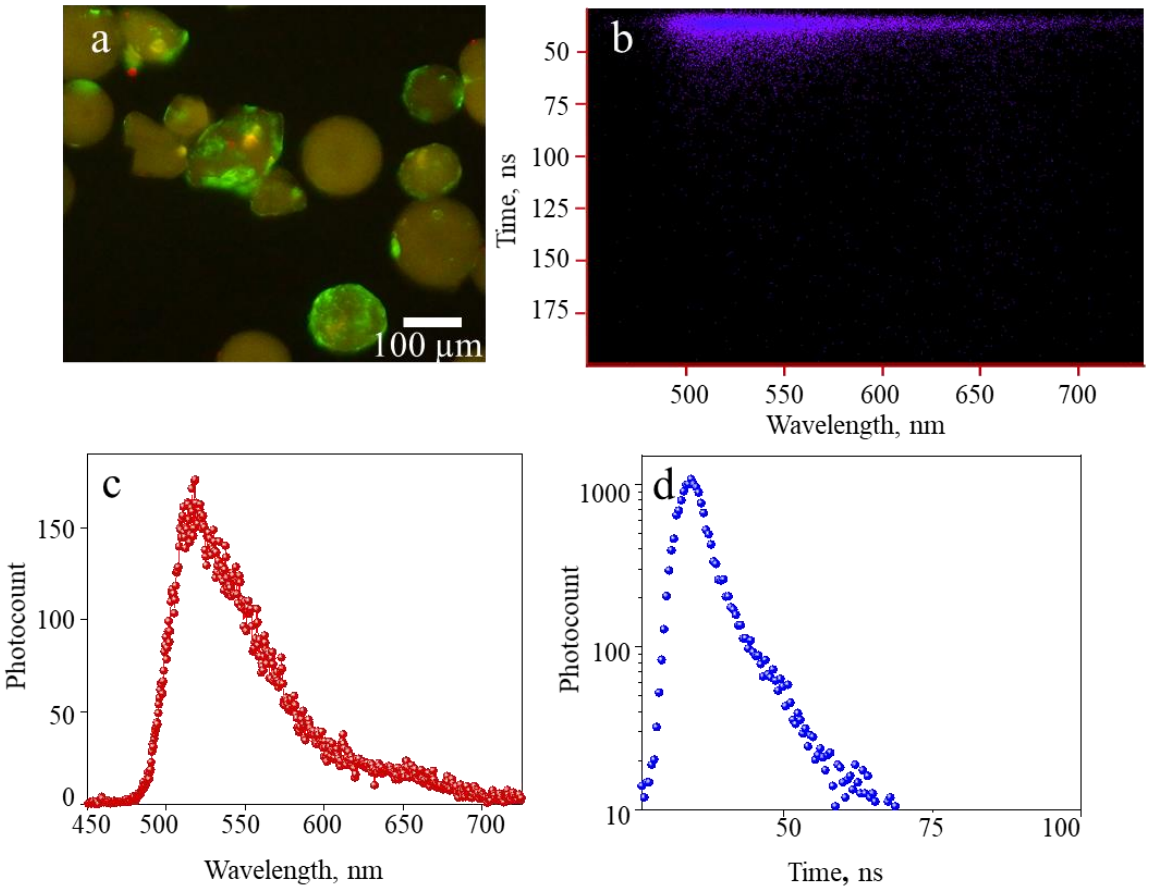

Figure 3.8. (a) A fluorescence image of HeLa cells attached on the silica particles with anti-EGFR-ab. The cells were labeled with Syto25 and AlexaFluor 488-anti-CD44-ab conjugate. (b) A single-photon histogram showing the time- and energy-dispersed photon counts of PBMCs attached to silica particles, confirming the binding of the blood cells. (c) The fluorescence spectrum of Syto25 dye obtained from the integration of the photons in 'b'. (d) Fluorescence decay curve of Syto25 in PBMCs. The calculated average fluorescence lifetime is 3 ns.

Further, to verify the capture and detection of cancer cells using immuno-silica particles, I chose H1650 cells owing to the upregulation of EGFR in lung cancer cells.[56] Here, I labeled H1650 and T cells only with the Syto25 dye and attached them to the anti-EGFR-ab conjugated silica particles. Figure 3.9a-d shows H1650 cells on silica particles, obtained with different numbers of H1650 and T cells. Figure 3.9d, corresponding to 10^6 T cells/mL but without H1650 cells, shows many T cells bound to the anti-EGFR-ab functionalized silica particles.

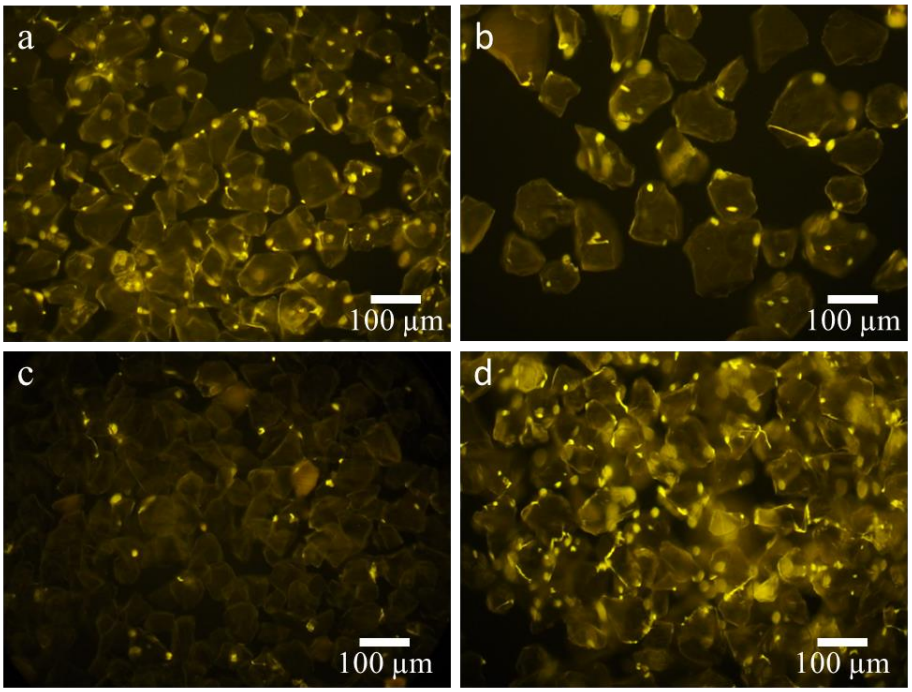

Figure 3.9. Fluorescence images of silica particles with anti-EGFR-ab in 1 mL blood samples with (a) 10^4 H1650 and 10^6 T cells, (b) 10^3 H1650 and 10^6 T cells, (c) 10^4 H1650 but without any T cells, and (d) 10^6 T cells but without any H1650 cells.

Despite the presence of EGFR in many cancer cells, such as H1650 and HeLa cells, the CTC enrichment method relying on EGFR proved to be less efficient than CD44-based capturing of the cells due to the interference of blood cells. Therefore, I combined the stem cell biomarkers such as CD44 with multicolor imaging, multimodal spectra, and multiple PL decays for error-free CTC detection, minimizing false-negative results. This work demonstrates the technical benefits of choosing mesenchymal biomarkers, the spectral and time-resolved modalities, and self-segregating immunosilica microparticles for CTC detection.

3.3 Conclusion

In this chapter, I demonstrated an effective microspectroscopic detection technique for the collection and error-free detection of CTCs with an accuracy of 1-10 among 100 cancer cells in 1 mL blood samples. By pre-labeling cells with the desired antibodies without saturating the surface antigens, cancer cells were collected by the multifunctional and self-segregating

immunosilica particles. The large-size, highly dense, and antibody-functionalization of silica particles were utilized to prevent the endocytosis and enable capturing of cancer cells without applying an external force. Besides, as an alternative to EpCAM antigen targeted CTC capturing, I focused on CD44 transmembrane stem cell marker, abundant in metastasized cells, resulting in high collection efficiency of cancer cells among the blood cells. Further, with the help of bright and narrowband emissive QDs labels, the isolated cancer cells were characterized by triple-fluorescence imaging and a six- to nine-fold fluorescence detection technique based on the spectral and lifetime resolutions, which are the fingerprints of the labeled cells. Hence, the multi-modality of this method is exemplified based on multicolor imaging and spectro-temporally resolved fluorescence detection technique, which can be developed for advanced cancer screening as well as post-surgical/ therapeutic clinical follow-up.

3.4 References

1. D. E Campton, A. B. Ramirez, J. J. Nordberg, N. Drovetto, A. C. Clein et al. High-recovery visual identification and single-cell retrieval of circulating tumor cells for genomic analysis using a dual-technology platform integrated with automated immunofluorescence staining, *BMC Cancer* **2015**, *15*, 360.

2. T. R. Ashworth, A case of cancer in which cells similar to those in the tumors were seen in the blood after death. *Med. J. Aust.* **1869**, *14*, 146.

3. S. K. Arya, B. Lim, A. R. A. Rahman, Enrichment, detection and clinical significance of circulating tumor cells. *Lab Chip* **2013**, *13*, 1995.

4. A. Ring, I. E. Smith, M. Dowsett, Circulating tumour cells in breast cancer. *Lancet Oncol*. **2004**, *5*, 79.

5. V. Muller, S. Riethdorf, B. Rack, W. Janni, P. A. Fasching et al. Prognostic impact of circulating tumor cells assessed with the CellSearch System™ and AdnaTest Breast™ in metastatic breast cancer patients: the DETECT study, *Breast Cancer Res.* **2012**,*14*, R118.

6. H. Iinuma, T. Watanabe, K. Mimori, M. Adachi, N. Hayashi et al. Clinical significance of circulating tumor cells, including cancer stem-like cells, in peripheral blood for recurrence and prognosis in patients with dukes' stage B and C colorectal cancer. *J. Clin. Oncol.* **2011**, *29*, 1547.

7. A. de Albuquerque, I. Kubisch, G. Breier, G. Stamminger, N. Fersis et al. Multimarker gene analysis of circulating tumor cells in pancreatic cancer patients: a feasibility study, *Oncology* **2012**, *82*, 3.

8. M. Cristofanilli, D. F. Hayes, G. T. Budd, M. J. Ellis, A. Stopeck, J. M. Reuben et al. Circulating tumor cells: a novel prognostic factor for newly diagnosed metastatic breast cancer, *J. Clin. Oncol*. **2005**, *23*, 1420.

9. H. Yagata, S. Nakamura, M. Toi, H. Bando, S. Ohno et al. Evaluation of circulating tumor cells in patients with breast cancer: multi-institutional clinical trial in Japan, *Int. J. Clin. Oncol*. **2008**, *13*, 252.

10. T. Kurihara, T. Itoi, A. Sofuni, F. Itokawa, T. Tsuchiya et al. Detection of circulating tumor cells in patients with pancreatic cancer: a preliminary result. *J. Hepatobiliary. Pancreat. Surg*. **2008**, *15*, 189.

11. M. C. Miller, G. V. Doyle, L. W. M. M. Terstappen, Significance of circulating tumor cells detected by the Cellsearch system in patients with metastatic breast colorectal and prostate cancer, *J. Oncol*. **2010**, *2010*, 617421.

12. M. Cristofanilli, G. T. Budd, M. J. Ellis, A. Stopeck, J. Matera et al. Circulating tumor cells, disease progression, and survival in metastatic breast cancer. *New Engl. J. Med.* **2004**, *351*, 781.

13. Y. T. Yeh, R. A. Harouaka, S. Y. Zheng, Evaluating a novel dimensional reduction approach for mechanical fractionation of cells using a tandem flexible micro spring array (tFMSA), *Lab Chip* **2017**, *17*, 691.

14. R. Rosenberg, R. Gertler, J. Friederichs, K. Fuehrer, M. Dahm et al. Comparison of two density gradient centrifugation systems for the enrichment of disseminated tumor cells in blood, *Cytometry* **2002**, *49*, 150.

15. L. S. Lim, M. Hu, M. C. Huang, W. C. Cheong, A. T. L. Gan et al. Microsieve lab-chip device for rapid enumeration and fluorescence in situ hybridization of circulating tumor cells, *Lab Chip* **2012**, *12*, 4388.

16. J. V. Green, S. K. Murthy, Microfluidic enrichment of a target cell type from a heterogenous suspension by adhesion-based negative selection, *Lab Chip* **2009**, *9*, 2245.

17. S. Nagrath, L. V. Sequist, S. Maheswaran, D. W. Bell, D. Irimia et al. Isolation of rare circulating tumour cells in cancer patients by microchip technology, *Nature* **2007**, *450*, 1235.

18. N. G. Zhang, Y. L. Deng, Q. D. Tai, B. R. Cheng, L. B. Zhao et al. Electrospun TiO2 nanofiber-based cell capture assay for detecting circulating tumor cells from colorectal and gastric cancer patients, *Adv. Mater*. **2012**, *24*, 2756.

19. J. H. Myung, K. A. Gajjar, J. Saric, D. T. Eddington, S. Hong, Dendrimer-mediated multivalent binding for the enhanced capture of tumor cells, *Angew. Chemie. Int. Ed.* **2011**, *50*, 11769.

20. S. Bamrungsap, T. Chen, M. I. Shukoor, Z. Chen, K. Sefah et al. Pattern recognition of cancer cells using aptamer-conjugated magnetic nanoparticles, *ACS Nano* **2012**, *6*, 3974.

21. S. Riethdorf, H. Fritsche, V. Muller, T. Rau, C. Schindlbeck et al. Detection of circulating tumor cells in peripheral blood of patients with metastatic breast cancer: a validation study of the CellSearch system, *Clin. Cancer Res*. **2007**, *13*, 920.

22. H. J. Yoon, T. H. Kim, Z. Zhang, E. Azizi, T. M. Pham et al. Sensitive capture of circulating tumour cells by functionalized graphene oxide nanosheets, *Nat. Nanotechnol*. **2013**, *8*, 735.

23. S. Wang, K. Liu, J. Liu, Z. T. Yu, X. Xu et al. Highly efficient capture of circulating tumor cells by using nanostructured silicon substrates with integrated chaotic micromixers, *Angew. Chemie. Int. Ed.* **2011**, *50*, 3084.

24. M. H. Park, E. Reategui, W. Li, S. N. Tessier, K. H. K. Wong et al. Enhanced isolation and release of circulating tumor cells using nanoparticle binding and ligand exchange in a microfluidic chip, *J Am. Chem. Soc*. **2017**, *139*, 2741.

25. K. Xiong, W. Wei, Y. Jin, S. Wang, D. Zhao et al. Biomimetic immuno-magnetosomes for high-performance enrichment of circulating tumor cells, *Adv. Mater*. **2016**, *28*, 7929.

26. N. N. Lu, M. Xie, J. Wang, S. W. Lv, J. S. Yi et al. Biotin-triggered decomposable immunomagnetic beads for capture and release of circulating tumor cells, *ACS Appl. Mater. Interfaces*. **2015**, *7*, 8817.

27. L. M. Millner, M. W. Linder, R. Valdes, Circulating tumor cells: a review of present methods and the need to identify heterogeneous phenotypes, *Ann. Clin. Lab*. *Sci*. **2013**, *43*, 295.

28. W. Hong, S. Lee, H. J. Chang, E. S. Lee, Y. Cho, Multifunctional magnetic nanowires: A novel breakthrough for ultrasensitive detection and isolation of rare cancer cells from non-metastatic early breast cancer patients using small volumes of blood, *Biomaterials* **2016**, *106*, 78.

29. R. E. Payne, E. Yague, M. J. Slade, C. Apostolopoulos, L. R. Jiao et al. Measurements of EGFR expression on circulating tumor cells are reproducible over time in metastatic breast cancer patients, *Pharmacogenomics* **2009**, *10*, 51.

30. M. Pestrin, S. Bessi, F. Galardi, M. Truglia, A. Biggeri et al. Correlation of HER2 status between primary tumors and corresponding circulating tumor cells in advanced breast cancer patients, *Breast Cancer Res. Treat*. **2009**, *118*, 523.

31. A. Satelli, Z. Brownlee, A. Mitra, Q. H. Meng, S. Li, Circulating tumor cell enumeration with a combination of epithelial cell adhesion molecule-and cell-surface vimentin-based methods for monitoring breast cancer therapeutic response, *Clin. Chem*. **2015**, *61*, 259.

32. K. A. Hyun, G. B. Koo, H. Han, J. Sohn, W. Choi et al. Epithelial-to-mesenchymal transition leads to loss of EpCAM and different physical properties in circulating tumor cells from metastatic breast cancer, *Oncotarget* **2016**, *7*, 24677.

33. A. Martowicz, G. Spizzo, G. Gastl, G. Untergasser, Phenotype-dependent effects of EpCAM expression on growth and invasion of human breast cancer cell lines, *BMC Cancer* **2012**, *12*, 1.

34. P. Banko, S. Y. Lee, V. Nagygyörgy, M. Zrinyi, C. H. Chae et al. Technologies for circulating tumor cell separation from whole blood, *J. Hematol. Oncol*. **2019**, *12*, 1.

35. M. J. M. Magbanua, J. W. Park, Isolation of circulating tumor cells by immunomagnetic enrichment and fluorescence-activated cell sorting (IE/FACS) for molecular profiling, *Methods* **2013**, *64*, 114.

36. L. W. Arnold, J. Lannigan, Practical issues in high-speed cell sorting, *Curr. Protoc. Cytom*. **2010**, *51*, 1.

37. P. G. Schiro, M. Zhao, J. S. Kuo, K. M. Koehler, D. E. Sabath et al. Sensitive and high-throughput isolation of rare cells from peripheral blood with ensemble-decision aliquot ranking, *Angew. Chem. Int. Ed*. **2012**, *51*, 4618.

38. L. S. Lim, M. Hu, M. C. Huang, W. C. Cheong, A. T. L. Gan et al. Microsieve lab-chip device for rapid enumeration and fluorescence in situ hybridization of circulating tumor cells, *Lab Chip* **2012**, *12*, 4388.

39. T. H. Kim, M. Lim, J. Park, J. M. Oh, H. Kim et al. FAST: Size-selective, clog-free isolation of rare cancer cells from whole blood at a liquid-liquid interface, *Anal. Chem*. **2017**, *89*, 1155.

40. S. S. Huang, R. N. Li, Y. X. Qu, J. Shen, J. Liu, Fluorescent biological label for recognizing human ovarian tumor cells based on fluorescent nanoparticles, *J. Fluoresc.* **2009**, *19*, 1095.

41. L. Tao, C. J. Song, Y. J. Sun, X. H. Li, Y. Y. Li et al. A fluorescent and chemiluminescent difunctional mesoporous silica nanoparticle as a label for the ultrasensitive detection of cancer cells, *Anal. Chim. Acta* **2013**, *761*, 194.

42. J. M. Rosenholm, A. Meinander, E. Peuhu, R. Niemi, J. E. Eriksson et al. Targeting of porous hybrid silica nanoparticles to cancer cells, *ACS Nano* **2009**, *3*, 197.

43. T. Deng, J. Li, L. L. Zhang, J. H. Jiang, J. N. Chen et al. A sensitive fluorescence anisotropy method for the direct detection of cancer cells in whole blood based on aptamer-conjugated near-infrared fluorescent nanoparticles, *Biosens. Bioelectron*. **2010**, *25*, 1587.

44. C. E. Yoo, H. S. Moon, Y. J. Kim, J. M. Park, D. Park et al. Highly dense, optically inactive silica microbeads for the isolation and identification of circulating tumor cells, *Biomaterials* **2016**, *75*, 271.

45. Z. Shen, A. Wu, X. Chen, Current detection technologies for circulating tumor cells, *Chem. Soc. Rev.* **2017**, *46*, 2038.

46. F. Grillet, E. Bayet, O. Villeronce, L. Zappia, E. L. Lagerqvist et al. Circulating tumour cells from patients with colorectal cancer have cancer stem cell hallmarks in ex vivo culture, *Gut* **2017**, *66*, 1802.

47. C. Chen, S. Zhao, A. Karnad, J. W. Freeman, The biology and role of CD44 in cancer progression: therapeutic implications, *J. Hematol. Oncol*. **2018**, *11*, 1.

48. W. Yan, Y. Chen, Y. Yao, H. Zhang, T. Wang, Increased invasion and tumorigenicity capacity of CD44+/CD24- breast cancer MCF7 cells in vitro and in nude mice, *Cancer Cell Int.* **2013**, *13*, 1.

49. E. I. Galanzha, J. W. Kim, V. P. Zharov, Nanotechnology-based molecular photoacoustic and photothermal flow cytometry platform for in-vivo detection and killing of circulating cancer stem cells, *J. Biophotonics* **2009**, *2*, 725.

50. J. M. Park, J. Y. Lee, J. G. Lee, H. Jeong, J. M. Oh et al. Highly efficient assay of circulating tumor cells by selective sedimentation with a density gradient medium and microfiltration from whole blood, *Anal. Chem*. **2012**, *84*, 7400.

51. J. Kim, H. Cho, S. I. Han, K. H. Han, Single-cell isolation of circulating tumor cells from whole blood by lateral magnetophoretic microseparation and microfluidic dispensing, *Anal. Chem*. **2016**, *88*, 4857.

52. P. M. Poortmans, S. Collette, C. Kirkove, E. Van Limbergen, V. Budach et. al. Internal mammary and medial supraclavicular irradiation in breast cancer, *N. Engl. J. Med*. **2015**, *373*, 317.

53. B. Cheng, H. Song, S. Wang, C. Zhang, B. Wu et al. Quantification of rare cancer cells in patients with gastrointestinal cancer by nanostructured substrate, *Transl. Oncol*. **2014**, *7*, 720.

54. P. Wee, Z. Wang, Epidermal growth factor receptor cell proliferation signaling pathways, *Cancers* **2017**, *9*, 1.

55. T. Ohnaga, Y. Takei, T. Nagata, Y. Shimada, Highly efficient capture of cancer cells expressing EGFR by microfluidic methods based on antigen-antibody association, *Sci. Rep*. **2018**, *8*, 1.

56. Y. Ohsaki, S. Tanno, Y. Fujita, E. Toyoshima, S. Fujiuchi et al. Epidermal growth factor receptor expression correlates with poor prognosis in non-small cell lung cancer patients with P53 overexpression, *Oncol. Rep*. **2000**, *7*, 603.

Chapter 4

Sensitizer-sensor nanoassembly for intracellular singlet oxygen detection and bioimaging

Abstract

Intracellular singlet oxygen ($^1O_2$) generation and detection play a key role in PDT to treat various cancers. Although photosensitizer nanoparticles and organic molecules promise photodynamic therapy, the PDT efficacy is limited due to certain existing limitations or their inherent features. Thus, programmed nanomaterials for controlled photosensitization and intracellular $^1O_2$ generation, trapping, and releasing have great potential to augment cancer therapy. This chapter introduces a novel sensor-sensitizer incorporated multifunctional mesoporous silica nanoassembly promising for efficient PDT. I demonstrate the potential of this nanoassembly to produce, store, release, and sense $^1O_2$ at the single-particle level and in living cells. The small size of the nanoassembly, within the diffusion length of $^1O_2$ in cells and tissues, allows for extremely efficient $^1O_2$ storing and releasing. I illustrate the potential of the nanoassembly for $^1O_2$-mediated therapy by synthesizing an anthracene-coumarin-dioctylamine conjugate. The $^1O_2$ sensing efficiency of this molecule is studied using steady-state absorption and fluorescence spectroscopy. The fluorescence of coumarin in the sensor or the nanoassembly is quantitatively quenched by the efficient intramolecular electron transfer from the aminomethyl anthracene moiety and under one- or two-photon excitation, a >230-fold fluorescence enhancement is observed, which is the highest compared to the previously reported molecules. High sensitivity and controlled release of $^1O_2$ are attained using a UV or Vis source. The sensor also shows good photostability in room light, unlike the commercial $^1O_2$ probes. Further, the conjugation of cell-penetrating ligands to the nanoassembly enables its utilization for biological applications. The cellular uptake of the nanoassembly is facilitated by macropinocytosis or passive delivery, which is confirmed by confocal imaging. In addition, the nanoassembly provides the red fluorescence of the photosensitizer and intense blue

emission from the uncaged sensor for synergized fluorescence-guided cell imaging and $^1O_2$ induced cell death.

4.1 Introduction

PDT has emerged as a safe, powerful, and cost-effective treatment modality in cancer management as an alternative to conventional cancer treatment modalities. This minimally invasive technique has high spatiotemporal precision, reduced extended morbidity, and low toxicity which involve a combination of tumor-localizing photosensitizer (PS), oxygen molecule, and light for local illumination. Reactive oxygen species (ROS) mediated PDT, particularly the highly reactive cytotoxic singlet oxygen (1O2), is effective for disrupting tumor microvasculature, oxidative stress-induced cellular damage, and impairment of membrane transport functions.[1-3] The principle of $^1O_2$ generation by PDT is schematically shown in Figure 4.1. By absorbing photons of suitable energy, the PS reaches the excited short-lived singlet state (^{1}PS*), which can undergo a series of processes such as nonradiative decay or radiative decay to the ground singlet state (S_0), proton or electron transfer to the substrate, or inter-system crossing (ISC) to generate the long-lived triplet excited state (^{3}PS*). The radiative relaxation emits fluorescence which is utilized for clinical imaging and photodetection. The singlet and triplet excited states of a PS can directly interact with a neighboring substrate such as a biomolecule and form radical cations or anions by the transfer of an electron or proton, which produce ROS such as superoxide anion radicals, hydroxyl radicals, and hydrogen peroxide after reacting with the molecular oxygen (Type I mechanism). Alternatively, the excited triplet state PS can transfer a part of its energy to the ground triplet state oxygen ($^3O_2$, $^3\Sigma_g^-$) by the triplet-triplet energy transfer (TTET) and generates the highly reactive $^1O_2$ (Type II mechanism). The transition energy required for forming $^1O_2$ from $^3O_2$ is very small (22 kcal/mol), which corresponds to 1274 nm. Studies indicate Type II mechanism as a dominant pathway for $^1O_2$ generation, which depends on the efficiency of ISC in a PDT process.[4,5] However, when an exciplex is formed during the reaction of ^{1}PS* with the substrate or solvent molecule, it prefers back electron transfer (BET). It returns to the ground state instead of an electron transfer to generate the radical species.[6] But the same process with ^{3}PS* results in the formation of radical species, generating the ROS. Here, the hyperfine or spin-orbit coupling breaks the multiplicity of the exciplex, and the BET process becomes spin forbidden. The $^1O_2$ produced by PS drugs

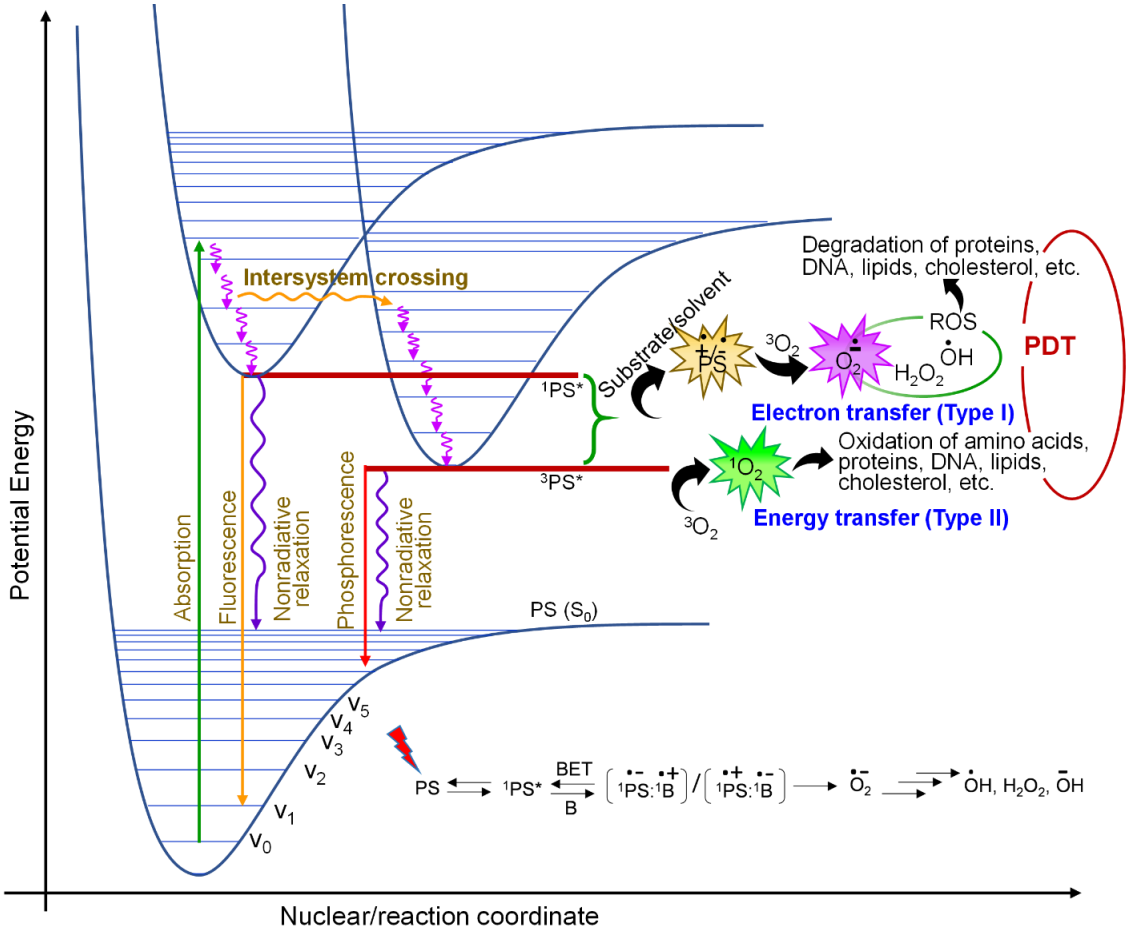

Figure 4.1. A scheme showing the mechanism of ROS and $^1O_2$ generation in the PDT process. 'B' or 'S' is a biomolecule or a substrate that acts as an electron donor or acceptor.

must be precisely delivered to the biological target to avoid any undesired toxicity by the overdose or non-specific drug localization. NPs offer multifarious advantages in PDT to alleviate the challenges associated with conventional PDT, and a variety of multifunctional theranostic nanocarriers have been recently developed.[7-11] The preparation of biodegradable NPs containing phthalocyanines and naphthalocyanines for PDT application was first reported by Labib *et al.* in 1991.[12] The high surface-to-volume ratio of NPs increases the loading of photoactive molecules and delivery efficiencies by preventing non-specific accumulation in the normal tissues.[13] They enhance the solubility of PS drugs and offer multifunctionality to incorporate many functional or targeting agents that modulate the biophysical properties of NPs. This includes the design of NPs with imaging agents, targeting ligands, chemo-drugs, and cloaking agents, which improve biodistribution, cellular uptake, and pharmacokinetics.

Further, the delivery of the NPs is facilitated by the enhanced permeability and retention effect (EPR) that enhances the diffusion and retention of the PS drugs within the tumor regions. Among such NPs, silica NPs are promising for PDT applications. Incorporating PSs in silica NPs by chemical functionalization protects the intrinsic fluorescence properties and promotes the aqueous solubility.[14-17] Silica NPs are chemically inert, transparent to light absorption, and not susceptible to varying pH conditions. In addition, the tunable size, shape, porosity and dispersibility, and ease of surface modifications offer great flexibility for the silica NPs. Apart from the existence of PS drugs, the need for a $^1O_2$ sensor is crucial to overcome the limitations of photooxygenation techniques for PDT.[18-21,45] Programmed nanomaterials integrating PS drugs, $^1O_2$ storage, sensing, and releasing moieties in a single architecture are highly demanding for next-generation PDT. Recently, an array of fluorescent probes based on polycyclic aromatic hydrocarbons and heterocyclic architectures are developed to detect and sense $^1O_2$.[22-27] But the performances of such probes are limited due to the inadequate fluorescence sensitivity or the complexity in synthesis. Also, the self-limiting factor of $^1O_2$ contributes to the hypoxic microenvironment in tumors and thus promotes cancer metastasis or builds up a resistance toward phototherapy.[28-32] Among the reported $^1O_2$ sensors, anthracene derivatives conjugated to fluorophores dominate as safe $^1O_2$ sensors and carriers due to their electron-rich nature, $^1O_2$ reactivity, and clean reaction.

The substituents at the 9- or 10-positions of anthracene modulate the sensitivity of $^1O_2$ detection.[33-37] Jiao *et al.* prepared a silica nanocarrier functionalized with the PS protoporphyrin IX, a 2-pyridone derivative as the $^1O_2$ storage/release unit, and a cyanine derivative as the $^1O_2$ self-monitoring unit for efficient fractional PDT.[38] Under light irradiation, endoperoxide is formed by the generation of $^1O_2$, and the stored $^1O_2$ is released in the dark by a cycloreversion mechanism. This was monitored by the fluorescence quenching of the cyanine dye. In another report, Stang *et al.* developed an organoplatinum(II) supramolecular metallacycle by coordination-driven self-assembly of dipyridylanthracene donor - Pt(II) acceptor for reversible $^1O_2$ capture and release. This nanocarrier showed high photooxygenation and thermolysis rates.[39] Hence, accurate detection and controlled supply of $^1O_2$ using probes with high spatiotemporal sensitivity are important for advancing PDT.

In this chapter, I report the synthesis of an aminomethylanthracene-coumarin-based $^1O_2$ sensor. I have also functionalized mesoporous silica NPs with PSs or $^1O_2$ sensors to construct different nanoassemblies and demonstrated their ability to continuously produce, store, release, and sense $^1O_2$ at the ensemble and single-particle levels, and in living cells using steady-state

absorption and fluorescence spectroscopy, single-particle, and confocal laser scanning imaging. The nano-size and multiple sensor-sensitizer conjugates of the assembly allow for efficient $^1O_2$ storing-sensing-releasing even at the single-cell and single-particle levels. In the absence of light, the fluorescence of coumarin is quantitatively quenched. Still, in the presence of $^1O_2$ generated by the PSs, I observed an enormous enhancement in the fluorescence intensity of the sensor under one- or two-photon excitation. The mechanism for this huge fluorescence enhancement is discussed in this chapter. The results showed an outstanding $^1O_2$-induced fluorescence turn-on efficiency at a controlled rate compared to the previously reported probes.[40] To further utilize the sensor for biological applications, I conjugated the nanoassembly with arginine-rich peptides. The nanoassembly showed enhanced cellular uptake and good biocompatibility. Along with the production and release of $^1O_2$ inside the cells, the nanoassembly provides bimodal fluorescence of the PSs and the sensor, promising for fluorescence-guided tumor cell imaging and $^1O_2$-induced cell death.

4.2 Results and discussion

4.2.1 Synthesis and characterization of a $^1O_2$ sensor

The $^1O_2$ sensors **4** or **5** were synthesized by a one-pot, base-catalyzed nucleophilic substitution reaction between 9,10-bis(chloromethyl) anthracene, 7-amino-4-methylcoumarin and *N*,*N*-dioctylamine (Figure 4.2). The structures were characterized by ^{1}H NMR and ^{13}C NMR

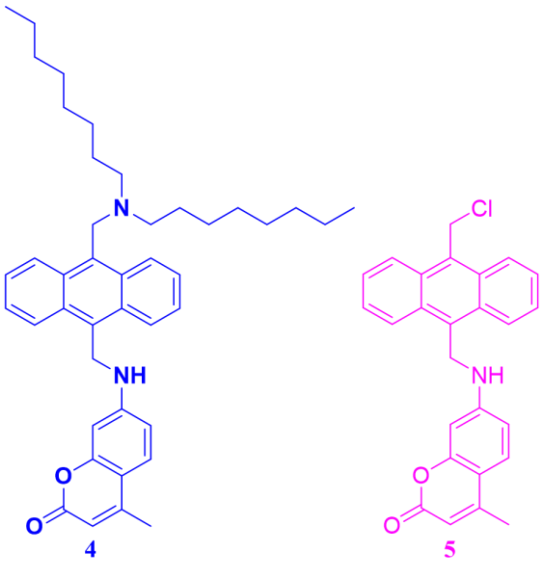

Figure 4.2. The structures of $^1O_2$ sensors **4** and **5** used in this work.

spectroscopy. The synthetic procedure and the characterization results are provided in Chapter 2.

4.2.2 Synthesis and characterization of a sensor-sensitizer-silica (SSS) and a sensor-silica (SS) nanoassemblies

To prepare mesoporous silica-based SS or SSS nanoassemblies, the intermediate **5** was isolated, and the PS TCPP or **5** were attached covalently to the amino-functionalized silica NPs (Chapter 2). The covalent attachment of moieties onto the silica matrix prevents the undesired leaching of molecules and thus maintains the photoactivity of the PS and sensor. The functionalized silica NPs were characterized by SEM as shown in Figure 4.3. The images showed a uniform

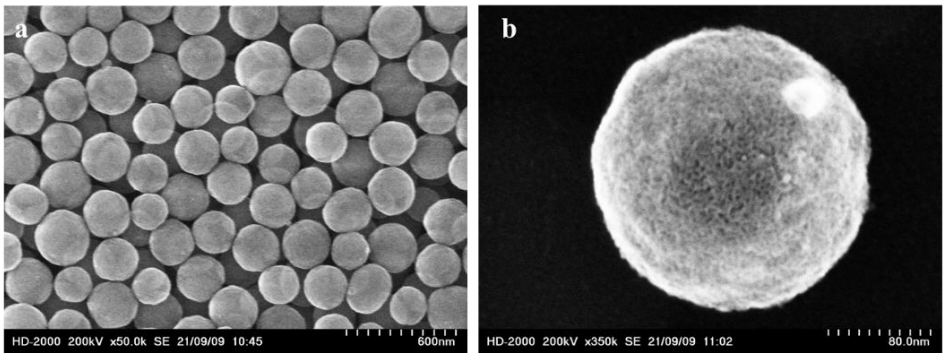

Figure 4.3. SEM images of functionalized silica a) before and b) after surface modification.

spherical morphology of the NPs, with an average size of 200 nm. The integration of PSs with silica NPs overcomes the limitations associated with first- and second-generation PS drugs in terms of hydrophilicity, tumor specificity, and tumor-penetration ability.[15,16] I chose TCPP as the PS in constructing the nanoassembly due to the tetravalency of porphyrin, which helps in facile functionalization. Also, the fluorescence of TCPP in the red region opens intriguing possibilities in image-guided therapeutics.

4.2.3 The mechanism of $^1O_2$ generation, storage, release, and sensing

The TCPP molecules conjugated to the nanoassemblies on suitable excitation by the light source generate $^1O_2$ by sensitizing the molecular oxygen. The aminomethyl anthracene

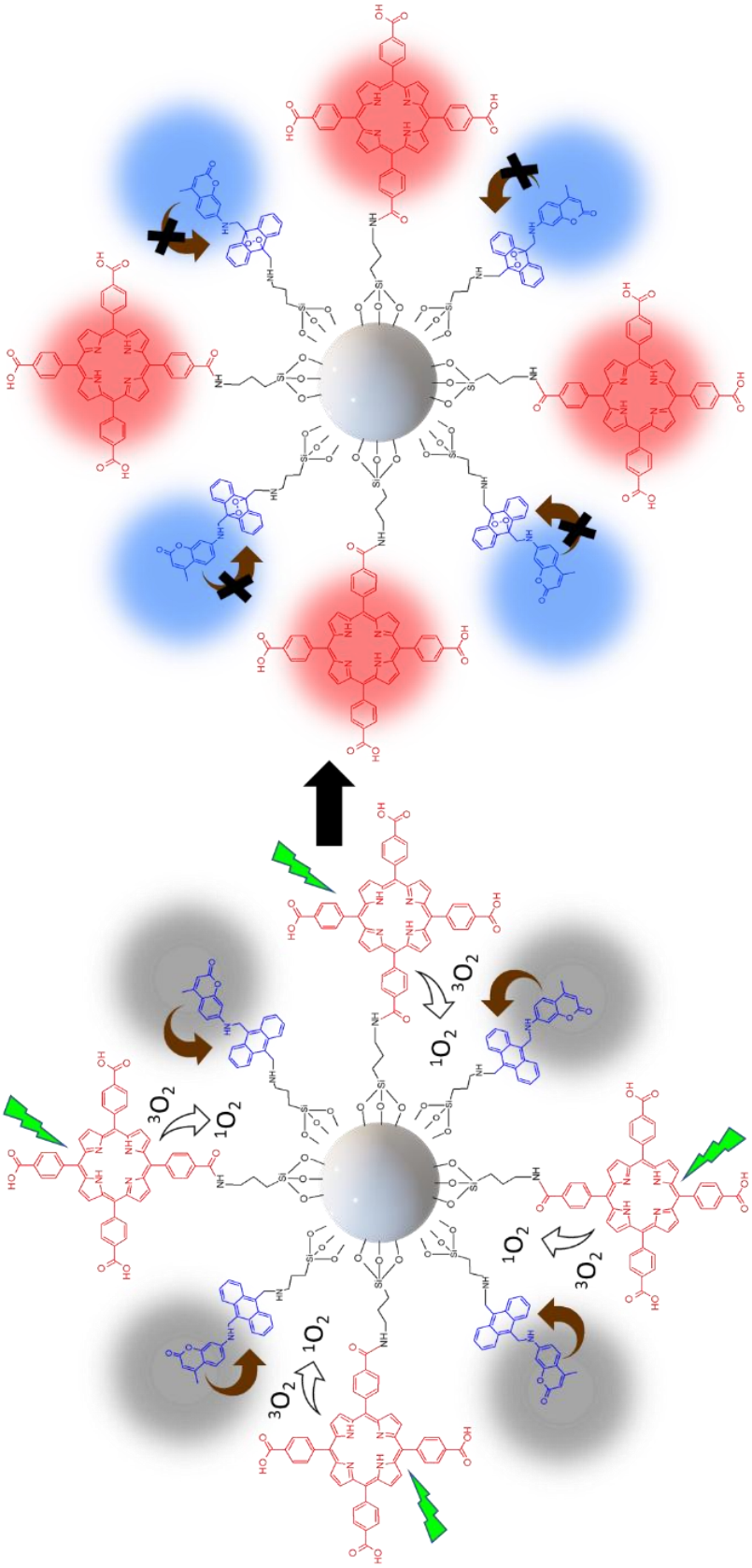

Figure 4.4. A scheme showing $^1O_2$ generation by TCPP, and blue fluorescence uncaging due to oxidation of the sensor.

group sandwiched between the silica and coumarin fluorophore shows selective capturing of $^1O_2$ by [2+4] cycloaddition reaction forming a 9,10-endoperoxide and releasing the quenched fluorescence of the coumarin chromophore. Without $^1O_2$, these donor-acceptor dyads are weakly fluorescent due to the efficient intramolecular electron transfer between the two moieties. Upon the generation of $^1O_2$ by PS, the photoinduced electron transfer (PET) is blocked due to the oxidation of anthracene by $^1O_2$, and thus the chromophore exhibits intense fluorescence.[41] This process is schematically shown in Figure 4.4.

4.2.4 $^1O_2$ generation and detection at the ensemble level

First, I investigated the efficiency of the SSS nanoassembly for $^1O_2$ detection by measuring the photophysical properties of sensor **4** in the solution phase. The UV-light-induced fluorescence of sensor **4** showed a >230-fold intensity enhancement (Figure 4.5a). To understand the reasonfor this huge fluorescence increase, I performed the experiment in the presence of an efficient $^1O_2$ scavenger such as sodium azide (NaN_3). A remarkable increase in the fluorescence intensity was observed under 365 nm irradiation, whereas no change in the intensity was observed using 532 nm excitation. This ruled out the possibility of self-sensitization by sensor **4** (Figure 4.5 b,c). Thus, according to previous reports, the increased fluorescence of the coumarin unit is due to the [4+4] photodimerization of the anthracene groups to form dibenzobarrelene derivative (Figure 4.5 d).[41]

The molar extinction coefficient of sensor **4** was calculated to be ~ 26700 M^{-1} cm^{-1}, from the steady-state absorption measurements (Figure 4.6a). $^1O_2$ trapping, storing, and releasing ability of sensor **4** was studied by irradiating a solution of sensor **4** (10 µM) and TCPP (5 µM) in acetonitrile with a 532 nm laser. The $^1O_2$ generated by TCPP is trapped by sensor **4**, forming a non-fluorescent exciplex which further transforms to a less fluorescent endoperoxide. This isindicated by a >60-fold fluorescence intensity enhancement of sensor **4**, as shown in Figure 4.7a,d. On subsequent irradiation of the solution with UV light, the fluorescence intensity showed an enormous enhancement (>225-fold) from its initial non-fluorescent state (Figure 4.7c,d). Here, the nonfluorescent intermediate and the less fluorescent endoperoxide undergo decomposition to release the trapped $^1O_2$, 9,10-anthraquinone, and the highly fluorescent coumarin fluorophore as the main photoproducts by 365 nm irradiation (Figure 4.7e).[42,43] This takes place by the thermal cleavage of O-O and C-C bonds in the endoperoxide, which is common for alkyl-substituted anthracenes.[44] Also, the decay of the anthracene vibronic bands

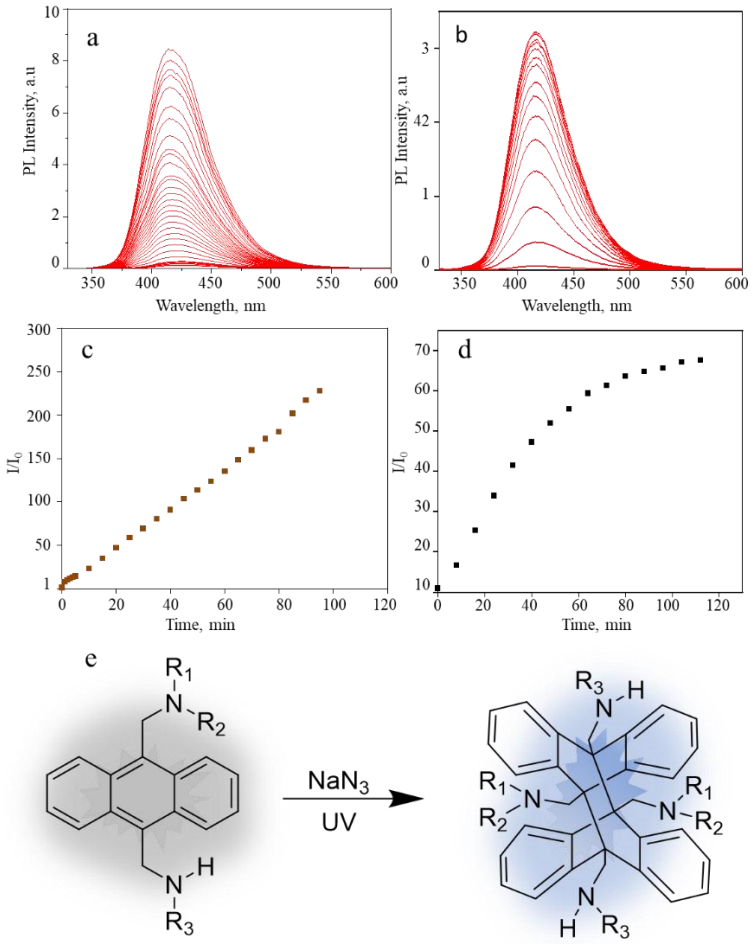

Figure 4.5. (a,b) Fluorescence spectra (λ_{ex}=320 nm) of (a) **4** in CH_3CN before and after irradiation at 365 nm for 95 min, inset: time-trace of the peak fluorescence intensities, (b) a mixture of **4** (10 μM) and NaN_3 (150 μM) in CH_3CN before and after irradiation at 365 nm for 112 min. (c,d) Time-trace of the peak fluorescence intensities in (c) figure a and (d) figure b. (e) A scheme showing the UV-induced dimerization of the sensor.

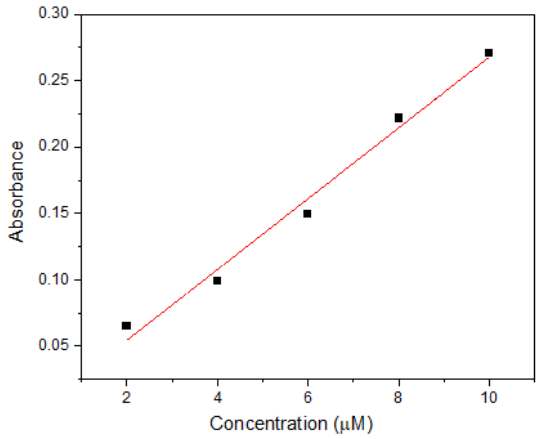

Figure 4.6. (a) The absorbance-concentration plot for sensor **4** in CH3CN. The absorbance at 378 nm is used.

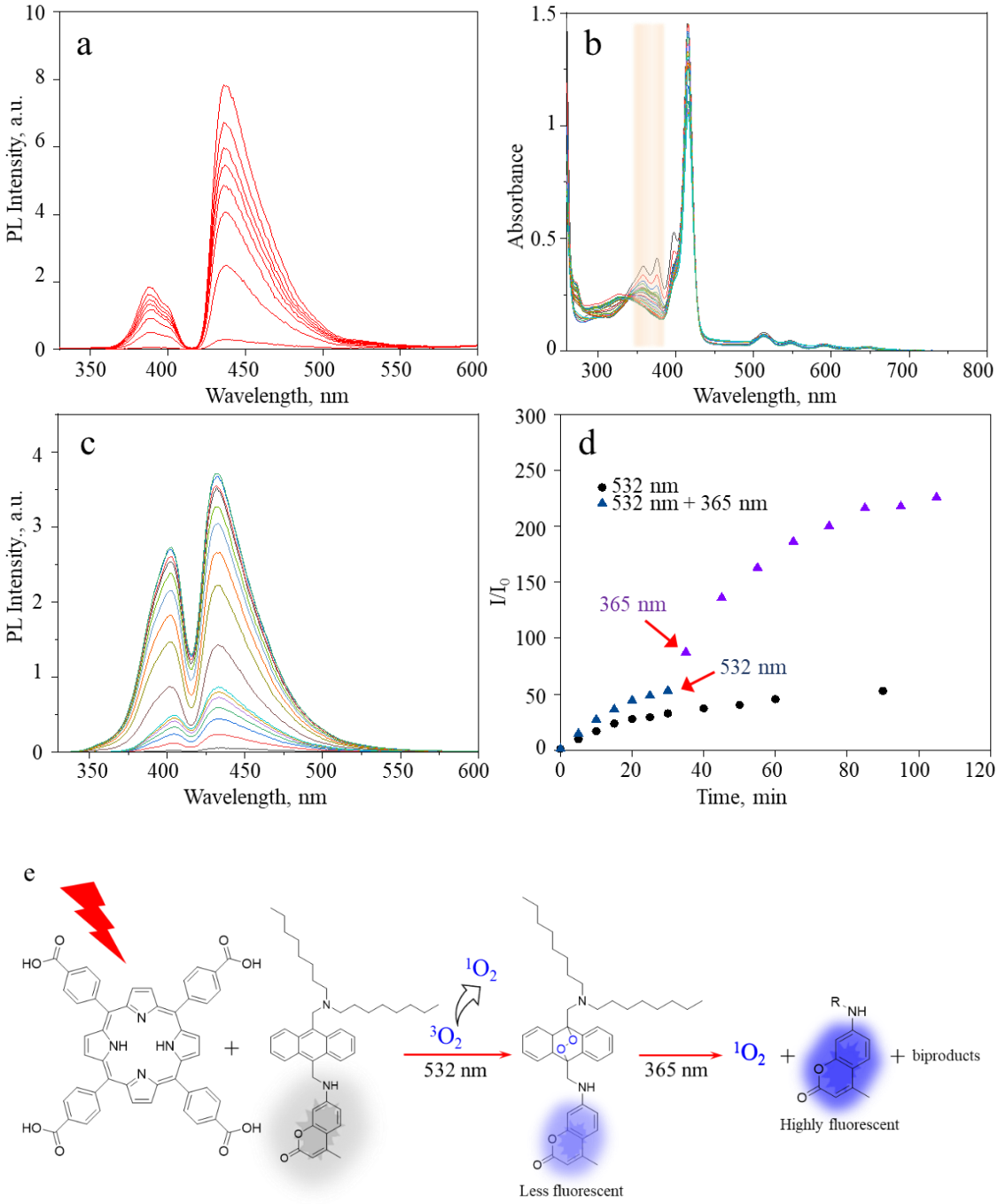

Figure 4.7. (a) Fluorescence spectra (λ_{ex}=320 nm) of a mixture of **4** (10 μM) and TCPP (5 μM) in CH_3CN before and after photoactivation at 532 nm (50 mW cm^{-2}) for 90 min. (b) Absorption and (c) fluorescence spectra of a mixture of **4** (10 μM) and TCPP (5 μM) in CH_3CN before and after photoactivation at 532 nm (50 mW cm^{-2}) for 30 min, followed by UV illumination (365 nm) for 100 min. (d) Time-trace of the peak fluorescence intensities at different conditions. (e) A scheme showing UV-vis induced two-step fluorescence enhancement of **4**.

ca. 356 nm, 376 nm, and 396 nm in the absorption spectrum and the gradual appearance of peak ca. 325 nm indicate the $^1O_2$-mediated photo-oxidation of anthracene, forming anthraquinone (Figure 4.7b).

The fluorescence sensitivity of sensor **4** is exceptionally high compared to the previously reported probes due to the facile intramolecular electron transfer favored by the aminomethyl groups in the molecule that decreases the oxidation potential of anthracene. The fluorescence intensity enhancement was confirmed from the UV light-induced, time-dependent fluorescence images of a solution containing sensor **4** with or without TCPP after 532 nm laser excitation. The $^1O_2$ generated by the photoactivated TCPP is captured and released by the sensor, as seen by the brilliant magenta emission in Figure 4.8. Whereas, an intense blue emission is observed from a solution of sensor **4** due to the photodimerization.

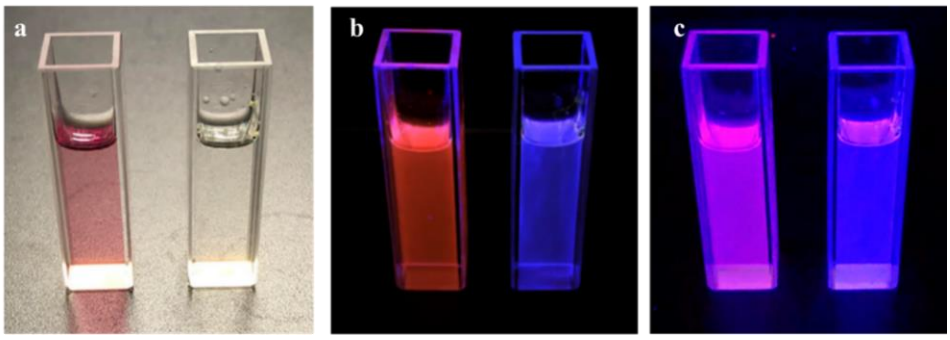

Figure 4.8. Fluorescence images of (left) a mixture of **4** and TCPP and (right) **4** (a) before UV illumination and (b,c) after UV illumination for (b) 1 min and (c) 5 min; the samples were photoactivated at 532 nm before UV illumination.

I also investigated the $^1O_2$ storing ability of the SS and SSS nanoassemblies by the intermolecular or intraparticle sensitization of TCPP (Figure 4.9a-c). The time-trace fluorescence intensity curve showed an efficient intramolecular photogeneration and capturing of $^1O_2$ by SSS than the intermolecular transfer between SS and a solution of TCPP. This was further confirmed by the fluorescence images of the SSS nanoassembly (Figure 4.9d-f). Hence, these results demonstrate the outstanding sensitivity of sensor **4** for $^1O_2$ trapping, storing, and releasing for PDT applications.

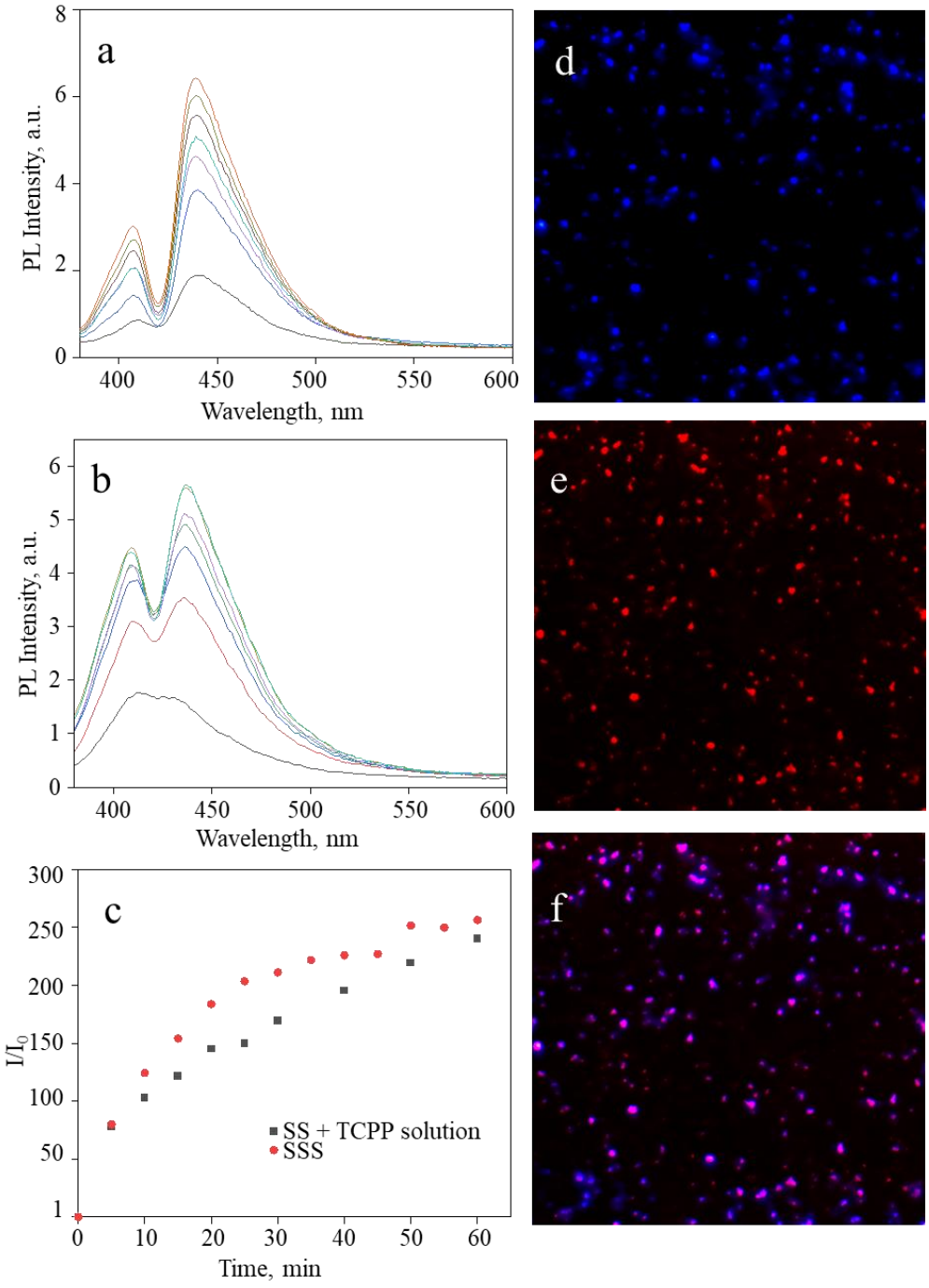

Figure 4.9. Fluorescence spectra (λ_{ex}=320 nm) of (a) SS in a TCPP solution (5 μM) and (b) SSS in DMF before and after photoactivation at 532 nm (50 mW cm^{-2}) for 60 min, (c) time-trace of the peak fluorescence intensities in figure a and b. (d-f) Fluorescence images (λ_{ex}=532 nm) of SSS NPs collected using a (d) 420-480 nm BP filter, (e) 580 LP filter, and (f) overlay image of d and e. The image sizes are 80 x 80 μm^2.

4.2.5 $^1O_2$ generation and detection at the single-particle level

I further studied the photostability and $^1O_2$ trapping, storing, sensing, and releasing abilities of the nanoassemblies at the single-particle level (Figure 4.10). The as-prepared SSS nanoassembly showed intense red fluorescence of TCPP under 532 nm laser excitation. The fluorescence of the coumarin moiety ca 430 nm was below the detection limit of an EMCCD camera due to the fluorescence quenching by intraparticle electron transfer in **4**. With continuous 365 nm excitation, the fluorescence intensity increased and saturated, consistent with the fluorescence uncaging property of **4**.

To analyze the $^1O_2$ trapping behavior of the sensors in SS dispersed in a TCPP solution or SSS in water, I excited the TCPP in a solution (for SS) or on the SSS NPs using a 532 nm laser for 30 s. The UV-light induced, time-dependent sensing and release of $^1O_2$ were monitored by continuous irradiation of the samples with 365 nm light for 2 min after each step of photosensitization. The PL intensity trajectories from a large number of NPs were collected and analyzed. Figure 4.10a,b represent the trajectory collected from one such NP. The data was further deconvoluted to understand the enhancement in the photo-response of the sensor, as shown in the fluorescence intensity trajectories. Figure 4.10d shows the $^1O_2$ capture and storing ability of the sensor, forming its corresponding 9,10-endoperoxide. As shown, the fluorescence intensity of the sensor in SSS shows a remarkable time-dependent enhancement compared to the SS NPs after 532 nm photosensitization. This is due to higher $^1O_2$ caging and sensing efficiency when the sensor and PS are in close proximity. Whereas the $^1O_2$ capturing and sensing is less efficient in SS NPs due to the large degree of diffusion freedom for $^1O_2$ produced in the solution. Figure 4.10e shows the UV-induced $^1O_2$ releasing abilities of the nanoassemblies. Both systems showed a temporally controlled release of $^1O_2$, indicated by the stepwise increases of the fluorescence intensity. Thus, the designed SSS acts

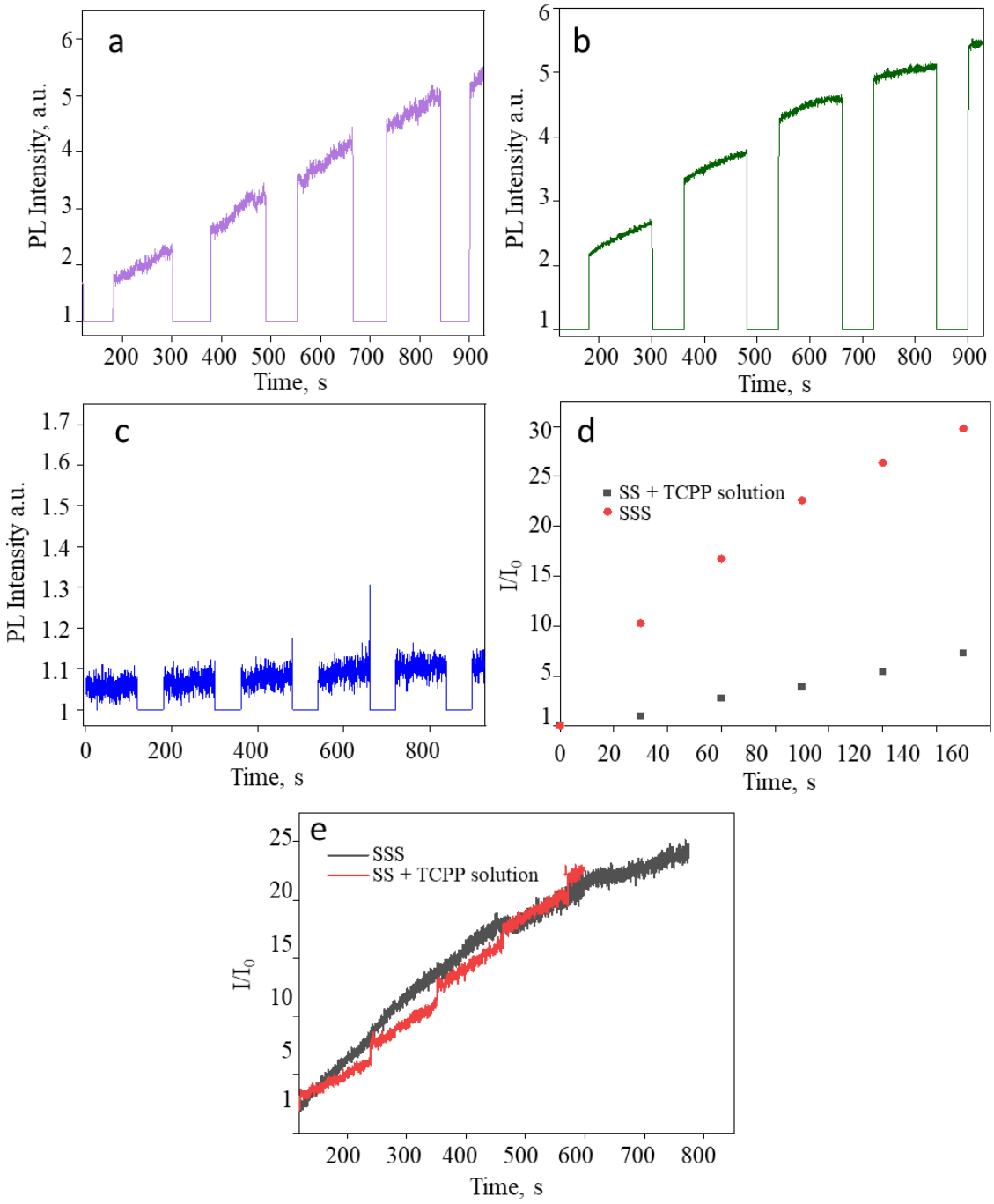

Figure 4.10. (a-c) Fluorescence intensity trajectories showing (a,b) $^1O_2$ production detected for (a) SS NPs in a TCPP solution, and (b) SSS NPs in water under 532 nm laser irradiation for 30 s intervals and UV illumination for 2 min intervals. (c) The effect of UV light (365 nm) on SS NPs in water. (d,e) Time-trace of the fluorescence intensities in Figures 2a,b showing (d) photoinduced $^1O_2$ capturing and storing by **4** and (e) UV-induced releasing of trapped $^1O_2$.

as a nanoreactor that promotes the photo-oxidation reactions and ensures a controlled and sustained release of $^1O_2$. I also examined the photostability of sensor **4** under continuous UV light illumination. Figure 4.10c shows the fluorescence intensity trajectories of SS in water under prolonged UV irradiation, suggesting low photodimerization efficiency and good photostability of the sensor **4**.

Red and NIR exciting QDs are used in PDT studies due to their deep tissue penetration, improved water solubility, and biocompatibility.[46,47] The high photostability and absorption cross-section of QDs make them suitable as energy donor species to produce $^1O_2$.[48] Thus, I studied the $^1O_2$ generation and releasing properties of the Si-sensor-QD655 nanoassembly by exciting QD655 using a 532 nm laser for 1 min followed by UV illumination for 2 min. As shown in Figure 4.11a, the fluorescence intensity trajectory showed a gradual increase, only at high excitation powers, whereas there was no significant enhancement at a low excitation power due to the low $^1O_2$ quantum efficiency of QDs. Hence, nanosystems utilizing QDs as PS require high excitation powers for an efficient photoinduced generation of $^1O_2$. At high power excitation, **4** displayed good $^1O_2$ trapping, storing, sensing, and releasing abilities. The

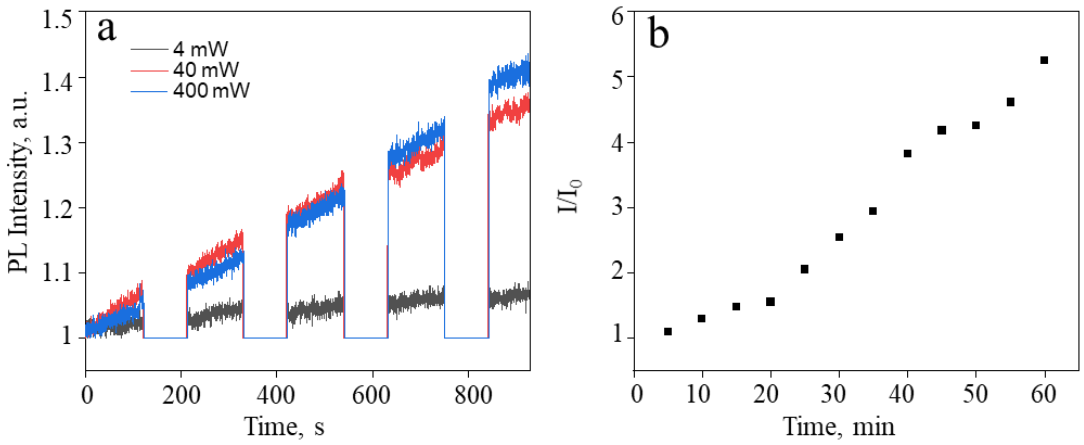

Figure 4.11. (a) Fluorescence intensity trajectories showing $^1O_2$ production by Si-sensor-QD655 NPs during intraparticle photosensitization using 532 nm laser for 1 min and UV illumination for 2 min at different excitation intensities. (b) A time trace of the peak fluorescence intensities before and after photoactivation at 532 nm (50 mW cm^{-2}) for 60 min.

ensemble level studies of Si-sensor-QD655 also showed a similar fluorescence enhancement, similar to the single-particle studies (Figure 4.11b).

4.2.6 $^1O_2$ generation and detection in cells

Finally, I investigated the cellular uptake ability of different nanoassemblies in MCF7 breast cancer cells. The cells were incubated with Syto13 dye, Si-TCPP, SS, SSS, and silica-sensor-QD655 NPs, as explained in Chapter 2. The confocal fluorescence microscopic images obtained are shown in Figure 4.12. The images showed an effective accumulation of NPs inside the cells by macropinocytosis.[50] The cells labeled with SSS showed intense red-blue emission in the cytoplasm due to the colocalized red emission from TCPP and the blue emission from sensor **4 (**Figure 4.12c**).** However, I observed a few NPs adhered to the outer cell membrane.

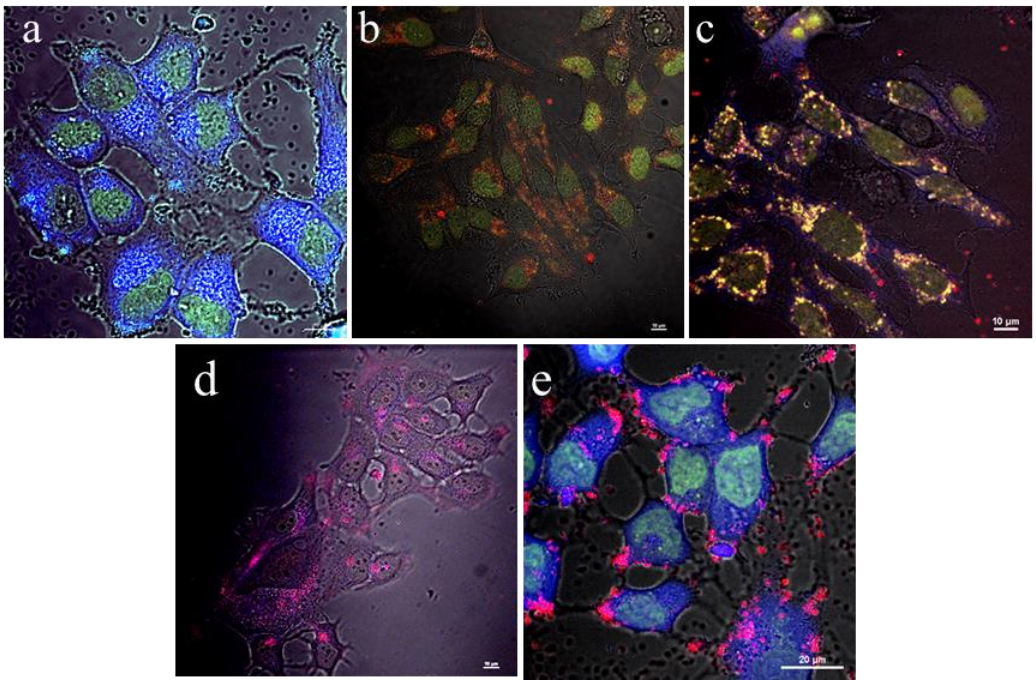

Figure 4.12. Fluorescence images of cells labeled with different NPs: (a) SS, (b) Si-TCPP, (c) SSS, (d) SSS-RGD, and (e) silica-sensor-QD655. Scale: (a,c,e) 150 x 150 µm^2, (b,d) 200 x 200 µm^2.

In the case of cells labeled with silica-sensor-QD655 NPs, the NPs were aggregated around the cell membrane which could be due to the charge-based interaction of QDs **(**Figure 4.12e).

Therefore, to increase the intracellular uptake of NPs, I functionalized the nanoassembly with cell-penetrating peptide RGD. Tumor-specific ligands conjugated to PS-NPs, denoted as third-generation nanovectors, promote the passive targeting of NPs in cells.[51] Here, I found that the cells effectively took up the RGD-conjugated NPs through $\alpha_v\beta_3$ integrin-mediated endocytosis, as shown in Figure 4.12d. This result suggests the potential of nanoassembly for fluorescence-guided PDT of tumor cells due to the co-enhanced bimodal fluorescence of TCPP and the sensor and the $^1O_2$ generation property of TCPP.

Following the cellular uptake of the nanoassembly, the intracellular $^1O_2$ generation was confirmed by single-particle fluorescence measurements and confocal time-lapse imaging. For the single-particle experiment, the cells incubated with the SSS-RGD nanoassembly were photo-irradiated continuously using 532 nm light, followed by intermittent UV illumination

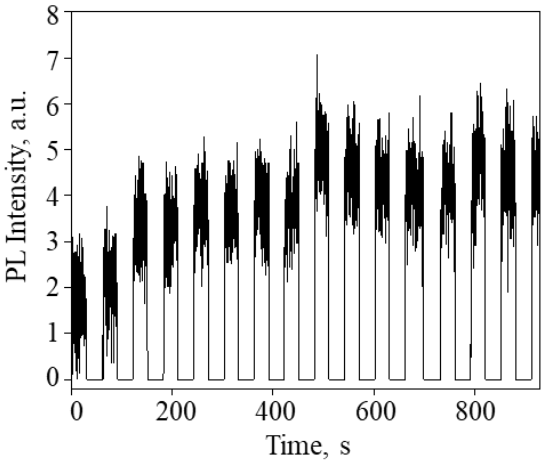

Figure 4.13. A fluorescence intensity trajectory showing $^1O_2$ production in MCF7 cells incubated with SSS-RGD NPs by continuous 532 nm laser irradiation. The intensity was recorded for each 30 s UV illumination.

and the trajectories were recorded for each step of the UV illumination. Similar to the above results, a time-correlated increase in the fluorescence intensity was seen due to an increase in the fluorescence intensity from **4** (Figure 4.13). Further, I observed the morphology changes in cells under continuous light irradiation with time during confocal imaging. Here, I observed the formation of apoptotic cells and corpuscles and cell shrinkage at high laser powers.[38] These

results confirm $^1O_2$ generated and released continuously in the intracellular environment by the photo-oxidation reaction leads to cell death mainly by apoptosis.

4.3 Conclusion

I constructed a nanomaterial scaffold for intracellular $^1O_2$ production, trapping, sensing, and controlled release by the co-assembly of a $^1O_2$ generator, a PS, and an anthracene-coumarin dyad-based sensor molecule. The sensitivity of this nanoassembly was studied using steady-state absorption and fluorescence measurements in solutions and living cells, which revealed a significant fluorescence intensity enhancement of the sensor, outraging the commercially employed $^1O_2$ sensors. The photostability and spatiotemporal controlled release ability of the nanoassembly were monitored at the single-particle level in various steps of light-induced photoactivation. The UV-light induced spatiotemporal controlled release of $^1O_2$ underscores the potential of this nano-scaffold as an intracellular $^1O_2$ probe. Further, the fluorescence cell images showed that the NP-RGD peptide conjugate is internalized and readily accumulated in the cytoplasm. Under high power laser irradiation, $^1O_2$-induced cell death was observed. Therefore, the nanoassembly can be utilized for synergized fluorescence-guided tumor cells diagnosis and PDT. Additionally, with the incorporation of efficient photothermal agents, the design can be extended further for image-guided PDT and PTT.

4.4 References

1. K. Liu, X. Liu, Q. Zeng, Y. Zhang, L. Tu et al. Covalently assembled NIR nanoplatform for simultaneous fluorescence imaging and photodynamic therapy of cancer cells, *ACS Nano* **2012**, *6*, 4054.

2. N. Zhao, B. Ding, Y. Zhang, J. L. Klockow, K. Lau et al. Reactive oxygen species and enzyme dual-responsive biocompatible drug delivery system for targeted tumor therapy, *J. Control. Release* **2020**, *324*, 330.

3. Z. Cao, D. Li, J. Wang, X. Yang, Reactive oxygen species-sensitive polymeric nanocarriers for synergistic cancer therapy, *Acta Biomater.* **2021**, *130*, 17.

4. M. R. Younis, G. He, J. Qu, J. Lin, P. Huang et al. Inorganic nanomaterials with intrinsic singlet oxygen generation for photodynamic therapy, *Adv. Sci.* **2021**, *8*, 2102587.

5. W. Wu, X. Shao, J. Zhao, M. Wu, Controllable photodynamic therapy implemented by regulating singlet oxygen efficiency, *Adv. Sci.* **2017**, *4*, 1700113.

6. A. Anaz, J. Sobhanan, K. M. Sulfiya, C. Jasmin, P. K. Sreelakshmi, Advances in photodynamic antimicrobial chemotherapy, *J. Photochem. Photobiol. C: Photochem. Rev.* **2021**, *19*, 100452.

7. Q. Liu, J. Tian, Y. Tian, Q. Sun, D. Sun et al. Near-infrared-II nanoparticles for cancer imaging of immune checkpoint programmed death-ligand 1 and photodynamic/immune therapy, *ACS Nano* **2021**, *15*, 515.

8. D. Wang, H. Wu, S. Z. F. Phua, G. Yang, W. Qi Lim et al. Self-assembled single-atom nanozyme for enhanced photodynamic therapy treatment of tumor, *Nat. Commun.* **2020**, *11*, 1.

9. X. Ke, D. Wang, C. Chen, A. Yang, Y. Han et al. Co-enhancement of fluorescence and singlet oxygen generation by silica-coated gold nanorods core-shell nanoparticle, *Nanoscale Res. Lett*. **2014**, *9*, 666.

10. Y. Wan, G. Lu, W. C. Wei, Y. H. Huang, S. Li et al. Stable organic photosensitizer nanoparticles with absorption peak beyond 800 nanometers and high reactive oxygen species yield for multimodality phototheranostics, *ACS Nano* **2020**, *14*, 9917.

11. S. Farooq, R. E. de Araujo, Identifying high performance gold nanoshells for singlet oxygen generation enhancement, *Photodiagnosis Photodyn. Ther*. **2021**, *35*, 102466.

12. A. Labib, V. Lenaerts, F. Chouinard, J. C. Leroux, R. Ouellet et al. Biodegradable nanospheres containing phthalocyanines and naphthalocyanines for targeted photodynamic tumor therapy, *Pharm. Res.* **1991**, *8*, 1027.

13. M. Das, A. Solanki, A. Ganesh, S. Thakore, Emerging hybrid biomaterials for oxidative stress induced photodynamic therapy, *Photodiagnosis Photodyn. Ther*. **2021**, *34*.

14. C. Mendoza, N. Emmanuel, C. A. Páez, L. Dreesen, J. C. M. Monbaliu et al. Improving continuous flow singlet oxygen photooxygenation reactions with functionalized mesoporous silica nanoparticles, *ChemPhotoChem* **2018**, *2*, 890.

15. F. F. E. Kohle, S. Li, M. Z. Turker, U. B. Wiesner, Ultrasmall PEGylated and targeted core-shell silica nanoparticles carrying methylene blue photosensitizer, *ACS Biomater. Sci. Eng*. **2020**, *6*, 256.

16. R. Liu, Y. Gao, N. Liu, Y. Suo, Nanoparticles loading porphyrin sensitizers in improvement of photodynamic therapy for ovarian cancer, *Photodiagnosis Photodyn. Ther.* **2021**, *33*, 102156.

17. J. Kim, H. Lee, J. Y. Lee, K. H. Park, W. Kim et al. J. Photosensitized production of singlet oxygen via C60 fullerene covalently attached to functionalized silica-coated stainless-steel mesh: remote bacterial and viral inactivation, *Appl. Catal. B Environ*. **2020**, *270*, 118862.

18. J. Fan, M. Yang, J. Zhang, D. Shabat, X. Peng, Near-infrared chemiluminescent probe for real-time monitoring singlet oxygen in cells and mice model, *ACS Sensors* **2020**, *5*, 3158.

19. D. C. Yang, S. Wang, X. L. Weng, H. X. Zhang, J. Y. Liu et al. Singlet oxygen-responsive polymeric nanomedicine for light-controlled drug release and image-guided photodynamic-chemo combination therapy, *ACS Appl. Mater. Interfaces* **2021**, *13*, 33905.

20. K. Deng, B. Wu, C. X. Wang, Q. Wang, H. Yu et al. An oxidation-enhanced magnetic resonance imaging probe for visual and specific detection of singlet oxygen generated in photodynamic cancer therapy in vivo, *Adv. Healthc. Mater*. **2020**, *9*, 16.

21. H. Lai, J. Yan, S. Liu, Q. Yang, F. Xing et al. Peripheral RAFT polymerization on a covalent organic polymer with enhanced aqueous compatibility for controlled generation of singlet oxygen, *Angew. Chemie. Int. Ed*. **2020**, *59*, 10431.

22. M. A. Filatov, S. Karuthedath, P. M. Polestshuk, H. Savoie, K. J. Flanagan et al. Generation of triplet excited states via photoinduced electron transfer in meso-anthra-BODIPY: fluorogenic response toward singlet oxygen in solution and in vitro, *J. Am. Chem. Soc*. **2017**, *139*, 6282.

23. P. De Bonfils, E. Verron, P. Nun, V. Coeffard, Photoinduced storage and thermal release of singlet oxygen from 1,2-dihydropyridine endoperoxides, *ChemPhotoChem* **2021**, *5*, 847.

24. B. Chen, Y. Yang, Y. Wang, Y. Yan, Z. Wang et al. Precise monitoring of singlet oxygen in specific endocytic organelles by super-PH-resolved nanosensors, *ACS Appl. Mater. Interfaces* **2021**, *13*, 18533.

25. T. Chen, P. Hou, Y. Zhang, R. Ao, L. Su et al. Singlet oxygen generation in dark-hypoxia by catalytic microenvironment-tailored nanoreactors for NIR-II fluorescence-monitored chemodynamic therapy, *Angew. Chem. Int. Ed.* **2021**, *60*, 15006.

26. T. L. Lam, K. C. Tong, C. Yang, W. L. Kwong, X. Guan et al. Luminescent ruffled iridium(iii) porphyrin complexes containing N-heterocyclic carbene ligands: structures, spectroscopies and potent antitumor activities under dark and light irradiation conditions, *Chem. Sci.* **2019**, *10*, 293.

27. D. Liang, Y. Zhang, Z. Wu, Y. J. Chen, X. Yang et al. A near infrared singlet oxygen probe and its applications in in vivo imaging and measurement of singlet oxygen quenching activity of flavonoids, *Sensors Actuators, B Chem.* **2018**, *266*, 645.

28. J. Deng, F. Liu, L. Wang, Y. An, M. Gao et al. Hypoxia- and singlet oxygen-responsive chemo-photodynamic micelles featured with glutathione depletion and aldehyde production, *Biomater. Sci.* **2019**, *7*, 429.

29. J. Chen, D. Li, B. Huo, F. Zhang, X. Zhao et al. Epidermal growth factor receptor-targeted delivery of a singlet-oxygen sensitizer with thermal controlled release for efficient anticancer therapy, *Mol. Pharm.* **2019**, *16*, 3703.

30. D. Wang, B. Xue, T. Y. Ohulchanskyy, Y. Liu, A. Yakovliev et al. Inhibiting tumor oxygen metabolism and simultaneously generating oxygen by intelligent upconversion nanotherapeutics for enhanced photodynamic therapy, *Biomaterials* **2020**, *251*, 120088.

31. S. S. Lucky, K. C. Soo, Y. Zhang, Nanoparticles in photodynamic therapy, *Chem. Rev.* **2015**, *115*, 1990.

32. W. Lv, M. Cao, J. Liu, Y. Hei, J. Bai, Tumor microenvironment-responsive nanozymes achieve photothermal-enhanced multiple catalysis against tumor hypoxia, *Acta Biomater*. **2021**, *135*, 617.

33. Z. Yuan, S. Yu, F. Cao, Z. Mao, C. Gao et al. Near-infrared light triggered photothermal and photodynamic therapy with an oxygen-shuttle endoperoxide of anthracene against tumor hypoxia, *Polym. Chem.* **2018**, *9*, 2124.

34. R. Bresolí-Obach, J. Nos, M. Mora, M. L. Sagristà, R. Ruiz-González et al. Anthracene-based fluorescent nanoprobes for singlet oxygen detection in biological media, *Methods* **2016**, *109*, 64.

35. M. Sun, S. Krishnakumar, Y. Zhang, D. Liang, X. Yang et al. Singlet oxygen probes made simple: anthracenylmethyl substituted fluorophores as reaction-based probes for detection and imaging of cellular $^1O_2$, *Sensors Actuators, B Chem*. **2018**, *271*, 346.

36. X. Liu, P. Dai, T. Gu, Q. Wu, H. Wei et al. Cyclometalated iridium(III) complexes containing an anthracene unit for sensing and imaging singlet oxygen in cellular mitochondria, *J. Inorg. Biochem*. **2020**, 209.

37. J. Zhu, J. Zou, J. Zhang, Y. Sun, X. Dong et al. An anthracene functionalized BODIPY derivative with singlet oxygen storage ability for photothermal and continuous photodynamic synergistic therapy, *J. Mater. Chem. B* **2019**, *7*, 3303.

38. L. Jiao, X. Zhang, J. Cui, X. Peng, F. Song, Three-in-one functional silica nanocarrier with singlet oxygen generation, storage/release, and self-monitoring for enhanced fractional photodynamic therapy, *ACS Appl. Mater. Interfaces* **2019**, 11, 25750.

39. Y. Q. He, W. Fudickar, J. H. Tang, H. Wang, X. Li et al. Capture and release of singlet oxygen in coordination-driven self-assembled organoplatinum(II) metallacycles, *J. Am. Chem. Soc*. **2020**, *142*, 2601.

40. S. Kim, T. Tachikawa, M. Fujitsuka, T. Majima, Far-red fluorescence probe for monitoring singlet oxygen during photodynamic therapy, *J. Am. Chem. Soc.* **2014**, *136*, 11707.

41. R. Kohara, K. Yuyama, Y. Shigeri, V. Biju, Blue-emitting electron-donor/acceptor dyads for naked-eye fluorescence detection of singlet oxygen, *ChemPhotoChem* **2017**, *1*, 299.

42. H. Fidder, A. Lauer, W. Freyer, B. Koeppe, K. Heyne, Photochemistry of anthracene-9, 10-endoperoxide, *J. Phys. Chem. A.* **2009**, *113*, 6289.

43. M. Nathusius, D. Sleeman, J. Pan, F. Rominger, J. Freudenberg et al. Kinetic stabilization of blue-emissive anthracenes: phenylene bridging works best, *Chem. A Eur. J*. **2021**, *27*, 16606.

44. W. Fudickar, T. Linker, Why triple bonds protect acenes from oxidation and decomposition, *J. Am. Chem. Soc*. **2012**, *134*, 15071.

45. V. Kabanov, D. J. Press, R. P. S. Huynh, G. K. H. Shimizu, B. Heyne, Assessment of encapsulated dyes' distribution in silica nanoparticles and their ability to release useful singlet oxygen, *Chem. Commun*. **2018**, *54*, 6320.

46. O. S. Wolfbeis, An overview of nanoparticles commonly used in fluorescent bioimaging, *Chem. Soc. Rev*. **2015**, *44*, 4743.

47. E. S. Shibu, K. Ono, S. Sugino, A. Nishioka, A. Yasuda et al. Photouncaging nanoparticles for MRI and fluorescence imaging in vitro and in vivo, *ACS Nano* **2013**, *7*, 9851.

48. V. Biju, T. Itoh, M. Ishikawa, Delivering Quantum Dots to Cells: Bioconjugated quantum dots for targeted and nonspecific extracellular and intracellular imaging, *Chem. Soc. Rev*. **2010**, *39*, 3031.

49. E. Yaghini, K. F. Pirker, C. W. Kay, A. M. Seifalian, A. J. MacRobert, Quantification of reactive oxygen species generation by photoexcitation of PEGylated quantum dots, *Small* **2014**, *10*, 5106.

50. D. Manzanares, V. Ceña, Endocytosis: the nanoparticle and submicron nanocompounds gateway into the cell, *Pharmaceutics* **2020**, *12*, 371.

51. R. Liu, Y. Gao, N. Liu, Y. Suo, Nanoparticles loading porphyrin sensitizers in improvement of photodynamic therapy for ovarian cancer, *Photodiagnosis Photodyn. Ther*. **2021**, *33*, 102156.

Chapter 5

General conclusions and perspectives

Cancer has become the most devastating disease affecting the healthy longevity plans of developing and developed economies. The challenges facing humanity face are control measures against cancers, such as error-free diagnosis and efficient treatment. Along with various biomedical imaging techniques such as magnetic resonance imaging (MRI), X-ray computed tomography (CT), ultrasound (US), positron emission tomography (PET), and single-photon emission computed tomography (SPECT), solid and fluid sample biopsies help cancer diagnosis by tissue/cell imaging and gene profiling. Also, novel chemotherapeutics and emerging nanomaterials-based phototherapy play important roles in cancer management. In this thesis, I summarized a silica particles-based platform for collecting and detecting cancer cells in the blood and the generation, storing, releasing, and sensing of singlet oxygen, an important component in photodynamic therapy (PDT).

Collecting and analyzing circulating tumor cells (CTCs) by liquid biopsy is promising for cancer detection and treatment follow-up. This is a less invasive tool, helping frequent assays to study the formation of secondary tumors and determine tumor heterogeneity.[1-4] Technologies for CTC enrichment relying on the physical or biological characteristics of CTCs can be classified into immunocapture and biophysical methods. In the immunocapture technique, cells are collected using positive or negative immunomagnetic enrichment or microfluidics or nanomaterials.[5-9] In contrast, biophysical techniques such as microfluidics, membrane filtration, and dielectrophoresis involve the isolation of cells based on the size, density, or electrical charge.[10-15] Following the isolation, CTCs are often identified by various optical techniques. These optical methods suffer from low throughput and decreased cell viability despite the advantages.[16] Further, morphological and gene alterations such as epithelial-to-mesenchymal transition (EMT) downregulate the epithelial phenotypes, lowering the CTC collection efficiency.[17] In chapter 3, I showed an effective method for collecting and characterizing cancer cells in the blood, which adds a new dimension to liquid biopsy for CTC detection. For the cancer cell collection/isolation, I used stem cell antigen-specific immunosilica particles. Also, I used anticancer antigen-specific immuno quantum dots (QDs) and nucleus staining dyes for

error-free CTC detection. The large size of silica microparticles helped gravity separation and collection of the silica-cell complexes, thus eliminating an external centrifugal/magnetic force.

The narrow and bright orange-red emission of two types of QDs, the green emission of the nucleus stain, and the unique photoluminescence lifetimes of these labels helped multiplexed CTC imaging and detection. Also, by using the CD44 antibody, this work overcomes the limitation of EpCAM-based CTC enrichment techniques that cause false positives due to the presence of such antigen in other cells and false negatives due to the EMT transition of CTCS. Thus, by integrating triple fluorescence color, spectral maxima, and lifetime values, this work achieved a nine-fold CTC detection accuracy. This work highlights the clinical relevance of multimodal CTC collection and detection by a noninvasive approach, promising for cancer screening and post-surgical or therapeutic follow-up. This technique helps identify CTCs at the single-cell level. This CTC detection method can be translated into clinical technology by combining a spectro-temporal sensor and disposable silica/silane-coated membranes to enable on-site dip-detection of cancer cells in the blood. Also, the cells collected using large silica particles or membranes maintain their viability for subculturing and genetic profiling of CTCs.

I focus on singlet oxygen detection in the fourth chapter. Singlet oxygen ($^1O_2$) is a highly reactive species with a strong cytotoxic effect, and it induces the oxidation of various biomolecules. It is vital in regulating intracellular signaling pathways and treating cancers by PDT.[18-21] The short $^1O_2$ lifetime demands accurate and sensitive probes for its detection. Different methods for detecting $^1O_2$ include electron-para-magnetic resonance (EPR), phosphorescence, UV-vis spectrophotometry, fluorescence, and chemiluminescence.[22] EPR is used for quantifying and detecting $^1O_2$ using sterically hindered secondary amine probes such as 2,2,6,6-tetramethylpiperidine (TEMP). But the complexity of analysis and expensive instrumentation limits its utility. Phosphorescence of $^1O_2$ at 1270 nm has a low quantum efficiency resulting in a weak signal-to-noise ratio and demanding high sensitivity cooled detectors. Absorbance-based spectrophotometric techniques use probes, such as 9,10-diphenyl anthracene, forming endoperoxides on reaction with $^1O_2$. But poor photostability of the intermediate and the limited sensitivity of spectrophotometry often limit this technique. Chemiluminescence probes such as 2-methyl-6-phenyl-3,7-dihydroimidazo[1,2-α] pyrazine-3-one (CLA) also exhibit good $^1O_2$ sensitivity, but it also reacts with superoxide anion, lowering $^1O_2$ selectivity. Fluorescence probes based on organic molecules ensure high $^1O_2$ detection sensitivity. This technique provides high spatiotemporal resolutions to study the $^1O_2$ generation or decay kinetics. But some sensors show self-sensitization-induced degradation and reactivity

to other ROS such as hydroxyl radical or superoxide.[23] Therefore, stable $^1O_2$ fluorescence probes are continuously sought after, which, combined with $^1O_2$ storing and releasing capabilities add new dimensions to cancer PDT. I developed a silica nanosystem that generates, store, release and sense $^1O_2$ in a spatiotemporally controlled manner for synergized fluorescence-based cell imaging and photodynamic therapeutic applications. A $^1O_2$ sensor was synthesized, and its photophysical properties were investigated at the ensemble-solution and single-particle levels and in living cells. Further, a sensor-sensitizer nanoassembly was constructed by modifying the nanosilica with a porphyrin photosensitizer, $^1O_2$ sensor, and cell-penetrating RGD ligands for intracellular $^1O_2$ delivery and detection. The sensor exhibited ca. 230-fold $^1O_2$ sensitivity in two-step light irradiation, which is the highest sensitivity reported so far. Further, the nanoassembly showed efficient cell internalization on conjugation with RGD peptide, which was confirmed by the uniform distribution of the porphyrin and the sensor fluorescence in the cytoplasm. Cell death by apoptosis was observed under continuous laser irradiation of the labeled cells. Although the sensor shows blue fluorescence, Thus, this work expands the scope for developing new NIR-emissive and two-photon excitation-based $^1O_2$ probes with high fluorescence sensitivity. Also, by incorporating efficient photothermal agents, the design can be further extended to image-guided combined PDT-photothermal therapy.

While nanoparticles (NPs) are enormously utilized in biomedical and commercial products such as electronic gadgets, cosmetics, food additives, surface coatings, and paints, their impacts on human health and the environment need careful attention. NPs toxicity depends on various physiochemical parameters such as the size, shape, composition, morphology, dose, surface smoothness/roughness and modifications, durability, or solubility.[24] These properties determine the extent of biological interactions of NPs with proteins, cells, or tissues. The administration of NPs can be intravenous, subcutaneous, inhalation, transdermal, intraperitoneal, and oral. Among these routes, the small-size NPs facilitate their entry mainly by inhalation (lungs), injection (gastrointestinal tract), dermal penetration, nervous system uptake, etc., which later translocate to the circulatory and lymphatic systems.[25,26] Recent research results connect asthma, lung cancer, bronchitis, Parkinson's disease, and Alzheimer's disease with NP inhalation.[25] Crohn's disease and colon cancers are caused by NP ingestion, whereas the presence of NPs in the blood can result in blood clots, heart diseases, and arrhythmia.[25] NPs are also associated with autoimmune diseases such as rheumatoid arthritis and lupus erythematosus and can adversely affect the liver, spleen, etc., during their translocation.[25] This thesis includes cell-based studies such as membrane labeling and

intracellular delivery of CdSe/ZnS QDs and silica NPs. Although these NPs do not show cytotoxic effects on cultured cells, detailed pharmacokinetic studies are needed before their *in vivo* applications.

5.1 References

1. Z. Feng, J. Wu, Y. Lu, Y. -T. Chan, C. Zhang et al. Circulating tumor cells in the early detection of human cancers, *Int. J. Biol. Sci.* **2022**, *18*, 3251.

2. A. J. Rushton, G. Nteliopoulos, J. A. Shaw, R. C. Coombes, A Review of Circulating Tumour Cell Enrichment Technologies, *Cancers* **2021**, *13*(5), 970.

3. M. T. Gabriel, M. F. Heymann, D. Heymann, Circulating Tumor Cells as a Tool for Assessing Tumor Heterogeneity, *Theranostics* **2019**, *9*(16), 4580.

4. M. Vishnoi, S. Peddibhotla, W. Yin, A. T. Scamardo, G. C. George et al. The isolation and characterization of CTC subsets related to breast cancer dormancy, *Sci. Rep.* **2015**, *5*, 17533.

5. K. C. Andree, A. M. C. Barradas, A. T. Nguyen, A. Mentink, I. Stojanovic et al. Capture of Tumor Cells on Anti-EpCAM-Functionalized Poly(acrylic acid)-Coated Surfaces, *ACS Appl. Mater. Interfaces* **2016**, *8*(23), 14349.

6. L. Chen, M. Peng, N. Li, Q. Song, Y. Yao et al. Combined use of EpCAM and FRα enables the high-efficiency capture of circulating tumor cells in non-small cell lung cancer, *Sci. Rep.* **2018**, 8, 1188.

7. S. Wang, S. Hong, S. Cai, J. Lei, J. Chen et al. Negative depletion mediated brightfield circulating tumour cell identification strategy on microparticle-based microfluidic chip, *J. Nanobiotechnol.* **2020,** *18*(70).

8. J. H. Kim, H. H. Chung, M. S. Jeong, M. R. Song, K. W. Kang et al. One-step detection of circulating tumor cells in ovarian cancer using enhanced fluorescent silica nanoparticles, *Int. J. Nanomedicine* **2013**, *8*, 2247.

9. A. Glia, M. Deliorman, P. Sukumar, F. K. Janahi, B. Samara et al. Herringbone Microfluidic Probe for Multiplexed Affinity-Capture of Prostate Circulating Tumor Cells, *Adv. Mater. Technol.* **2021**, *6*, 2100053.

10. N. Sun, X. Li, Z. Wang, Y, Li, R. Pei, High-purity capture of CTCs based on micro-beads enhanced isolation by size of epithelial tumor cells (ISET) method, *Biosens. Bioelectron.* **2018**, *102*, 157.

11. R. A. Harouaka, M. Nisic, S. Y. Zheng, Circulating tumor cell enrichment based on physical properties, *J. Lab. Autom.* **2013**, *18*, 455.

12. S. Khetani, M. Mohammadi, A. S. Nezhad, Filter-based isolation, enrichment, and characterization of circulating tumor cells, *Biotechnol. Bioeng*. **2018**, *115*, 2504.

13. Q. Huang, F. B. Wang, C. H. Yuan, Z. He, L. Rao et al. Gelatin nanoparticle-coated silicon beads for density-selective capture and release of heterogeneous circulating tumor cells with high purity, *Theranostics* **2018,** *8*, 1624.

14. Z. Liu, R. Chen, Y. Li, J. Liu, P. Wang et al. Integrated microfluidic chip for efficient isolation and deformability analysis of circulating tumor cells, *Adv. Biosyst.* **2018**, *2*.

15. P. R. C. Gascoyne, S. Shim, Isolation of circulating tumor cells by dielectrophoresis, *Cancers* **2014**, *6*, 545.

16. P. Banko, S. Y. Lee, V. Nagygyorgy, M. Zrinyi, C. H. Chae, D. H. Cho, A. Telekes, Technologies for circulating tumor cell separation from whole blood, *J. Hematol. Oncol. Pharm.* **2019**, *12* (48).

17. A. Martowicz, G. Spizzo, G. Gastl, G. Untergasser, Phenotype-Dependent Effects of EpCAM Expression on Growth and Invasion of Human Breast Cancer Cell Lines, *BMC Cancer* **2012**, *12*, 1.

18. V. A. Dmitrieva, E. V. Tyutereva, O. V. Voitsekhovskaja, Singlet Oxygen in Plants: Generation, Detection, and Signaling Roles, *Int. J. Mol. Sci.* **2020**, *21*(9), 3237.

19. M. Riethmuller, N. Burgur, G. Bauer, Singlet oxygen treatment of tumor cells triggers extracellular singlet oxygen generation, catalase inactivation and reactivation of intercellular apoptosis-inducing signaling, *Redox. Biol.* **2015**, *6*, 157.

20. C. Nathan, A. C. Bussel, Beyond oxidative stress: an immunologist's guide to reactive oxygen species, *Nat. Rev. Immunol.* **2013**, *13*, 349.

21. G. Bauer, D. Sersenova, D. B. Graves, Z. Machala, Dynamics of singlet oxygen-triggered, RONS-based apoptosis induction after treatment of tumor cells with cold atmospheric plasma or plasma-activated medium, *Sci. Rep.* **2019,** *9*, 13931.

22. H. Wu, Q. Song, G. Ran, X. Lu, B. Xu, Recent developments in the detection of singlet oxygen with molecular spectroscopic methods, *Trends Anal. Chem.* **2011**, *30*(1).

23. D. B. Zhu, D. Xing, Y. D. Wei, X. Li, B. Gao, Evaluation of the degree of medical radiation damage with a highly sensitive chemiluminescence method, *Luminescence* **2004**, *19*(5), 278.

24. T. A. Saleh, Nanomaterials: Classification, properties, and environmental toxicities, *Environ. Technol. Innov.* **2020**, *20*, 101067.

25. C. Buzea, I. I. Pacheco, K. Robbie, Nanomaterials and nanoparticles: Sources and toxicity, *Biointerphases* **2007**, *2*(4).

26. S. Sharifi, S. Behzadi, S. Laurent, M. L. Forrest, P. Stroeve et al. Toxicity of nanomaterials, *Chem. Soc. Rev.* **2012**, *41*, 2323.

Publications and patents

Peer-reviewed Articles

1. **Toxicity of Nanomaterials Due to Photochemical Degradation and the Release of Heavy Metal Ions.**
   J. Sobhanan, P. Jones, R. Kohara, S. Sugino, M. Vacha, C. Subrahmanyam, Y. Takano, F. Lacy, V. Biju
   Nanoscale **2020**, *12*, 22049 (Featured on the cover page).

2. **Multimodal Detection of Cancer Cells in the Blood using Stem Cell Antigen-Specific Immunosilica Particles and Immunofluorescent Quantum Dots.**
   J. Sobhanan, Y. Takano, S. Sugino, E. Hirata, S. Yamamura, V. Biju
   NPG Asia Mater. **2022**, *14*, 3.

3. **Molecular Recognition in the Infection, Replication, and Transmission of COVID-19-Causing SARS-CoV-2: An Emerging Interface of Infectious Disease, Biological Chemistry, and Nanoscience.**
   P.Kumar,† **J. Sobhanan**,† Y. Takano, V. Biju (†Equal contribution)
   NPG Asia Mater. **2021**, *13*, 14.

4. **Advances in Photodynamic Antimicrobial Chemotherapy.**
   A. Anas, **J. Sobhanan,** K. M. Sulfiya, C. Jasmin, P. K. Sreelakshmi, V. Biju
   J. Photochem. Photobiol. C Photochem. Rev. **2021**, *49*, 100452.

5. **Near Infrared Light Control of Membrane Potential by an Electron Donor-Acceptor Linked Molecule.**
   Y. Takano, K. Miyake, **J. Sobhanan**, V. Biju, N. V. Tkachenko, H. Imahori
   Chem. Commun. **2020**, *56*, 12562.

6. **Mechano-Optical Modulation of Excitons and Carrier Recombination in Self-Assembled Halide Perovskite Quantum Dots.**
   Z. Zhang, S. Ghimire, T. Okamoto, B. M. Sachith, **J. Sobhanan,** C. Subrahmanyam, V. Biju
   ACS Nano **2022**, *16*, 160 (Featured on the cover page).

7. **Photoeradication of Aquatic Pathogens by Curcumin for clean and safe drinking water.**
   S. K. Moideen, A. Anas, **J. Sobhanan**, H. Zhao, V. Biju
   J. Photochem. Photobiol. A: Chem. **2022**, *432*, 114104.

Patents

1. **Mechano-optical modulation of exciton and charge carrier recombination in self-assembled halide perovskite quantum dots.**
   V. Biju, Z. Zhijing, S. Ghimire, T. Okamoto, B. M. Sachith, **J. Sobhanan**
   Japanese Patent Application Number P2021-125.

2. **Development of a sensor and a sensor-sensitizer nanoassembly for intracellular and solution phase singlet oxygen detection and the processes thereof**
   V. Biju, **J. Sobhanan**
   Japanese Patent Application Number P2021-209.

Papers presented at conferences

1. **Environmental Degradation of PbS and CdSe Quantum Dots and the Related Toxicity**
   J. Sobhanan, Y. Takano, V. Biju
   The 102nd Annual Meeting of the Chemical Society of Japan, Japan, 25 Mar **2022**. **[Oral]**

2. **Sensor-Sensitizer Loaded Mesoporous Silica Nanoparticles for Biosensing and Bioimaging**.
   J. Sobhanan,V. Biju
   The 22nd RIES-Hokudai International Symposium, Sapporo, Japan, 6 Dec **2021**. **[e-Poster]**

3. **Multimodal Detection of Circulating Tumor Cells Using Multifunctional Silica Particles**.
   J. Sobhanan, Y. Takano, V. Biju
   Annual Meeting of the Japanese Photochemistry Association 2021, Japan, 14 Sep **2021**. **[e-Poster]**

4. **Multimodal Detection of Circulating Tumor Cells Using Multifunctional Silica Particles.**
   J. Sobhanan, Y. Takano, V. Biju
   The Chemical Society of Japan Hokkaido Branch 2021 Summer Research Presentation, Japan, 17 July **2021**. **[Oral]**

5. **Multimodal Detection of Circulating Tumor Cells Using Multifunctional Silica Particles.**
   J. Sobhanan, Y. Takano, V. Biju
   The 101st Annual Meeting of the Chemical Society of Japan, Japan, 21 Mar **2021**. **[Oral]**

6. **Gravity Separation and Microspectroscopic Detection of Circulating Tumor Cells in the Blood.**
   J. Sobhanan
   International Conference on Materials for the Millennium – MATCON 2021, India, 15 Mar **2021**. **[Oral]**

7. **Spectrally and Temporally Resolved Modalities for the Selective Detection of Cancer Cells from Among Blood Cells.**
   J. Sobhanan, Y. Takano, V. Biju
   The Chemical Society of Japan Hokkaido Branch 2021 Winter Research Presentation, Japan, 26 Jan **2021**. **[e-Poster]**

8. **Multimodal Detection of Circulating Tumor Cells Using Multifunctional Silica Particles.**
   J. Sobhanan, Y. Takano, V. Biju
   The 21st RIES-Hokudai International Symposium, Sapporo, Japan, 10 Dec **2020**. **[e-Poster]**

9. **The Release of Heavy Metal Ions from Engineered Nanomaterials: The Origin and Mechanism of Nanotoxicity.**
   J. Sobhanan, Y. Takano, V. Biju
   The 6th Hokkaido University Cross-Departmental Symposium, Sapporo, Japan, 19 Oct **2020**. **[e-Poster]**

10. **Cytotoxicity and Genotoxicity of Engineered Nanomaterials due to the Release of Heavy Metal Ions.**
    J. Sobhanan, Y. Takano, V. Biju,
    Annual Meeting of the Japanese Photochemistry Association 2020, Japan, 9 Sep **2020**. **[e-Poster]**

11. **Fluorescence Microscopic and Spectroscopic Investigations of Ligand-Protein Interactions in Cell Membrane using Quantum Dot-Folic Acid Conjugate.**
    J. Sobhanan, Y. Takano, V. Biju
    2019 International Symposium of Research Institute for Electronic Science (RIES) and Center for Emerging Functional Matter Science (CEFMS), Sapporo, Japan, 3 Dec **2019**. **[Poster]**

Research highlights and awards

Cover pages

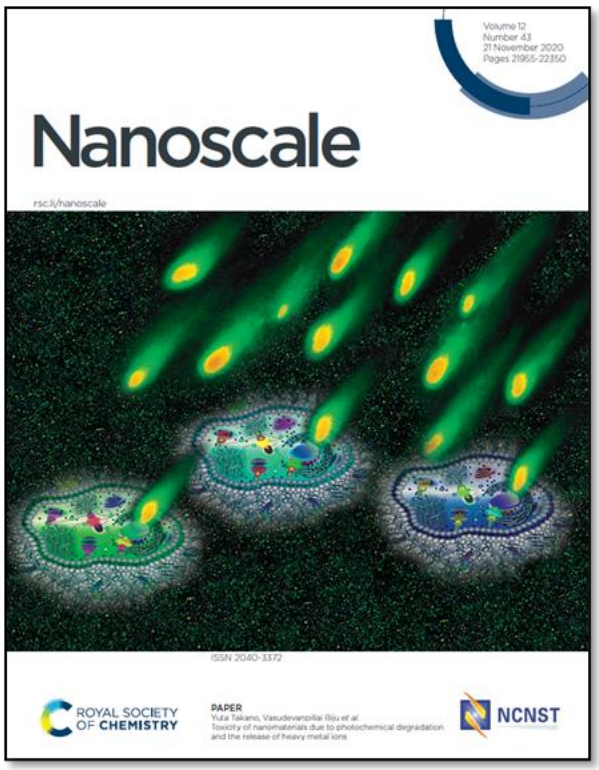

J. Sobhanan, *et al., Nanoscale* **2020**, *12*, 22049.

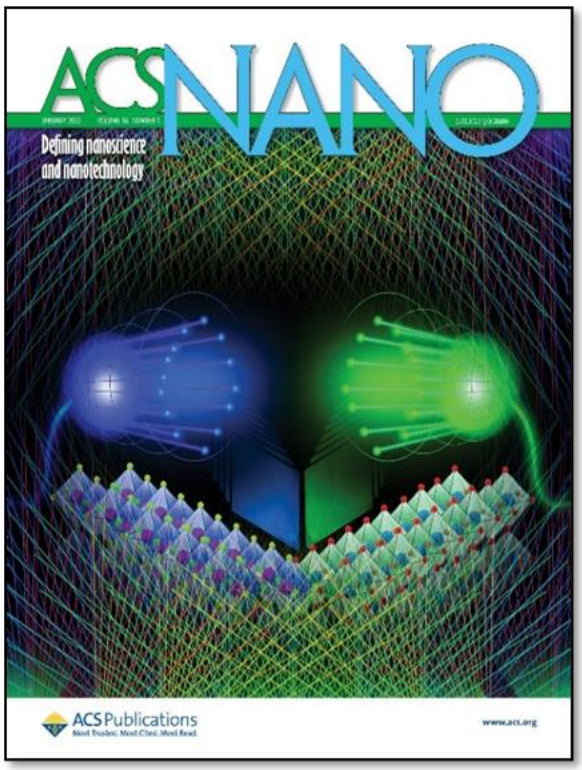

Z. Zhang, S. Ghimire, T. Okamoto, B. M. Sachith, J. Sobhanan *et al. ACS Nano* **2022**, *16*, 160.

Awards

1. **The Best Presentation Award**, *the 21st RIES-Hokudai International Symposium*, 2020, Hokkaido University.

2. **The Journal of Photochemistry and Photobiology A: Chemistry (Elsevier) Award** for the Best Presentation, *the Japanese Photochemistry Association*, 2021, Japan.

3. **Research Excellence Award**, *Graduate School of Environmental Science*, 2022, Hokkaido University.